From winds to eddies to diapycnal mixing of the deep ocean: the abyssal meridional overturning circulation driven by the surface wind-stress.

by

Geoffrey John Stanley
B.Math, University of Waterloo, 2011

A Thesis Submitted in Partial Fulfillment of the
Requirements for the Degree of

MASTER OF SCIENCE

in the School of Earth and Ocean Sciences

© Geoffrey John Stanley, 2013
University of Victoria

All rights reserved. This thesis may not be reproduced in whole or in part, by photocopying or other means, without the permission of the author.

From winds to eddies to diapycnal mixing of the deep ocean: the abyssal meridional overturning circulation driven by the surface wind-stress.

by

Geoffrey John Stanley
B.Math, University of Waterloo, 2011

Supervisory Committee

Dr. O. A. Saenko, Supervisor
(School of Earth and Ocean Sciences;
Canadian Centre for Climate Modelling and Analysis)

Dr. A. J. Weaver, Supervisor
(School of Earth and Ocean Sciences)

Dr. J. M. Klymak, Departmental Member
(School of Earth and Ocean Sciences)

Supervisory Committee

Dr. O. A. Saenko, Supervisor
(School of Earth and Ocean Sciences;
Canadian Centre for Climate Modelling and Analysis)

Dr. A. J. Weaver, Supervisor
(School of Earth and Ocean Sciences)

Dr. J. M. Klymak, Departmental Member
(School of Earth and Ocean Sciences)

ABSTRACT

Previous numerical and theoretical results based on constant diapycnal diffusivity suggested the abyssal meridional overturning circulation (MOC) should weaken as winds over the Southern Ocean intensify. We corroborate this result in a simple ocean model, but find it does not hold in more complex models. First, models with a variable eddy transfer coefficient and simple yet dynamic atmosphere and sea-ice models show an increase, albeit slightly, of the abyssal MOC under increasing winds. Second, the abyssal MOC significantly strengthens with winds when diapycnal diffusivity is parameterized to be energetically supported by the winds. This tests the emerging idea that a significant fraction of the wind energy input to the large-scale ocean circulation is removed by mesoscale eddies and may then be transferred to internal lee waves, and thence to bottom-enhanced diapycnal mixing. A scaling theory of the abyssal MOC is extended to incorporate this energy pathway, corroborating our numerical results.

Contents

List of Tables

List of Figures

ACKNOWLEDGEMENTS

I would like to express my thanks, first and foremost, to my supervisor Dr. Oleg Saenko for developing this tractable yet expansive project and skillfully guiding me through it. I also thank Dr. Andrew Weaver and Dr. Jody Klymak for their mentorship, encouragement, and further guidance and insight in this research. I am grateful for financial support from the Natural Sciences and Engineering Research Council (NSERC) of Canada in the form of a *Julie Payette-NSERC Research Scholarship* and also through the *CREATE Training Program in Interdisciplinary Climate Science at the University of Victoria*; for his role in the latter, Dr. Andrew Weaver deserves my further appreciation. I also thank Dr. Patrick Cummins for thoughtfully reviewing the thesis and providing useful suggestions.

I have received tremendous support from many others as well. Thanks to the climate lab staff, Ed Wiebe, Mike Eby, and Wanda Lewis, for your skillful technical support. Many other students of the climate lab and the School brightened my graduate experience. In particular I thank Neil Swart for our discussions while I was first learning about physical oceanography, and Dave Janssen for his natural flare that helped keep me mentally well-balanced through the toughest moments.

My ever-lasting thanks goes to my family. To my parents Jan and Leonard Stanley who instilled in me curiosity, dedication, and mathematics, because of you I never doubted that I would make my career in science. To my brother David Stanley, my elder, who is following a similar path in science, because of your invaluable insight which you have always so freely offered, my path has been smooth. And finally, to my partner Karen McCallum, because of the diversity of your thoughts you kept my focus on the big picture and lent meaning to this work, and with your unending support you made it all joyful and possible.

Chapter 1

Introduction

Turbulent mixing in a stratified ocean requires an input of mechanical energy, the primary sources of which are the winds and the tides [Munk and Wunsch, 1998]. While the impact on the large-scale ocean circulation by tidally-drive diapycnal mixing has been the focus of several studies, the possibility of wind-driven diapycnal mixing in the abyss has not been correspondingly explored. In part, this is because wind energy is input at the ocean surface and it is far from clear how it makes its way to small-scale turbulence in the abyss. This energy pathway is coming to be understood through recent theoretical, observational, and numerical studies that describe mesoscale eddies, fed by wind energy, interacting with rough bottom topography and generating internal lee waves which break in near-bottom turbulent bursts [Marshall and Naveira Garabato, 2008].

The major goal of this thesis is to evaluate how the simulated ocean circulation is influenced by the capacity of the winds to support diapycnal mixing in the abyss. To this end, two distinct parameterizations of diapycnal mixing in which eddy energy supports bottom-enhanced diapycnal mixing are proposed and tested. The focus is on the response of the abyssal meridional overturning circulation (MOC) to changes in the strength of the Southern Hemisphere westerly winds. There are two branches of study.

The first is a theoretical approach. Previous theoretical scalings have predicted a decrease in the strength of the abyssal MOC under increased westerly wind-stress over the Southern Ocean [Ito and Marshall, 2008], at least in the limit of weak mixing in the abyss [Nikurashin and Vallis, 2011]. These scalings are examined in this thesis and one is extended to incorporate wind/eddy-driven diapycnal mixing. With this extension, the abyssal MOC, being driven by abyssal diapycnal mixing that is itself driven by the winds, is predicted to *increase* under increased westerly wind-stress. With a combination of wind-dependent and wind-independent energy supporting diapycnal mixing, some interesting behaviour is predicted at low wind-stress, including a critical wind-stress at which the abyssal MOC attains a minimum strength. The scaling theory is also generalized, resulting in somewhat different qualitative predictions.

The second approach is numerical, using a coarse-resolution ocean-climate model configured in an idealized basin geometry. Eddies are parameterized by way of Gent and McWilliams [1990], which sap potential energy, originating primarily from the winds, at a cleanly calculable rate [Tandon and Garrett, 1996]. This energy is then released, using the proposed parameterizations, to diapycnal mixing. These numerical modelling efforts corroborate the theoretical predictions we make that the abyssal MOC intensifies under stronger winds when diapycnal mixing is linked to the wind energy input, and contrast previous numerical results based on wind-independent diapycnal mixing. When winds are decreased, feedbacks with the atmosphere, sea-ice, and eddy transfer coefficient can become dominant such that the abyssal MOC collapses at low winds. Indeed, our theoretical prediction of an increase of the abyssal MOC below a critical wind-stress is found in only one particular model.

This work is significant because anthropogenic climate change has intensified the Southern Hemisphere westerly winds, which drive upwelling in the Southern Ocean and hence outgassing of deep carbon reserves [Lovenduski *et al.*, 2008]; moreover, this trend is projected to continue. Since the abyssal ocean is an enormous reservoir of both heat and carbon, it is of great importance to understand how the abyssal ocean circulation will change under changing winds. If the abyssal MOC speeds up, climate feedbacks involving the abyssal ocean will act on shorter time-scales. This may be especially significant if the abyssal MOC's spatial structure changes, such as from a basin-scale overturning to one with a faster recirculation in the Southern Ocean. This thesis represents an initial and hopefully thought-provoking sensitivity study of the abyssal MOC to changes in wind energy input.

Outline

The layout of this thesis is as follows:

Chapter 1 motivates the problem to be studied and introduces the claims to be proved by this thesis.

Chapter 2 describes in detail the energy pathway from surface winds to abyssal diapycnal mixing, and develops parameterizations for this process.

Chapter 3 describes the abyssal MOC from a theoretical perspective. A simple picture of the circulation is given, and scaling theories of the abyssal MOC are derived.

Chapter 4 describes the numerical model and experimental design used in this thesis.

Chapter 5 examines the numerical results and provides a physical analysis, drawing on the theory from Chapter 3.

Chapter 6 summarizes the key conclusions of this thesis.

Appendices A & B further discuss oceanic eddies, including their effect on the circulation and their parameterization in general circulation models.

Appendix C develops an alternative scaling theory of the abyssal MOC.

Chapter 2

Wind/Eddy-Driven Diapycnal Mixing

Observations indicate that diapycnal mixing is highly non-uniform [e.g. Kunze *et al.*, 2006], being relatively weak in the upper ocean interior [Gregg, 1987; Ledwell *et al.*, 1993] and enhanced in the abyss, especially above complex topography, along the boundaries, and in the Southern Ocean [Polzin *et al.*, 1997; Naveira Garabato *et al.*, 2004; Walter *et al.*, 2005; Sloyan, 2005]. Evidently, then, the mechanical energy driving small-scale turbulence, though originating at the surface on large-scales, preferentially dissipates in certain regions and to varying degrees, owing to the complexities of transferring energy through different scales of oceanic flow. In this chapter we review the physical underpinnings of this cascade of energy, and develop a parameterization for use in numerical ocean models that is based on this energy cascade and thereby, it is hoped, captures in a realistic way some of the complexities of the distribution of mixing and mixing energy within the ocean.

2.1 The energy pathway from surface winds to abyssal mixing

The energy pathway studied in this thesis transmits wind energy that is input on large-scales (Figure 2.1) at the surface, through eddies (Figure 2.2), to small-scale turbulent mixing in the abyssal ocean. We now describe the physics of this energy pathway.

The large-scale forcing of the ocean by wind, by air-sea exchange of heat and

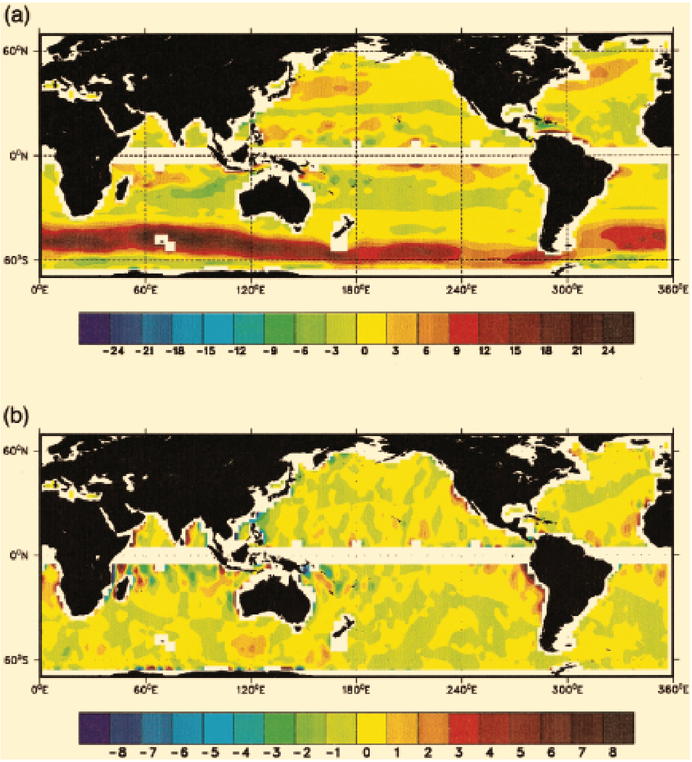

Figure 2.1: Work of the wind on the geostrophic current, $\overline{\tau \cdot \mathbf{u}_g}$ [10^{-3} W m^{-2}], separated as the (a) zonal component and (b) meridional component, with the overline denoting a long-time average. The wind-stress τ was taken from the National Centers for Environment Prediction (NCEP) climatology and the surface geostrophic flow $\mathbf{u}_g$ was derived from satellite observations of sea surface height, having applied geostrophy. The dominant source of wind energy input is from the Southern Hemisphere westerlies over the Antarctic Circumpolar Current, though the wind-work on the Kuroshio and Gulf Stream/North Atlantic Current is also notable. Figure reproduced from [Wunsch, 1998], © Copyright 1998 American Meteorological Society.

freshwater, and by differential solar radiation drive a global circulation, including flow in the abyssal ocean. A near-bottom current of magnitude U that is normal to topographic relief can generate internal waves with horizontal scales between U/N and U/f, with N and f being the buoyancy and Coriolis frequencies, respectively [Gill, 1982; Scott *et al.*, 2011; Ferrari and Wunsch, 2009]. The current in question could be a feature of the large-scale circulation. Indeed, relatively strong and deeply penetrating mean currents in the Southern Ocean and along western boundaries could generate internal waves by this mechanism. Furthermore, in several places deep currents have been observed that seem to have been forced by time-varying winds [e.g. Koblinsky

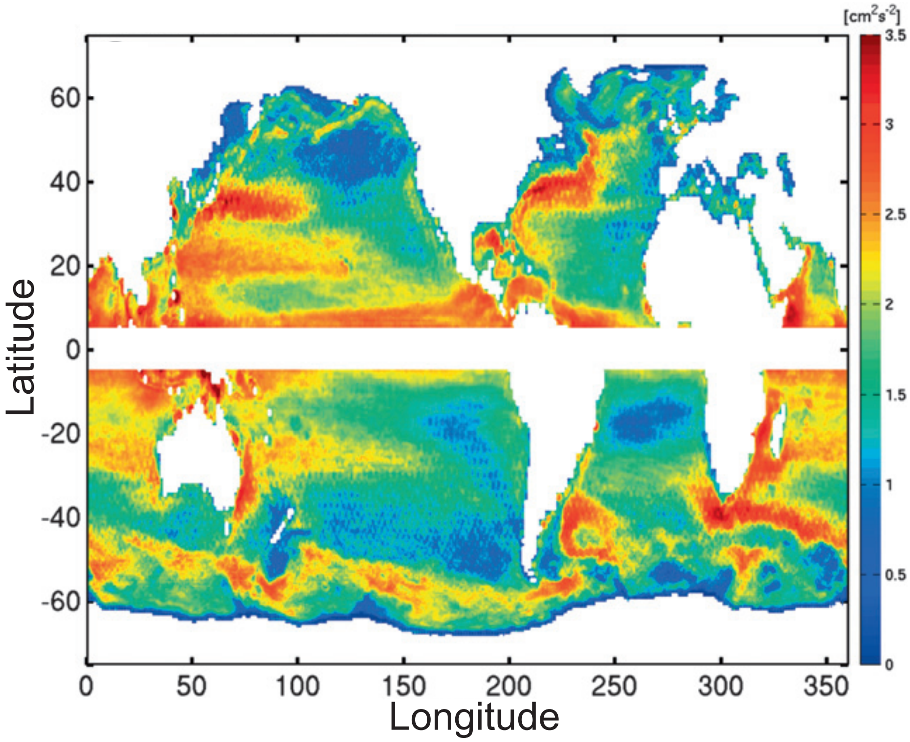

Figure 2.2: Logarithm of eddy kinetic energy (EKE) [cm^2 s^{-2}] derived from satellite observations from 2003–2007 of sea surface height, using geostrophy to obtain sea surface velocity. A ±5° belt around the equator is masked where geostrophy breaks down. EKE is highest in the western boundary currents, the Southern Ocean, and the tropics. Figure reproduced from [Farneti *et al.*, 2010], © Copyright 2010 American Meteorological Society.

and Niiler, 1982]; theoretical arguments [e.g. Willebrand *et al.*, 1980] and numerical results [e.g. Saenko, 2008] support the possibility of strong, time-varying currents over vast regions of the deep ocean that appear to be driven largely by seasonal variations of the surface wind-stress.

However, because of their (generally) larger kinetic energy, mesoscale eddies are likely to be of more importance than mean currents in generating internal waves through this mechanism, provided that they are deep-reaching. While there is large uncertainty in the available estimates, it appears that a significant fraction of the wind energy input to the surface geostrophic currents is removed from the mean state by baroclinic instability [Huang and Wang, 2003; Wunsch and Ferrari, 2004], forming eddies. This is also supported by estimates based on eddy-resolving simulations [Zhai and Marshall, 2013]. With this in mind, we now examine the lifecycle of eddies, with particular attention to whether eddies may dissipate their energy in small-scale abyssal motions.

The most fundamental components of the energy cascade through eddies are illustrated in Figure 2.3. The large-scale forcing of the ocean provides a steady supply of available potential energy (APE), as is evident by differential heating generating more buoyant waters at low-latitudes, or by the wind-work on the oceanic general circulation (Figure 2.1) fluxing light waters downward and denser waters upward such as around the latitudes of Drake Passage. This APE, distributed on the basin-scale, is consumed by baroclinic eddies, which are formed through baroclinic instability at, or somewhat larger than, the scale of the first baroclinic Rossby radius [Marshall and Naveira Garabato, 2008]. The downscale, or direct, cascade of baroclinic energy continues until it reaches the Rossby radius of deformation L_d for the given vertical mode. At this scale the direct cascade of energy is largely arrested and energy is instead transferred to the lower baroclinic modes, or to the barotropic mode in the case of the first baroclinic mode [Charney, 1971; Salmon, 1998]. Barotropic eddies, constrained by vertical homogeneity, behave akin to turbulence in two dimensions, merging and growing in spatial-scale, as well as in their degree of barotropization. This inverse cascade of barotropic energy to larger spatial scales is arrested near the Rhines scale $\sim \sqrt{U/\beta}$, where U is a root-mean-square velocity at energy-containing scales and β is the northward gradient of the Coriolis parameter [Rhines, 1975]; at this scale, energy is transferred through Rossby waves to the mean flow in the form of banded zonal jets.

However, it is possible for this barotropic energy to be dissipated through other mechanisms before reaching the Rhines scale. Scott and Wang [2005] used satellite altimetry to observe the spectral flux of eddy kinetic energy (EKE) and found broad agreement with the above theory in most regions of the ocean, including an inverse energy cascade at long wavelengths and its arrest near the Rhines scale. The stark exception is the region of the Antarctic Circumpolar Current (ACC), where they found the inverse energy cascade to be arrested well below the Rhines scale. Here, the Rhines scale is a maximum owing to the large mean speeds, and the deformation radius is relatively small owing to the high latitude: thus the theoretical scales for the source and the sink of barotropic energy are particularly distant, allowing barotropization to develop more fully. While the reason for this premature arrest is far from clear, one enticing possibility is that the more fully developed barotropic eddies of this region foster enhanced energy dissipation through interaction with the sea-floor [Marshall

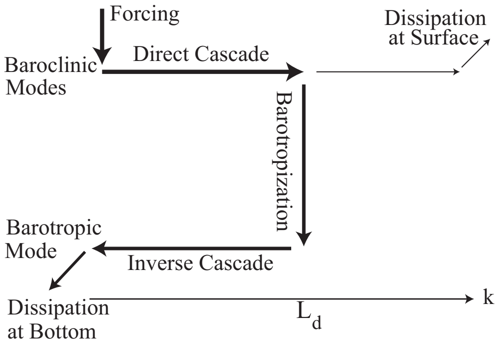

Figure 2.3: A schematic of how energy is transferred through different modes and scales in geostrophic turbulence. The horizontal axis is the horizontal wave number k, hence larger spatial scales are at left. Motions are separated according to their vertical dependence as either barotropic (lower) or baroclinic of any vertical mode (upper). Energy is predominantly input on large scales, then cascades downscale to the Rossby radius of deformation L_d where baroclinic instability forms baroclinic eddies. At this scale, eddies homogenize vertically (barotropisation) and then grow in spatial scale (as in 2D turbulence). Energy dissipation occurs largely through bottom-interactions, which are available to barotropic eddies, though some energy also dissipates near the surface. Figure adapted from [Ferrari and Wunsch, 2009].

and Naveira Garabato, 2008].

The notion that genuine eddy energy dissipation occurs primarily near the sea-floor is supported by the lack of a convincing dissipation mechanism away from the sea-floor. There are two other possible locations for dissipation. In the interior, eddy energy can be dissipated either by non-linear eddy-internal wave interactions or by generation of new internal waves through loss of balance. The former is weak in the geophysical setting, as implied by non-acceleration theorems [Dewar and Killworth, 1995], while the latter remains under investigation. The second option is dissipation near the surface. Scott and Wang [2005] observe from the altimetric signal that at L_d about 1/4 of the kinetic energy continues to cascade downscale, leaving the remaining 3/4 to cascade upscale. Since the former is due to baroclinic eddies and the latter primarily due to barotropic eddies, and since only barotropic eddies are exposed to the sea-floor, we are led to conclude that dissipation at the sea-floor is significantly stronger than dissipation at the surface [Marshall and Naveira Garabato, 2008]. Further evidence for bottom-dissipation using satellite altimetry is presented by Gille *et al.* [2000], who argue from the statistical anti-correlation between bottom roughness and EKE that not only is the sea-floor a dominant sink of eddy energy, but more specifically that the mechanism for bottom-dissipation is dependent upon the roughness of the bottom topography — the possibility of which we now consider.

Though there are several mechanisms whereby EKE can be dissipated near the sea-floor, eddy interaction with rough-topography is likely the most significant. Numerical simulations of flow over topography, comparing flat topography to rough topography that is spectrally akin to that found in the Drake Passage, show the generation of internal gravity waves in the lee of topography to be a far more efficient dissipation mechanism than bottom boundary layer drag, which is the only dissipation mechanism available in a flat-bottomed ocean [Nikurashin *et al.*, 2013]. When these internal lee waves break, they induce diapycnal mixing; thus, observational evidence of intense diapycnal mixing over rough topography in strongly eddying regions [e.g. Naveira Garabato *et al.*, 2004; Sloyan, 2005] corroborates the conjecture that the dominant sink of eddy energy is the generation of internal lee waves by deep-reaching flows impinging on rough bottom topography. Furthermore, Naveira Garabato *et al.* [2007] analyzed the spreading of a natural tracer in the southwest Atlantic sector of the ACC and calculated the energy released by baroclinic instability in the region, of which the energy consumed by diapycnal mixing in the same region was found to be a significant fraction (about 50%). This further corroborates the conjecture that it is the energy released by eddies that supports this intense diapycnal mixing. This energy pathway is likely to be active outside the ACC as well, including in the deeply reaching zonal jets [e.g. Maximenko *et al.*, 2005] and in the regions of western boundary currents and their extensions [Zhai *et al.*, 2010].

Assuming that at least a fraction of the eddy energy supports small-scale mixing in the abyss, the described energy pathway may have important implications for the associated MOC and its response to changes in wind energy input and ocean eddy activity. In the next section we derive the rate of energy dissipation (ϵ) by mesoscale eddies parameterized according to Gent and McWilliams [1990, hereafter GM]. Then expanding upon Marshall and Naveira Garabato [2008], in the last section we use ϵ to develop representations of this energy pathway in numerical ocean models with GM-parametrized eddies.

2.2 Dissipation of energy by Gent-McWilliams eddies

One of the most widely used eddy parameterizations employed in ocean climate modelling, including in this study, is that due to GM. The GM scheme ensures that the parametrized eddies remove APE from the mean state adiabatically — that is, without mixing across buoyancy surfaces [Gent *et al.*, 1995]. In steady state, the rate of consumption of APE by the eddies must equal the rate of eddy energy dissipation ϵ, the formula for which we now derive, following Gent *et al.* [1995] and Tandon and Garrett [1996].

Begin with the linearized steady-state equation describing the resolved (large-scale) horizontal flow $\overline{\mathbf{u}}$ in a Boussinesq ocean, which is

$$f\mathbf{k} \times \overline{\mathbf{u}} = -\frac{\nabla_h p}{\rho_0} + \frac{\partial_z \mathbf{T}}{\rho_0}, \tag{2.1}$$

where f is the Coriolis parameter, p the pressure, $\mathbf{T}$ the applied stress (given as $\boldsymbol{\tau}$ at the surface), ρ_0 a reference density, $\mathbf{k}$ the vertical unit vector, and $\nabla_h \equiv (\partial_x, \partial_y)$. Combining (2.1) with the hydrostatic balance and assuming $\partial_{zz}\mathbf{T}$ is small, we get the thermal wind relation

$$f\mathbf{k} \times \partial_z \overline{\mathbf{u}} = -\nabla_h \bar{b}, \tag{2.2}$$

where $\bar{b} = -g(\rho - \rho_0)\rho_0^{-1}$ is the resolved buoyancy. The horizontal residual transport velocity (see Appendix A) is

$$\mathbf{u}^\dagger = \overline{\mathbf{u}} + \mathbf{u}^*, \tag{2.3}$$

and similarly in the vertical, $w^\dagger = \overline{w} + w^*$; in the GM parameterization, $\mathbf{u}^* = -\partial_z(K_{GM}\mathbf{s})$ is the eddy-induced velocity, where $\mathbf{s} = -\nabla_h \bar{b}/\partial_z \bar{b}$ is the isopycnal slope, and K_{GM} is the eddy transfer coefficient. Transforming (2.1) to use $\mathbf{u}^\dagger$, then using the GM scheme for $\mathbf{u}^*$ and using (2.2) to relate back to resolved velocities, and finally using the residual decomposition (2.3) again, we obtain

$$f\mathbf{k} \times \mathbf{u}^\dagger = -\frac{\nabla_h p}{\rho_0} + \frac{\partial_z \mathbf{T}}{\rho_0} + \partial_z \left(K_{GM} \frac{f^2}{N^2} \partial_z \mathbf{u}^\dagger \right) - \partial_z \left(K_{GM} \frac{f^2}{N^2} \partial_z \mathbf{u}^* \right), \tag{2.4}$$

where $N^2 = \partial_z \bar{b}$ is the squared buoyancy frequency. Numerical experiment [Gent *et al.*, 1995] and scaling arguments [Tandon and Garrett, 1996] suggest that $|\partial_z \mathbf{u}^*|/|\partial_z \mathbf{u}^\dagger| \ll 1$, and hence the last term on the right of (2.4) can be ignored.

Then, by comparison with (2.1), we see the GM eddy parameterization is equivalent to a vertical mixing of momentum with vertical viscosity coefficient $K_{GM}f^2/N^2$ [Gent *et al.*, 1995]. Indeed, eddies transport horizontal momentum downwards through out-of-phase fluctuations between pressure and isopycnal depth (interfacial form stress; see e.g. Olbers *et al.* 2004).

Multiplying (2.4) by $\rho_0\mathbf{u}^\dagger$ and using the continuity equation $\nabla_h\mathbf{u}^\dagger + \partial_z w^\dagger = 0$, some manipulation gives the budget of kinetic energy as [see Eq. 25 in Gent *et al.*, 1995]

$$\nabla_h \cdot (p\mathbf{u}^\dagger) + \partial_z(pw^\dagger) - \partial_z\left(\rho_0 K_{GM}\frac{f^2}{N^2}\mathbf{u}^\dagger \cdot \partial_z\mathbf{u}^\dagger\right) = \rho_0\bar{b}w^\dagger + \partial_z\mathbf{T}\cdot\mathbf{u}^\dagger - \rho_0\epsilon. \quad (2.5)$$

On the RHS, the first term is the conversion rate of potential to kinetic energy, while the last term, with $\epsilon \equiv K_{GM}(f^2/N^2)(\partial_z\overline{\mathbf{u}})^2$, is the rate of kinetic energy dissipation by GM-parameterized eddies. This can be further transformed, by (2.2), to

$$\epsilon = K_{GM}\ N^2 s^2, \quad (2.6)$$

where $s = |\mathbf{s}|$.

The spatial structure of $\rho_0\epsilon$ is estimated from the Levitus climatology and shown in Figure 2.4. Globally, it integrates to 1.1 TW using the spatially-variable formulation for K_{GM} described in Appendix B. This is within the range of previous such estimates [Huang and Wang, 2003; Wunsch and Ferrari, 2004], and is close to the estimate by Wunsch [1998] for the globally-integrated wind work on the surface geostrophic currents.

2.3 Parameterization of eddy-driven diapycnal mixing

Based on Gent *et al.* [1995], Tandon and Garrett [1996] point out that the GM parameterization assumes, implicitly, a purely viscous dissipation of the released energy. They further argue that it is unlikely that real ocean eddies dissipate without diapycnal mixing. If, as they note, the eddy energy were dissipated locally in the ocean interior, perhaps by breaking internal waves, then the associated diapycnal diffusivity

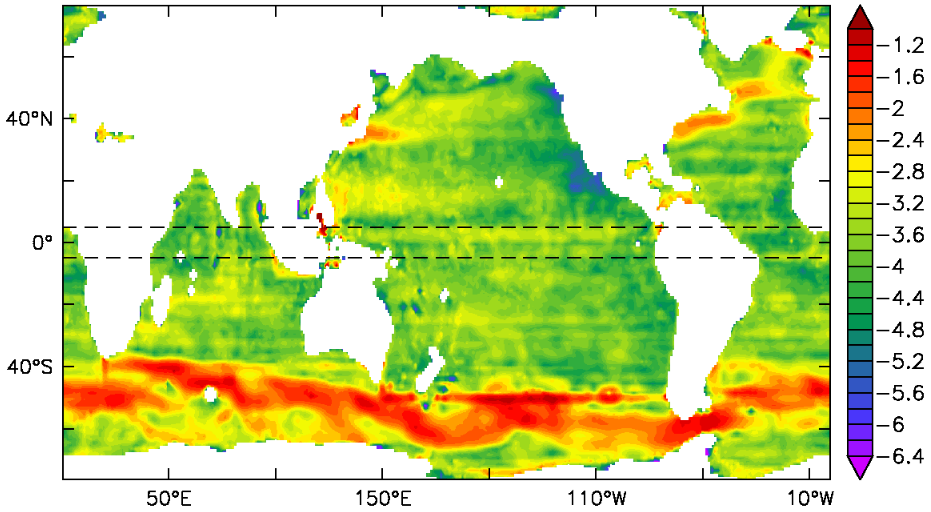

Figure 2.4: Logarithm of energy dissipated by GM-parameterized eddies between $z_1 = 200$ m and $z_2 = 2000$ m depth, $\int_{z_2}^{z_1} \rho_0 \epsilon \, \mathrm{d}z$ [W m^{-2}] with ϵ given by (2.6), diagnosed from the Levitus climatology. The dashed lines at 5°N/S bound the region where the first baroclinic Rossby radius is capped at 200 km for the computation of K_{GM}, given by (B.5). Eddy energy dissipation is strongest in the Antarctic Circumpolar Current and in western boundary currents.

could be estimated as

$$\kappa_\nu = \Gamma K_{GM} s^2, \tag{2.7}$$

where $\Gamma \approx 0.2$ is the fraction of energy dissipation ϵ that supports diapycnal mixing (with the remainder dissipating through viscous heating), and we have used the relation of Osborn [1980]:

$$\kappa_\nu = \frac{\Gamma \epsilon}{N^2}. \tag{2.8}$$

However, in order to adopt such a hypothesis of local mixing by eddy energy dissipation, there has to be a mechanism capable of transferring energy at a rate of order ϵ directly from baroclinic eddies to the internal wave field, which can be problematic [Marshall and Naveira Garabato, 2008].

Instead, as outlined in Section 2.1, barotropic eddies interacting with rough bottom-topography can generate the required internal waves, leading Marshall and Naveira Garabato [2008] to propose a new parametrization for the eddy-driven diapycnal mixing where, unlike in (2.7), much of the eddy dissipation occurs within the bottom fraction δ of the water column. Under such an assumption, (2.7) becomes

$$\kappa_\nu = \frac{\langle \Gamma K_{GM} s^2 \rangle}{\delta}, \tag{2.9}$$

for $z < -H(1-\delta)$, where H is the local ocean depth. The angled brackets represent a vertical average over the water column. Slightly modifying the suggested form of bottom-enhancement of κ_ν, we choose a smooth structure function with a constant vertical decay scale given by ζ,

$$F(z) = \frac{\exp(-(H+z)/\zeta)}{\zeta(1-\exp(-H/\zeta))}, \tag{2.10}$$

after [St. Laurent *et al.*, 2002] to bottom-enhance diapycnal mixing:

$$\kappa_\nu(x,y,z,t) = F(z) \int_{-H}^{z_{ml}} \Gamma K_{GM} s^2 \, \mathrm{d}z, \tag{2.11}$$

where z_{ml} is the local mixed layer depth. In the numerical experiments described in Chapter 4, we set $\zeta = 1000$ m and $z_{ml} = 140$ m. Since F satisfies $\int F \, \mathrm{d}z = 1$, the vertical integrals of κ_ν from either (2.7) or (2.11) are equal, and hence our numerical model runs with this parameterization shall be referred to as "κ_ν-conserving".

In addition, we will test a somewhat different approach. Namely, rather than "conserving" κ_ν over the water column below the mixed layer, such as implied by (2.9) and (2.11), we propose to conserve the energy dissipation ϵ. Furthermore, we will assume that some fraction of this energy dissipates near the bottom of the local water column and some propagates away. With these assumptions, the eddy dissipation can be rearranged to have the following form:

$$\tilde{\epsilon}(x,y,z,t) = r\,(q\hat{\epsilon} + (1-q)\bar{\epsilon})\,F, \tag{2.12}$$

where F is the same structure function as above, ϵ is given by (2.6), $\hat{\epsilon}(x,y) = \int_{-H}^{z_{ml}} \epsilon \, \mathrm{d}z$, and $\bar{\epsilon} = A^{-1} \iint\int_{-H}^{z_{ml}} \epsilon \, \mathrm{d}z \, \mathrm{d}A$, with A being the ocean area. The corresponding diapycnal diffusivity is then computed from (2.8) using the rearranged $\tilde{\epsilon}$ in place of ϵ. A fraction r of eddy energy dissipation is assumed to generate internal waves which eventually support diapycnal mixing; setting $r = 1$, this parameterization conserves the total APE released by eddies, converting it into energy supporting diapycnal mixing and is hereafter referred to as "E-conserving". Since it is possible for internal waves to transport energy far afield before breaking, a fraction $(1 - q)$ of the eddy energy is assumed to contribute to the global internal wave field and support κ_ν globally, while a fraction q is assumed to generate turbulence in the local water column. Since sloping topography is often critical to the breaking of (possibly remotely generated) internal waves [e.g. Ivey and Nokes, 1989], both the global and local energy for mixing are still bottom-enhanced in (2.12).

Chapter 3

Theory

Our theoretical understanding of the global ocean's MOC and its connection to Southern Ocean dynamics has improved markedly in recent years. The dynamics of a circumpolar channel (Drake Passage) have been cast in a zonally-averaged residual-mean framework and applied to both the upper overturning cell [Marshall and Radko, 2003] and the abyssal or lower-limb cell [Ito and Marshall, 2008]. In this chapter we examine and further develop the theory of Ito and Marshall [2008], allowing us to predict the strength of the abyssal MOC based on input parameters such as the diapycnal diffusivity κ_ν — or its parameterization in terms of other variables (Section 2.3) — the eddy transfer coefficient K_{GM}, the surface wind-stress τ, and simple aspects of the model geometry. Prior to this, however, we describe the basic theoretical setting of the abyssal MOC. This chapter finishes with an additional scaling theory for the abyssal MOC based on energetic arguments.

3.1 Circulation of the abyssal overturning cell

We begin by giving a simple, zonally averaged, intuition-building picture of the abyssal MOC and the main factors that control it. A schematic is shown in Figure 3.1. Westerly winds over a southern circumpolar channel (i.e. having no continental barriers) drive an ageostrophic northward surface Ekman flow. Geostrophic return flow can only occur below the level of highest topography in the circumpolar channel. The westerly winds strengthen moving north in the channel, hence strengthening the northward Ekman transport and creating a surface divergence that is balanced by upwelling (Ekman suction). This tilts the isopycnals in the channel, creating available potential energy upon which mesoscale eddies feed, reducing the slope of isopycnals and creating a counter-clockwise eddy-induced circulation that opposes the clockwise Eulerian-mean (wind-driven) circulation.

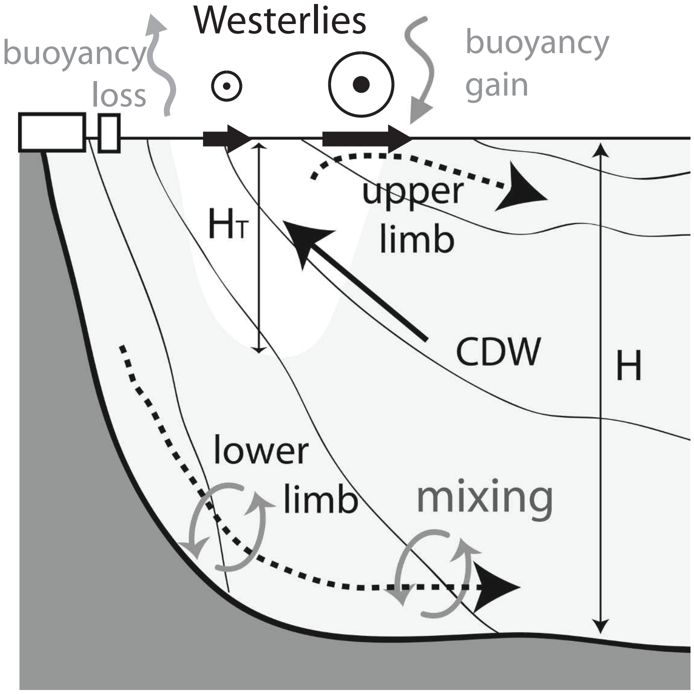

Figure 3.1: Schematic of the zonally averaged meridional overturning circulation in the Southern Ocean. The Drake Passage with no continental barriers above a depth H_T is shown in white. Northward Ekman flux at the surface is indicated by thick black arrows. Circumpolar Deep Water (CDW) upwells around the Drake Passage owing to the negative wind-stress curl. Sea-ice near the southern boundary is shown at left. Buoyancy lost by the abyssal MOC at the surface is balanced by buoyancy gain in the abyss via turbulent diapycnal mixing, illustrated by circular gray arrows. Figure adapted from [Ito and Marshall, 2008], © Copyright 2008 American Meteorological Society.

Employing the continuity equation, we can define the Eulerian-mean stream function Ψ, up to an additive constant, by

$$\left(-\partial_z\overline{\Psi}, \partial_y\overline{\Psi}\right) = \left(\overline{v}, \overline{w}\right), \tag{3.1}$$

and similarly for the eddy-induced stream function Ψ^*:

$$\left(-\partial_z\Psi^*, \partial_y\Psi^*\right) = \left(v^*, w^*\right). \tag{3.2}$$

The sum of the Eulerian-mean and the eddy-induced circulations is the residual circulation (see Appendix A):

$$\Psi^\dagger = \overline{\Psi} + K_{GM}s, \tag{3.3}$$

where $\Psi^* = K_{GM}s$ follows immediately from (3.2) and the GM eddy closure, (A.17). It is this residual circulation that represents the mass-weighted transport from both eddies and the mean flow, and is our primary concern in diagnosing the abyssal MOC. As can be seen in (3.3), the residual circulation is a balance between the Eulerian circulation ($\overline{\Psi} > 0$) and the eddy-driven circulation ($K_{GM}s < 0$).

As the residual circulation transports near-surface waters near the southern boundary southward, buoyancy is lost to the cold atmosphere. At the southern boundary (on the Antarctic shelf and underneath sea-ice in the Ross and Weddell seas of the real ocean) convection occurs and hence buoyancy is further lost. This "Antarctic Bottom Water" (AABW) then moves north in the abyss, with some upwelling along the sloped isopycnals in a relatively rapid recirculation. What water moves north past the southernmost isopycnal that outcrops, however, must then rise across deep isopycnals, gaining buoyancy in the deep to balance the buoyancy lost at the surface. This occurs through diapycnal diffusion transporting buoyancy downwards. Having then gained the required buoyancy, the water returns southward and upwells along isopycnals in the circumpolar channel to close the circulation.

Classical theories posited that the abyssal stratification was maintained by diapycnal diffusion bringing buoyancy down from the surface, but this requires a κ_ν of $\mathcal{O}(10^{-4}\ \mathrm{m}^2\ \mathrm{s}^{-1})$ [Munk, 1966], found to be an order of magnitude larger than that observed in the mid-depth ocean away from topography [Polzin *et al.*, 1997; Kunze *et al.*, 2006]. It is indeed the mid-depth diapycnal mixing that is critical here, as diapycnal mixing in the abyss, though commonly observed to be greatly elevated above mid-depth levels, cannot bring buoyancy down from the surface.

An alternative theory, proposed by Toggweiler and Samuels [1998], posits that it is the wind-work over the Southern Ocean that maintains the abyssal stratification. Wolfe and Cessi [2010] provide an illuminating study, and Nikurashin and Vallis [2011] developed their analytic model of the abyssal MOC with both this mechanism and the diapycnal mixing mechanism at work. The idea is that, by (meridionally) sloping isopycnals, the Southern Hemisphere westerlies work to connect the deep ocean interior to the mixed layer in the circumpolar channel/Southern Ocean, thereby matching the abyssal stratification with the meridional buoyancy gradient in the

Southern Ocean's mixed layer.

Nikurashin and Vallis [2011] propose the following mechanistic link between Southern Ocean wind-stress and the abyssal MOC: stronger winds increase the isopycnal slope, thereby connecting the deep ocean interior to the mixed layer at more northerly latitudes where the meridional buoyancy gradient can be larger, and hence increasing abyssal stratification; by inhibiting vertical motion, it is possible for an increase in the abyssal stratification to reduce the advective-diffusive upwelling and hence the abyssal MOC. The reliance of this argument on the surface boundary conditions shall be discussed in Section 5.1.3.

The scaling theories we develop in the next section generally rely on solving two equations for two variables: the residual circulation, $\Psi^\dagger$, and the isopycnal slope in the circumpolar channel, s. For a simple box-like geometry, Ito and Marshall [2008] derived an analytic expression for the Eulerian circulation, by beginning from the steady-state, time- and stream-wise averaged zonal momentum equation with horizontal eddy momentum fluxes neglected:

$$-\rho_0 f \overline{v} = -\frac{\Delta p}{L_x} + \frac{\partial T}{\partial z}, \tag{3.4}$$

where T is the zonal shear stress, Δp is the pressure difference across topography (which stands a height H_T above the sea-floor), and L_x is the length of the ACC around the globe. In the latitudes of Drake Passage and above the tallest topography ($z > -H_T$), $\Delta p = 0$. Below topography, however, $\Delta p \neq 0$ and this pressure difference provides the primary sink for the momentum input by the surface wind-stress. Indeed, vertically integrating (3.4) over the full fluid-column gives $\Delta p = L_x \tau (H - H_T)^{-1}$, where $\tau = T(0)$ is the surface eastward wind-stress. Then, using (3.2) and vertically integrating again, we get

$$\overline{\Psi} = (\partial_z \overline{\Psi})(z + H) \tag{3.5}$$

below the surface Ekman layer, where

$$\partial_z \overline{\Psi} = \begin{cases} -\frac{\tau}{\rho_0 f} \frac{1}{H - H_T} & (z < -H_T), \\ 0 & (z \geq -H_T). \end{cases} \tag{3.6}$$

Note the Eulerian circulation is proportional to the surface wind-stress over the circumpolar channel, $\overline{\Psi} \propto \tau$, as well as to the height above the bottom, $\overline{\Psi} \propto (z + H)$, when below topography.

The second required equation expresses a balance between the buoyancy transport accomplished by the residual circulation and by diapycnal mixing. We therefore begin with the buoyancy equation at steady state, assuming no explicit sources or sinks:

$$\mathbf{u}^\dagger \cdot \nabla_h \bar{b} + w^\dagger \partial_z \bar{b} = \partial_z \left(\kappa_\nu N^2 \right), \tag{3.7}$$

where $\mathbf{u}^\dagger = (u^\dagger, v^\dagger)$ is the horizontal residual velocity vector, $w^\dagger$ is the vertical residual velocity, ∇_h the 2D horizontal gradient operator. Note that the divergence of the along-isopycnal eddy buoyancy flux ($\nabla \cdot \overline{\mathbf{u}'b'}_{||}$ in Appendix A) has been absorbed into the residual advecting velocity so that only diapycnal buoyancy fluxes, here approximated by vertical buoyancy fluxes, remain on the RHS.

Following Karsten and Marshall [2002] and Ito and Marshall [2008], the zonal[1] average of (3.7) can be integrated, along a surface of constant buoyancy $\bar{b}$, beginning at the sea-floor for a distance $|\tilde{y}|$ (adopting the convention that $\tilde{y} < 0$ because $s < 0$) to obtain

$$\Psi^\dagger \left(\tilde{y}, \bar{b} \right) = \int_0^{\tilde{y}} \frac{1}{\partial_z \bar{b}} \frac{\partial}{\partial z} \left(\kappa_\nu \partial_z \bar{b} \right) \, \mathrm{d}\tilde{y}', \tag{3.8}$$

having assumed isopycnal slopes are generally small, $|s| \ll 1$. (This approximation holds despite $|v^\dagger| \gg |w^\dagger|$: see Ito and Marshall 2008 or Karsten and Marshall 2002 for full details.) This also ensures the meridional distance $y < 0$ travelled following an isopycnal southward as it rises from the sea-floor is very close to $\tilde{y}$. As Ito and Marshall [2008] assumed, let us suppose the buoyancy field decays exponentially with depth:

$$\bar{b} = b_0(y) \exp\left(\frac{z}{z_0} \right), \tag{3.9}$$

where b_0 is the surface buoyancy and $z_0 > 0$ is an assumed constant e-folding scale. Then (3.8) becomes

$$\Psi^\dagger \left(\tilde{y}, \bar{b} \right) = \int_0^{\tilde{y}} \left(\frac{\kappa_\nu}{z_0} + \frac{\partial \kappa_\nu}{\partial z} \right) \, \mathrm{d}\tilde{y}'. \tag{3.10}$$

This is the second equation, which forms, together with (3.3), a closed system for s and $\Psi^\dagger$. We now solve this system for a variety of parameterizations of diapycnal mixing.

---

[1] For the ACC, an along-stream average is preferable to a zonal average, but for illustration of the theory a zonal average is sufficient.

3.2 Scaling theory for the abyssal overturning

3.2.1 Constant mixing

For the purposes of a simple theory, let us assume that κ_ν is uniform and $s = \alpha z_0/\tilde{y}$ for some constant α. We shall revisit these assumptions in Appendix C. For now, (3.10) becomes [Ito and Marshall, 2008]

$$\Psi^\dagger = \alpha \frac{\kappa_0}{s}, \tag{3.11}$$

having chosen a constant value κ_0 for κ_ν. Combining (3.3) and (3.11) and solving the resulting quadratic equation for s (choosing the negative root, appropriate for the Southern Ocean), the solution for the slope and residual circulation is

$$s = -\frac{\overline{\Psi}}{2K_{GM}}(1 + \sqrt{1+\phi}), \tag{3.12}$$

$$\Psi^\dagger = \frac{\overline{\Psi}}{2}(1 - \sqrt{1+\phi}), \tag{3.13}$$

the latter illustrated by the blue curves in Figure 3.2. The dimensionless quantity ϕ reflects the relative magnitude of the mixing-driven and wind-driven circulations: $\phi \equiv 4\alpha\kappa_0 K_{GM} \left(\overline{\Psi} \right)^{-2}$. This is the scaling theory of Ito and Marshall [2008]. For $\phi \gg 1$, $\Psi^\dagger$ is predicted to scale as

$$\Psi^\dagger = -\sqrt{\alpha\kappa_0 K_{GM}} + \frac{1}{2}\overline{\Psi} + \mathcal{O}\left(\overline{\Psi}^2\right). \tag{3.14}$$

Note that even in this limit of strong wind-stress / weak mixing, $\Psi^\dagger$ is not independent of wind-stress (implicit in $\overline{\Psi}$), contrary to the assertion by Ito and Marshall [2008], except in so far as the dependence of $\overline{\Psi}$ is removed by evaluating the limit as $\overline{\Psi} \to 0$.

In this theory, stronger winds increase the slope of isopycnals, reducing the geometrical area of an isopycnal surface across which diapycnal diffusion acts; since κ_ν is constant here, this therefore reduces the diapycnal mass flux and hence the MOC. This is the physical meaning of (3.11). This prediction, as already pointed out, seems unlikely under a more realistic assumption in which κ_ν is dependent, directly or indirectly, on wind energy input [Munk and Wunsch, 1998], as we now examine.

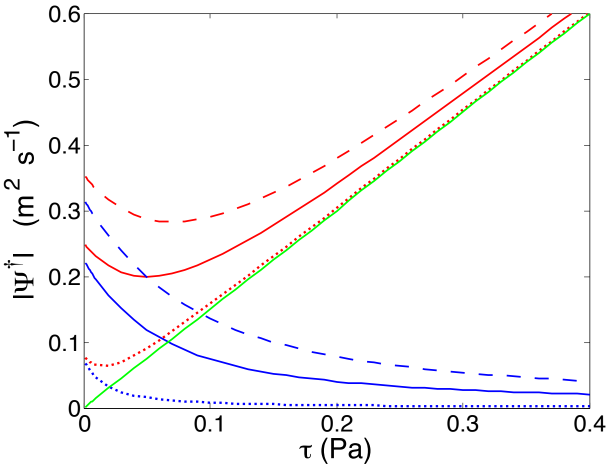

Figure 3.2: Theoretical predictions of the abyssal MOC given by (blue) Eq. (3.13), (green) Eq. (3.15), or (red) Eq. (3.17) as a function of Southern Ocean wind-stress (τ). The diapycnal diffusivity κ_ν is (blue) constant, as in [Ito and Marshall, 2008]; (green) entirely supported by eddy energy, Eq. (2.11); (red) supported by both eddy energy and a constant source, Eq. (3.16). Where applicable, the constant diffusivity is (dotted) 10^{-5} m^2 s^{-1}, (solid) 10^{-4} m^2 s^{-1}, or (dash) $2 \cdot 10^{-4}$ m^2 s^{-1}. We use $K_{GM} = 500$ m^2 s^{-1}, $\alpha = 1$, $\Gamma = 0.2$, $\rho_0 = 10^3$ kg m^{-3}, $f = -10^{-4}$ s^{-1}, and $\overline{\Psi}$ (and hence $\Psi^\dagger$) evaluated at depth 3250 m. The ocean depth is $H = 4000$ m, while the depth of tallest topography in the latitudes of the circumpolar channel is $H_T = 2750$ m.

3.2.2 Eddy mixing

We now consider extensions to the theory of Ito and Marshall [2008] based on alternative parameterizations of κ_ν discussed in Section 2.3, but we maintain that κ_ν is *uniform* — that is, we neglect the term $\partial_z \kappa_\nu$ for now. Supposing that the energy supporting diapycnal mixing comes *entirely* from eddies (or, indirectly, from the wind energy input), Saenko *et al.* [2012] modified the above scaling theory, using (2.7). In this case the equation for s is linear and the residual circulation is

$$\Psi^\dagger = -\overline{\Psi}\frac{\gamma}{1-\gamma}, \tag{3.15}$$

where $\gamma = \alpha\Gamma < 1$ since typically $\alpha < 1$ [Ito and Marshall, 2008]. Under these assumptions, $|\Psi^\dagger|$ increases linearly with wind-stress over the circumpolar channel (green curve in Figure 3.2). This captures the effect that stronger winds increase the isopycnal slope s, increasing eddy activity which increases diapycnal mixing and hence the abyssal MOC.

3.2.3 Eddy + constant mixing

Diapycnal mixing in the Southern Ocean could be non-zero even when it is not supported by wind power. For example, the tides provide another source of mechanical energy to support diapycnal mixing [Munk and Wunsch, 1998]. There may also be some other sources of mixing near the bottom [e.g. Bryden and Nurser, 2003], including those resulting from non-local energy. To obtain a simple scaling, we combine these additional mixing sources into a single constant κ_0, transforming (2.7) into

$$\kappa_\nu = \Gamma K_{GM} s^2 + \kappa_0. \tag{3.16}$$

Putting this into (3.3) and (3.11) gives a somewhat different form for $\Psi^\dagger$ than previously:

$$\Psi^\dagger = \frac{\overline{\Psi}}{2(1-\gamma)} \left(1 - 2\gamma - \sqrt{1+\phi_\gamma}\right), \tag{3.17}$$

where

$$\phi_\gamma = \frac{4\alpha\kappa_0 K_{GM}(1-\gamma)}{\overline{\Psi}^2}. \tag{3.18}$$

This is close to, but slightly more than, a linear superposition of the previous predictions, (3.13) and (3.15), for $\Psi^\dagger$ when $\kappa_\nu = \kappa_0$ and when $\kappa_\nu = \Gamma K_{GM} s^2$ (red curves in Figure 3.2.

In the limit of weak wind-stress, we recover an analogous result to (3.14)

$$\lim_{\overline{\Psi}\to 0} \Psi^\dagger = -\sqrt{\frac{\alpha\kappa_0 K_{GM}}{1-\gamma}}. \tag{3.19}$$

Note that, realistically, the background κ_0 in (3.16) may be significantly smaller than the global average κ_ν used in Section 3.2.1, leading to a much smaller $\Psi^\dagger$ in this limit; however, for better comparison κ_0 is the same for the blue and red curves in Figure 3.2. In the limit of strong wind-stress, $\Psi^\dagger$ asymptotically approaches that predicted by (3.15):

$$\lim_{\overline{\Psi}\to \infty} \Psi^\dagger = -\overline{\Psi}\frac{\gamma}{1-\gamma}. \tag{3.20}$$

Notably, (3.17) predicts a wind-stress τ_{crit} that establishes a minimum strength of the abyssal MOC.

This theory can be modified to include bottom-enhancement of κ_ν, such as by the vertical structure function F in (2.10), in which case the quantitative predictions of

$\Psi^\dagger$ are greatly enhanced, but the predictions are qualitatively the same. This theory can also be modified to account for an explicitly depth-varying isopycnal slope. These alternatives are explored in Appendix C. For now, however, we shall employ a general circulation model (Chapters 4 and 5) to explore the predictions made above.

Before doing so, we shall finish this chapter with an energetic discussion of the abyssal MOC, relating it through a simple box model to the energy consumed (or, equivalently, to the potential energy generated) by diapycnal mixing. Whereas the predictions for $\Psi^\dagger$ above are only in terms of model parameters (e.g. κ_ν, K_{GM}), in the next section the model output (specifically, the large-scale buoyancy field $\bar{b}$) as well as model parameters shall be used to predict $\Psi^\dagger$. While ultimately our qualitative predictions for $\Psi^\dagger$ come from the above predictions, additional consideration of the equilibrium buoyancy field (below) will augment our physical understanding (Chapter 5) of the response of the abyssal MOC to changes in surface wind-stress.

3.3 A simple box model

We shall now derive a simple energetic relation for abyssal MOC. To begin, integrate the buoyancy equation (3.7) horizontally over the ocean area A and vertically from the sea-floor to a depth z_d, employing continuity and assuming zero buoyancy flux across the boundaries, to get

$$\int \left(w^\dagger \bar{b}\right)\Big|_{z_d} \, \mathrm{d}A = \int \left(\kappa_\nu N^2\right)\Big|_{z_d} \, \mathrm{d}A. \tag{3.21}$$

This is nothing more than the budget of potential energy at steady state, as can be seen by substituting for buoyancy $b = -g\rho_0^{-1}\rho$, and (optionally) integrating vertically, to get

$$\int w^\dagger g\rho \, \mathrm{d}V + \int \rho_0 \kappa_\nu N^2 \, \mathrm{d}V = 0. \tag{3.22}$$

The rate of consumption of potential energy (PE) by the overturning circulation (first term) is balanced by the rate of generation of PE by diapycnal mixing (second term).

Now, consider the vertical flow across a horizontal section at depth z_d in an idealized box ocean basin of total depth H: Dense water of buoyancy b_1 convects downwards with velocity $w_1^\dagger$ in a narrow region (area A_1), perhaps near the southern boundary; this is balanced by a broad region (area A_2) of lighter water of buoyancy $b_1 + \Delta b_{z_d}$ upwelling at velocity $w_2^\dagger$. Employing mass conservation, $w_1^\dagger A_1 = -w_2^\dagger A_2 \equiv \Psi^\dagger$ (note the change of units to [m^3 s^{-1}] here), (3.21) becomes

$$(-\Psi^\dagger)\Delta b_{z_d} = \kappa_\nu N^2 A_2 \equiv \epsilon_{\mathrm{mix}} A_2, \tag{3.23}$$

where, purely for simplification, we have chosen average values for κ_ν and N^2 in the upwelling region, and approximated $\kappa_\nu N^2(A_1 + A_2) \approx \kappa_\nu N^2 A_2$ since $A_2 \gg A_1$ and N^2 is small in the convective region. Note (3.23) is not new [c.f. Eq. 3.17 from Munk and Wunsch, 1998]. It essentially says that the rate of the overturning circulation, requiring a buoyancy gain of Δb_{z_d} in the abyss, is limited by the rate of energy consumption by diapycnal mixing ($\epsilon = \Gamma^{-1}\epsilon_{\mathrm{mix}}$). The latter is directly proportional to the rate of generation of potential energy by diapycnal mixing, which can be seen from (3.22). Or, if we were to instead suppose a still state ($w^\dagger = 0$, $\mathbf{u}^\dagger = \mathbf{0}$), carrying the buoyancy tendency term $\partial_t \bar{b}$ (t being time) from the LHS of (3.7) through to (3.21), we would note that the rate of energy consumption by diapycnal mixing at depth z_d is essentially the total rate of gain of buoyancy by waters beneath z_d: $\epsilon_{\mathrm{mix}}|_{z_d} = \int_{-H}^{z_d} \partial_t \bar{b}\, \mathrm{d}z$. Thus, supposing the energy consumed by diapycnal mixing ϵ_{mix} is constant, an increased buoyancy contrast Δb_{z_d} requires the overturning $\Psi^\dagger$ in (3.23) to slow, allowing more time for the required buoyancy to be gained.

Note that Δb_{z_d} and N^2 are different quantities, though subtly and intimately related. If the dense, convecting water of buoyancy b_1 intrudes along the sea-floor and therefore sets the buoyancy at depth H in the broad upwelling region, we might suppose

$$N^2 \sim \frac{\Delta b_{z_d}}{H - z_d}. \tag{3.24}$$

As was discussed in Section 3.1, the abyssal stratification N^2 is supported by the wind-work over the Southern Ocean and hence, due to the sloping isopycnals, the surface buoyancy distribution in the Southern Ocean is an important factor for N^2. The abyssal stratification is also supported, to some extent, by deep diapycnal mixing bringing buoyancy down (either from the pycnocline in the Pacific and Indian oceans, or from North Atlantic Deep Water (NADW) in the Atlantic), and hence the diapycnal diffusivity in the ocean basin is also an important factor. On the other hand, Δb_{z_d} is strongly determined by the buoyancy contrast across and hence the eddy activity within the circumpolar channel. It may also be determined by the surface buoyancy distribution in the Southern Ocean and any diabatic processes occurring in the subsurface Southern Ocean. Because of their intimate coupling, N^2 and Δb_{z_d} are both influenced by all the factors just mentioned, and there is, we see, something of a "chicken-and-egg" relationship between N^2 and Δb_{z_d}. One informs the other, and so careful physical analysis is required to ascertain whether a change in N^2 produces (or leads, in a time-evolving sense) a change in Δb_{z_d}, or vice versa. Knowing how the models we test in this thesis differ helps us solve this "chicken-and-egg" problem, thus allowing (3.23) to help explain *why* the abyssal MOC responds as it does to certain changes in the forcings. This line of thinking is most closely applied in Section 5.1.3.

Finally, we note that, for a constant κ_ν, the box model (3.23) is related to the theory of Ito and Marshall [2008]. Indeed, zonally integrating (3.10) and employing (3.24) gives

$$\Psi^\dagger = \int_0^{\tilde{y}} \int_0^{L_x} \frac{\kappa_\nu}{z_0} \frac{N^2}{\left(\frac{\Delta b_{z_d}}{H - z_d}\right)} \, \mathrm{d}x \, \mathrm{d}\tilde{y} \sim \frac{\epsilon_{\mathrm{mix}} \tilde{y} L_x}{\Delta b_{z_d}}, \tag{3.25}$$

where L_x is the zonal distance around the globe and hence $(-\tilde{y})L_x \sim A_2$.

Chapter 4

Model Set-up

4.1 The UVic ESCM

This thesis employs version 2.9 of the University of Victoria Earth System Climate Model (UVic ESCM) [Weaver *et al.*, 2001], a model of intermediate complexity. The standard configuration of the UVic ESCM contains many components, but essentially only three are used in this study: the ocean, the atmosphere, and sea-ice.

The UVic ESCM owes the "intermediate" nature of its complexity to its atmospheric model, which is a vertically-integrated energy-moisture balance model (EMBM), first described by Fanning and Weaver [1996]. The surface wind vectors are prescribed and, together with the surface temperature from the land or the ocean component, the surface air temperature, specific humidity, and heat and freshwater fluxes are calculated, the latter two fluxes being determined by down-gradient (Fickian) eddy diffusion. These simplifications allow the model to be run rapidly, yet maintain enough complexity to allow for climate feedbacks that are suppressed by simpler atmospheric representations, such as a restoring surface boundary condition (SBC / RSBC); we shall explore the effect of these differences in Section 5.1.3.

The sea-ice model is a thermodynamic-dynamic model that predicts ice thickness, surface temperature, and areal fraction. Heat fluxes from the atmosphere and ocean as well as the usual radiative fluxes determine the ice melt or growth rates, assuming that the ice has no heat capacity and thus is in constant balance with the heat fluxes. The momentum budget follows elastic-viscous plastic dynamics, incorporating internal stresses as well as the surface wind-stress and the oceanic stress from below. For further details, we refer the reader to Weaver *et al.* [2001].

The ocean model is a fully dynamic, 3D general circulation model: version 2.2 of the Geophysical Fluid Dynamics Laboratory (GFDL) Modular Ocean Model (MOM) [Pacanowski, 1995]. Sub-grid scale eddy mixing is parameterized according to Gent and McWilliams [1990]; the eddy transfer coefficient K_{GM} we employ is non-uniform and prognostically determined by the local baroclinicity and Rossby radius (see Appendix B for full details), or in simpler experiments is set to a uniform constant of 800 $\mathrm{m}^2\ \mathrm{s}^{-1}$. The ocean model contains a full explicit vertical convection scheme [Pacanowski, 1995]. Especially in convective regions, the isopycnal slope can be very large which causes issues for numerical stability; therefore the slope tapering scheme of Gerdes *et al.* [1991] is used with a maximum slope threshold of 10^{-2}. Small-scale diapycnal mixing is parameterized by a term

$$\nabla \cdot (\kappa_\nu \nabla \phi) \tag{4.1}$$

in the tendency equation for a tracer ϕ, where the coordinate system implicit in the 3D gradient operator ∇ is rotated to match isoneutral surfaces. We test several parameterizations of κ_ν.

Tracer advection on the numerical grid is by way of flux corrected transport (FCT). Other computationally expedient advection schemes include the upstream and central difference schemes; the latter has higher-order accuracy (less implicit numerical diffusion) but is subject to numerical dispersion in the form of non-physical oscillations of the advected quantity near sharp fronts. These oscillations may create negative concentrations of a positive-definite quantity — they may violate the second law of thermodynamics. This problem is often resolved by *explicitly* introducing additional diffusion to mix away these oscillations. Of particular importance to this thesis, there is a vertical component of this (explicit and implicit) numerical diffusion, which then sets a lower bound on the amount of physical vertical / diapycnal diffusion that can be specified and accurately modelled. The FCT scheme blends the upstream and central difference schemes to achieve minimal numerical diffusion without creating non-physical oscillations. The procedure, described by Zalesak [1979], is often to locally average the upstream and central difference advective fluxes, weighted towards the central difference flux, but limited so that no new tracer minima or maxima are created by advection in the adjacent grid cells. Gerdes *et al.* [1991] analyzed these three advection schemes in a coarse resolution North Atlantic sector model and found that, in steady state, the thermocline is least diffusive under the FCT scheme.

To ensure that the levels of diapycnal mixing we specify in our models are accurately modelled, rather than dominated by numerical diffusion, we ran an initial test model with κ_ν set to 10^{-5} m^2 s^{-1} uniformly below the surface mixed layer. A weak basin-scale abyssal MOC was observed at 1.0 Sv. This MOC grew to 1.5 Sv when we increased κ_ν to 2×10^{-5} m^2 s^{-1}, indicating that even at this low level of diapycnal diffusivity, the abyssal MOC is driven by physical, not numerical, diffusion. Thus, we are confident that the models tested in this thesis, with $\kappa_\nu \geq 10^{-5}$ m^2 s^{-1} everywhere (and basin averages of $\kappa_\nu \geq 10^{-4}$ m^2 s^{-1} in the abyss), are dominated by physical, not numerical, diffusion.

The geometry of the model is as follows. The horizontal resolution is 2° × 2° for all model components. The ocean model and has 27 vertical levels that increase parabolically in thickness from 20 m at the surface to 280 m in the deepest layer. The basin is an idealized box geometry, 56° by 156° (longitude-latitude), representative of the Atlantic Ocean and its Southern Ocean sector (Figure 4.1), containing a 12° wide and 4° long zonally re-entrant channel of depth 2750 m representative of Drake Passage. Aside from this sill, the ocean bottom is flat at 4050 m depth. (The rough bottom topography assumed by our bottom-enhanced parameterizations of κ_ν need not be resolved.) There is a thin (one grid cell) strip of land surrounding the ocean. The prescribed surface wind-stress is a zonally uniform analytic function [Weaver and Sarachik, 1990] that captures the dominant features of the observed zonal winds (Figure 4.2, solid black line). For these "control" winds, the maximum stress of the westerlies over the Southern Ocean is $\tau_c = 0.2$ Pa.

This model is first spun-up from a uniform state for 10,000 years, with κ_ν set to the "Bryan-Lewis" profile described in the next section. The meridional profile of the simulated surface buoyancy flux is shown in Figure 4.2. The resulting equilibrium state is then used as an initial condition for experiments, run for 5,000 years, with alternative parameterizations of diapycnal mixing and varied wind-stress. In some experiments, we also use a restoring SBC, in which case the restoring temperature and salinity fields are taken from the surface climatology of the corresponding experiment run with the EMBM atmosphere at control winds, and the restoring timescale is 15 days for both temperature and salinity.

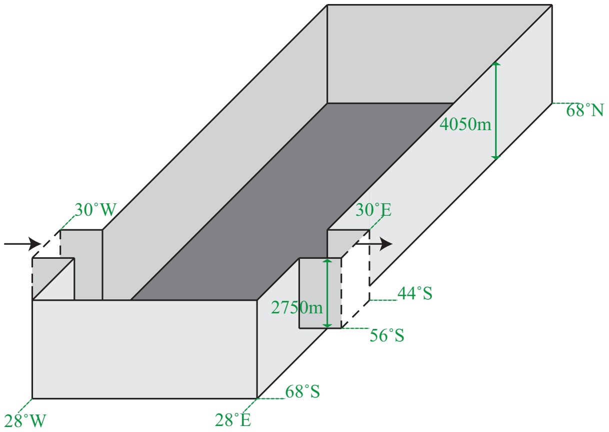

Figure 4.1: The idealized ocean basin geometry for the general circulation model used in this thesis. Black arrows indicate the channel in the south has periodic boundary conditions. Convergence of lines of longitude are not shown here.

4.2 Experimental set-up

We modify the "control" model described above with different parameterizations of diapycnal mixing, and we explore their response to variations in the wind-stress. First we discuss the diapycnal mixing parameterizations. The first is a constant vertical profile after Bryan and Lewis [1979], increasing from $1.3 \cdot 10^{-5}$ m^2 s^{-1} in the upper ocean to 10^{-4} m^2 s^{-1} in the abyss with a smooth change around 2000 m depth (hereafter referred to as the "Bryan-Lewis" experiment). Next is the "κ_ν-conserving" experiment with κ_ν given by (2.11). The "Fixed" experiment is a variant on this, having κ_ν and K_{GM} taken from the "κ_ν-conserving" experiment at control winds, and held fixed even as wind-stress is varied. Next is the "Combined" experiment with κ_ν the sum of (2.11) and the "Bryan-Lewis" profile, representing energy for mixing coming from both the winds/eddies and a constant source. Last is the "E-conserving" experiment with eddy dissipation energy given by (2.12) and mixing computed via $\kappa_\nu = \Gamma\tilde{\epsilon}/N^2$.

Scott *et al.* [2011] estimate the rate of lee wave generation associated with interaction of geostrophic flows with topography to be roughly 50% of the wind energy input to the large-scale circulation. Keeping this in mind, for comparative purposes so that the "E-conserving" globally averaged κ_ν profile would be similar to that of the "κ_ν-conserving" case (Figure 4.4), we choose $r = 0.5$. The remaining fraction $(1 - r)$ of eddy energy is dissipated by means other than internal lee wave generation, such as

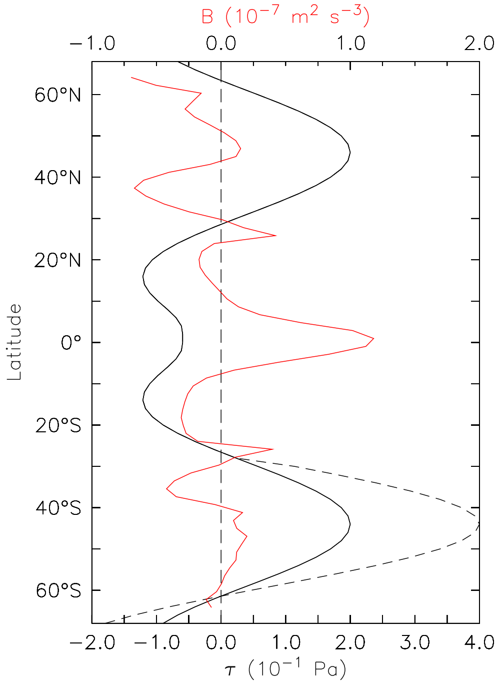

Figure 4.2: Black: The idealized zonally uniform wind-stress (τ) and (dashed) an example of its perturbation. Red: The zonally-averaged surface buoyancy flux (B) diagnosed from the "Bryan-Lewis" experiment with control winds.

those due to bottom drag, air-sea interaction, the transfer of eddy energy to the mean flow, etc. We also chose $q = 0.4$ to roughly fit some previous estimates [St. Laurent and Garrett, 2002; Nikurashin and Ferrari, 2010]. The simulated ocean circulation will be sensitive to the choice of q and r, but their physically-based estimation[1] is beyond the scope of this work.

Some additional restrictions are added to the model, which we now outline. The threshold isopycnal slope of 10^{-2} is also used as a maximum slope when computing the eddy energy dissipation or diapycnal diffusivity from the (squared) slope. For numerical stability and because $N > |f|$ for geophysical flows, we restrict $N^2 \geq 10^{-8}$ s^{-2}. All parameterizations have a minimum value for κ_ν which is set to the observed background level of turbulent mixing: $\kappa_\nu \geq 10^{-5}$ m^2 s^{-1}. Furthermore, since the parameterization (2.7) of Tandon and Garrett [1996] assumes the thermal wind

---

[1] Indeed, our choice for r is particularly arbitrary, given that not all wind energy input is dissipated by eddies (see Section 4.3).

balance, which is not valid in the Ekman layer, the eddy mixing parameterizations are not applied near the surface; instead we set $\kappa_\nu = 10^{-4}$ m^2 s^{-1} in the upper 140 m for all models.

This jump of κ_ν can lead to a downward vertical buoyancy diffusion that is, at this particular depth, comparable to Ekman pumping: that is, $|\partial_z \kappa_\nu| \sim |w_{Ek}| \sim 10^{-6}$ m s^{-1}, with Ekman pumping w_{Ek} at this depth dominating $w^\dagger$ in (3.7). Mixed layer κ_ν parameterizations akin to ours are typically used in idealized models to mimic strong wind-driven mixing in the upper ocean [e.g. Shakespeare and Hogg, 2012]. Note that a smoother transition of κ_ν to elevated mixed layer values spreads out, but does not remove, this effect. Thus, for this idealized study focusing on the abyssal circulation, we believe our mixed layer κ_ν parameterization to be adequate.

Due to anthropogenic climate change, both observations [Marshall, 2003] and numerical simulation [Fyfe and Saenko, 2006] show an increasing trend in the mid-latitude Southern Hemisphere westerly wind-stress; a poleward shift in the maximum of these westerlies is also a possibility, though a less robust result than the increasing strength [Marshall, 2003]. Based on the theory of Chapter 3, we expect the abyssal MOC to respond very differently to changes in the Southern Hemisphere westerly wind-stress when different parameterizations of diapycnal mixing are employed; thus for the practical reasons of long-term climate projection, this is our primary interest.

We shall investigate this question through simple perturbations to the winds. Let τ be the maximum wind-stress of the Southern Hemisphere westerlies (at 44°S in the model, coincident with the northern edge of the circumpolar channel), and as already noted, $\tau_c = 0.2$ Pa is the "control" value of τ. We perturb the control wind-stress field by way of a multiplicative factor (τ/τ_c) south of 30°S, which is where most wind energy is input to the ocean [Wunsch, 1998] and is similar to where winds have been perturbed in previous, related studies [e.g. Nikurashin and Vallis, 2011]. An example is shown by the dashed line in Figure 4.2. These, our main experiments, shall be referred to as "SOW" (Southern Ocean Winds). In another set of experiments, we apply a multiplicative factor to the global wind-stress field — an experiment more in geophysical fluid dynamics than future climate change. These experiments shall be referred to as "GFD".

4.3 Model verification

Before analyzing the numerical results under altered winds, we first present some model results at control winds for comparison with real ocean data. The wind energy input to the large-scale ocean circulation, calculated as the dot product of the surface wind-stress vector with the large-scale ocean surface velocity, is 0.32 TW regardless of the κ_ν parameterization. Given the estimated 1 TW of wind-work on the real ocean [Wunsch, 1998], and our model domain being 22% of the real ocean area, this rate of wind-work is somewhat too high and will contribute to a larger κ_ν in models where wind/eddy-energy supports mixing. The wind-work should be compared with the globally integrated eddy energy dissipation from and energy consumed by mixing, given in Table 4.1. In round numbers, the GM-parameterized eddies consume about 30% of the wind energy input.

Model	**Eddy energy dissipation (TW)**	**Mixing energy consumption (TW)**
"Bryan-Lewis"	0.092	0.10
"κ_ν-conserving"	0.086	0.10
"Combined"	0.093	0.15
"E-conserving"	0.090	0.092

Table 4.1: Globally integrated (below 140 m depth) eddy energy dissipation ($\rho_0\epsilon = \rho_0 K_{GM} N^2 s^2$ from (2.6)) and energy consumed by mixing ($\kappa_\nu N^2 \rho_0/\Gamma$ from (2.8)), at control winds for various diapycnal mixing parameterizations.

Considering the "E-conserving" model, the rate of energy consumption by mixing should be a fraction $r = 0.5$ of the eddy energy dissipation rate, exactly. However, the restriction $\kappa_\nu \geq 10^{-5}$ m^2 s^{-1} artificially adds mixing energy. Removing this restriction results in a rate of energy consumption by mixing of 0.047 TW, indeed close to $1/2$ the eddy energy dissipation rate. Even with the weak background mixing of 10^{-5} m^2 s^{-1} used here, this energetic addition is surprisingly large because it is active in the mid- and upper-ocean where N^2 is highest. Due to the bottom-enhancement by $F(z)$ in (2.12) and the low abyssal stratification, this criterion does not tend to apply itself in the abyssal ocean.

The "κ_ν-conserving" model (2.11), despite having "$r = 1$" implicitly should also have less energy consumed by mixing than eddy energy dissipation. Indeed, while local eddy dissipation, (2.7), would give equal eddy dissipation and mixing energy

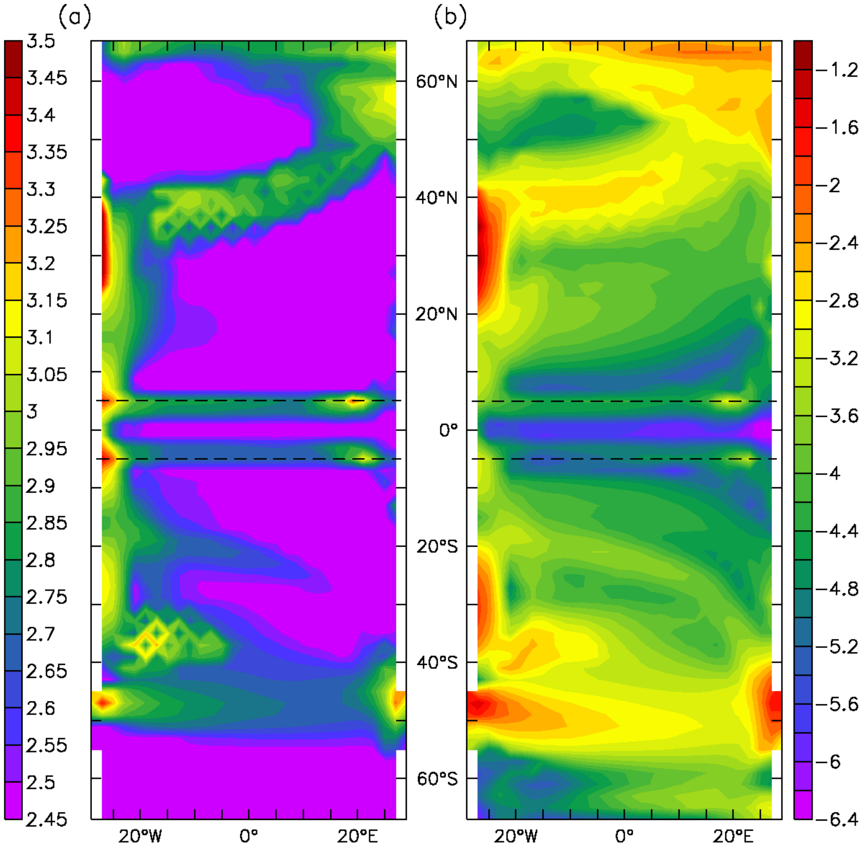

Figure 4.3: (a) Logarithm eddy transfer coefficient K_{GM} [m^2 s^{-1}] and (b) logarithm of energy dissipated by GM-parameterized eddies between $z_1 = 200$ m and $z_2 = 2000$ m depth, $\int_{z_2}^{z_1} \rho_0 \epsilon \, \mathrm{d}z$ [W m^{-2}] with ϵ given by (2.6), both from the "Bryan-Lewis" model at control winds. The dashed lines at 5°N/S bound the region where the first baroclinic Rossby radius is capped at 200 km for the computation of K_{GM}, given by (B.5).

consumption, the bottom-enhancement of κ_ν pairs large κ_ν with small N^2, reducing the total energy consumed by mixing. This gap is slightly overcompensated for by the artificial energy input inherent in restricting $\kappa_\nu \geq 10^{-5}$ m^2 s^{-1} (Table 4.1).

Having both eddy energy and a constant energy source supporting mixing, the "Combined" model has significantly more energy consumed by mixing than is dissipated by eddies alone. The extra mixing energy, we can imagine, comes from the tides.

The spatially variable eddy transfer coefficient K_{GM} is shown in Figure 4.3a. It is elevated in regions of strong baroclinicity, particularly in the ACC and western boundary currents. The spatial structure of the eddy energy dissipation simulated

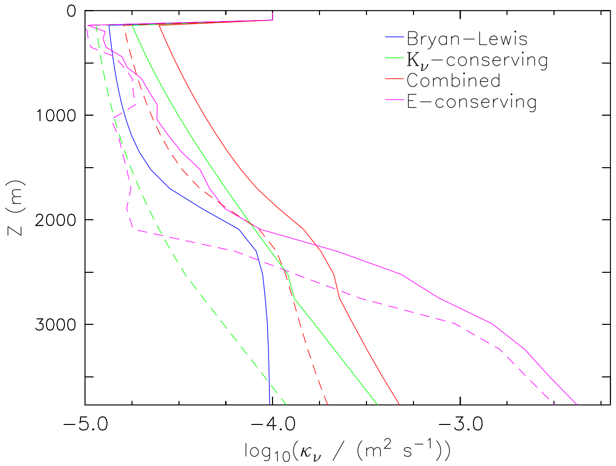

Figure 4.4: The diapycnal mixing coefficient κ_ν (solid) globally averaged, or (dash) averaged between 40°S and 40°N for (blue) "Bryan-Lewis" mixing, (green) "κ_ν-conserving, (red) "Combined", and (magenta) "E-conserving" experiments. The "Fixed" experiment in which κ_ν is taken from "κ_ν-conserving" is not shown. Above 140 m depth, κ_ν is set to 10^{-4} m^{2}s^{-1} in all experiments.

by the model, shown in Figure 4.3b, broadly resembles the corresponding field diagnosed from the Levitus data (Figure 2.4), though somewhat weaker in the ACC and somewhat stronger in the western boundary currents.

Depth profiles of κ_ν at control winds for our parameterizations are shown in Figure 4.4. Considering the "κ_ν-conserving" and "E-conserving" models, the diapycnal diffusivity is 1×10^{-3} m^2 s^{-1} and 3×10^{-3} m^2 s^{-1}, respectively, averaged over the bottom 800 m in the latitudes of the circumpolar channel. While large, diapycnal diffusivities of $\mathcal{O}(10^{-3})$ are found near the sea-floor over rough topography in the ACC [Sheen *et al.*, 2013], and even from observationally constrained inverse methods, basin-mean estimates of the abyssal diffusivity could be as high as $\mathcal{O}(10^{-3})$ [Ganachaud and Wunsch, 2000; Ganachaud, 2003]. Thus we believe our experiments serve well as sensitivity studies. The modelled spatial distribution of abyssal κ_ν, overlain with the abyssal stratification, is illustrated in Figure 4.5.

Lastly, Figure 4.6 compares the zonally averaged stratification for several models with that from the Levitus climatology. Without a continental slope at the southern boundary where deep convection occurs, the model's stratification in that region is too low. The stratification is also somewhat too low in the "E-conserving model" throughout the abyss. This may be due to the fact that wind energy conversion to diapycnal mixing is most strongly bottom-enhanced in this model (Figure 4.4), to the

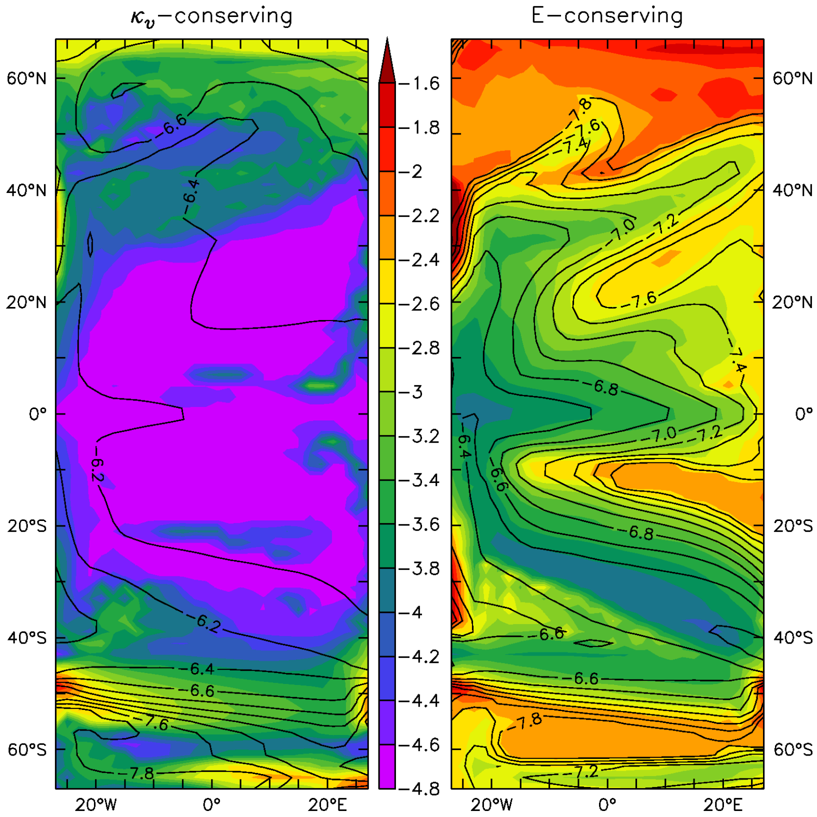

Figure 4.5: (Colours) logarithm of κ_ν [m^2 s^{-1}] and (contours) logarithm of N^2 [s^{-2}] averaged over the bottom 1000 m at control winds for the (left) "κ_ν-conserving" and (right) "E-conserving" models. In both models κ_ν is large around the model ACC and western boundary currents plus their extensions. In the "κ_ν-conserving" model (left), elevated κ_ν is largely contained to these regions, while in the "E-conserving" model (right), the two properties that (i) a fraction of the mixing energy is globally redistributed and (ii) $\kappa_\nu \propto N^{-2}$, effectively elevate κ_ν throughout the global abyss.

extent that diapycnal mixing in the abyss tends to mix away abyssal stratification. Otherwise, the modelled stratification compares well with the Levitus climatology.

4.4 Measuring the abyssal overturning

Before determining changes to the abyssal MOC under different mixing parameterizations and winds (Chapter 5), we must first decide how to compute the stream function, and then choose a metric for the abyssal MOC based on the chosen stream function. There are three common choices for the stream function Ψ: it can be a function of latitude and depth, of latitude and (potential) density, or of depth and

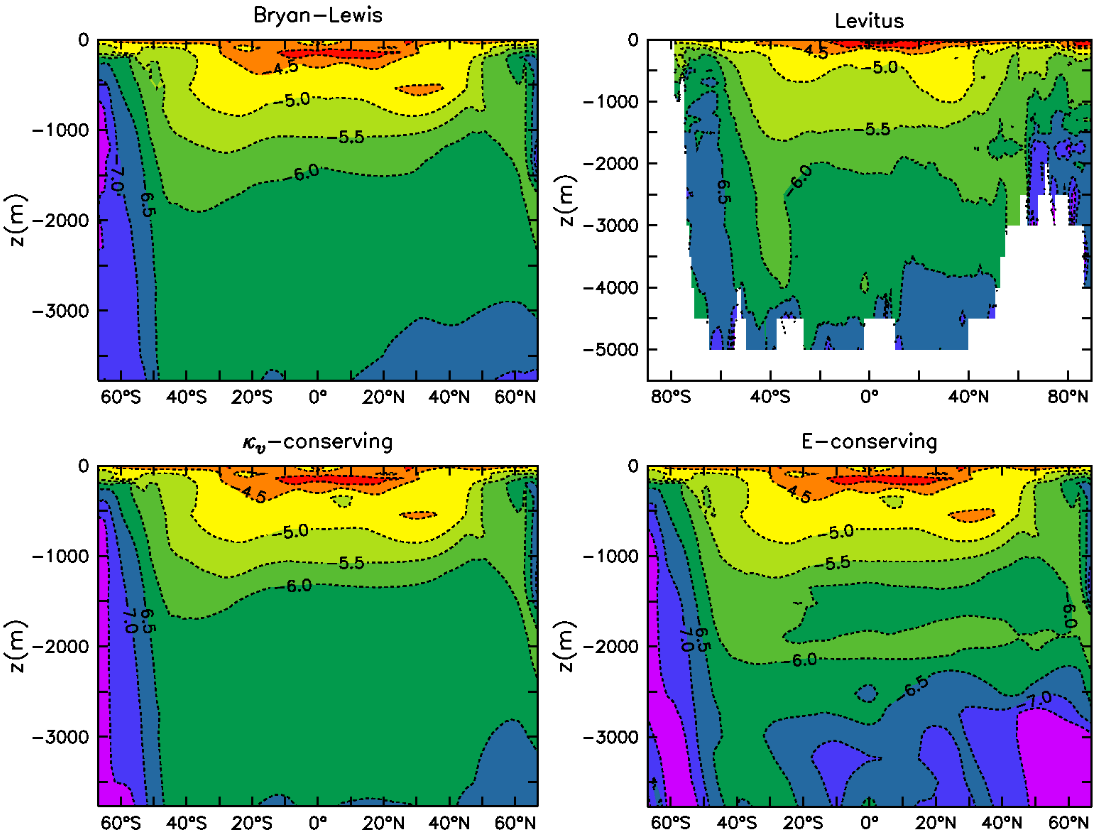

Figure 4.6: Logarithm of zonally averaged stratification [s^{-2}] for three model experiments at control winds, as well as from the Levitus climatology in the Atlantic Ocean and corresponding sectors of the Atlantic and Arctic Oceans. Contour interval is 0.5.

(potential) density. We consider the latitudinal extent of the abyssal MOC, in particular whether it extends northward of the circumpolar channel or primarily recirculates in the Southern Ocean, to be an important feature (critically affecting the time-scale of climate feedbacks involving the abyssal ocean) and hence do not study the MOC in depth-density space.

For comparison, Figure 4.7 shows an example of the stream function from our model in both latitude-depth and latitude-density space. The model reproduces the subtropical cells, Southern Ocean upwelling, and deep water formation in both hemispheres. The simulated AABW is injected in the south, with a fraction of it recirculating locally and the rest moving northward. The latter is then gradually converted to lighter waters by diapycnal mixing in a broad region north of about 20°S, before joining the model's NADW and returning back to the south.

To interpret the stream function in latitude-density space, note that upward ver-

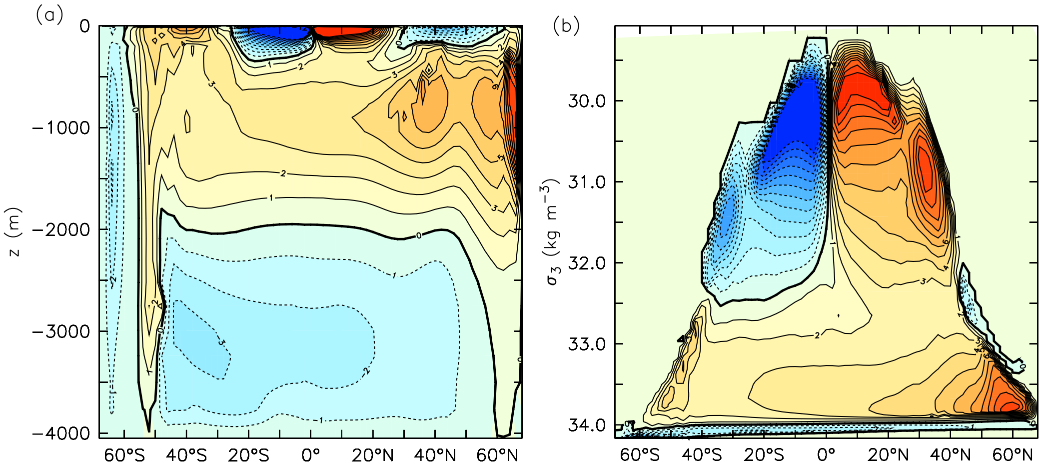

Figure 4.7: The zonal-average residual stream function for the "Bryan-Lewis" model at control winds $\tau_c = 0.2$ Pa, plotted as a function of (a) latitude and depth, or (b) latitude and potential density referenced to 3 km depth. Negative values (blue) indicate counter-clockwise flow, positive values (red) clockwise flow. The thick black line is the zero contour. Contour interval is 1 Sv, but contours beyond ±12 Sv are not shown. A zoomed-in view of the densest water classes is shown in the bottom left panel of Figure 5.1.

tical tendencies (following the direction of the flow) indicate buoyancy gain, which, away from the surface, must be by diapycnal mixing; downward vertical tendencies indicate buoyancy loss usually by cabbeling or convection. However, considering the RHS of the buoyancy equation (3.7), $\kappa_\nu\ \partial_{zz}\bar{b} + \partial_z\kappa_\nu\ \partial_z\bar{b}$, local buoyancy loss due to diapycnal mixing is possible, particularly in the case of strong bottom-enhancement of mixing, though likely uncommon.

Note the modelled Deacon cell around 50°S that appears as a dominant feature in the Southern Ocean circulation when working in latitude-depth space is largely eliminated in latitude-density space, showing it to be a largely adiabatic flow [Döös and Webb, 1994]. This strikingly illustrates why it is more physically relevant to work in latitude-density space. Since our purpose is to study parameterizations of diapycnal mixing that affect diabatic transformations, we primarily work in latitude-density space; the residual stream function is [Döös and Webb, 1994, Eq. 4.1]

$$\Psi^\dagger(\theta,\sigma_3) = \int_0^{2\pi}\int_{z(\phi,\theta,\sigma_3)}^0 v^\dagger(\phi,\theta,z')R\cos\theta\ \mathrm{d}z'\mathrm{d}\phi, \tag{4.2}$$

where θ is latitude, ϕ is longitude, σ_3 is potential density referenced to 3000 m depth, and $v^\dagger$ is the residual (see Appendix A) northward velocity.

To emphasize the portion of the abyssal overturning that extends northward of the circumpolar channel and forms a basin-scale counter-clockwise ($\Psi^\dagger(\theta, \sigma_3) < 0$) circulation (Figure 4.7), our chosen metric is the average, over the latitude range $\theta_1 =$ 42°S to $\theta_2 =$ 30°S, of the minimum value of $\Psi^\dagger(\theta, \sigma_3)$ restricted to the lower cell. For convenience, we denote this metric simply as $\Psi^\dagger$, with no arguments. Mathematically,

$$\Psi^\dagger = \frac{1}{\theta_2 - \theta_1} \int_{\theta_1}^{\theta_2} \min\{\Psi^\dagger(\theta, \sigma_3) \ : \ \sigma_3 > \sigma_3^{(abyss)}(\theta)\} \, \mathrm{d}\theta, \tag{4.3}$$

where $\sigma_3^{(abyss)}(\theta)$ is the minimum zonal-average σ_3 associated with the abyssal MOC at latitude θ.

Chapter 5

Numerical Results

We now consider the response of the abyssal MOC to changes in the surface wind-stress. The numerical model we employed in this thesis, while set to have an idealized basin geometry, represents a very complex ocean-climate system. Moreover, most of the mixing parameterizations (Section 2.3) we test have spatially-variable κ_ν. Therefore we should not expect the scaling theory of Section 3.2 to closely and quantitatively match our numerical results; rather, they are meant to serve us as a qualitative guide.

The "GFD" experiments are considered (briefly) in Section 5.2, but first we study the "SOW" experiments in depth. In addition to the differing behaviour arising from the various diapycnal mixing parameterizations (Section 5.1.1), we examine the two primary features of our model that differ from ocean-only models previously used to study the abyssal MOC's sensitivity to winds, mixing, and eddies. These features are (a) the eddy transfer coefficient K_{GM} that reacts to the ocean baroclinicity (Section 5.1.2) and (b) the energy-moisture balance model (EMBM) atmosphere and sea-ice model which together alter the surface boundary conditions (Section 5.1.3). We begin the discussion, however, with both these model options active, to illustrate the key result of this thesis (Section 5.1.1).

To aid understanding, let us briefly summarize the effects of the variable K_{GM} scheme and the EMBM + sea-ice model under changed wind-stress. While our formulation (B.5) for K_{GM} is somewhat complex, it is useful to think of it as essentially proportional to the isopycnal slope, $K_{GM} \sim K|s|$ for some constant $K > 0$. Stronger winds steepen isopycnals and make eddies more efficient.

The SBC's are different in two primary ways. First, as the zonal wind-stress τ is increased, we also increase the zonal wind velocity U, according to the standard quadratic bulk formula $\tau = c_D \rho_a U|U|$, where $c_D = 10^{-3}$ is the dimensionless drag coefficient and $\rho_a \sim 1$ kg m^{-3} is a reference surface air density [Gill, 1982]. This increases the air-sea buoyancy exchange rate, for example allowing more buoyancy loss as water upwelled in the circumpolar channel moves south to AABW formation sites. Second, by pulling sea-ice north, stronger Southern Ocean westerlies (north of 61°S in the model; see Figure 4.2) serve to hasten the formation of sea-ice and hence, via brine rejection, form denser AABW.

In what follows, "Southern Ocean" ("basin") shall refer to that part of the domain south of and including (north of) the circumpolar channel or to that part south (north) of 30°S where winds are perturbed (unperturbed), as appropriate from the context.

5.1 Perturbing the Southern Ocean winds

5.1.1 Response to wind energy input

The residual overturning stream function is illustrated for control and doubled wind-stress under several κ_ν parameterizations in Figure 5.1. Generally, we find the abyssal MOC intensifies under stronger winds, especially the recirculation in and south of the circumpolar channel. In the "κ_ν-conserving" case, diapycnal mixing is rather weak in the low-latitudes and so AABW extends north to around 60°N (near the formation sites of NADW where mid- to upper-level stratification is weak, isopycnal slopes are large, and diapycnal mixing in the water column is therefore large) before strongly upwelling and returning south. In contrast, the "Bryan-Lewis" experiment, with horizontally uniform diapycnal mixing, displays a rather linear change of abyssal $\Psi^\dagger(\theta, \sigma_3)$ with latitude. With stronger bottom-enhancement of diapycnal mixing (Figure 4.4), the "E-conserving" model exhibits rapid near-bottom diabatic transformation and hence an MOC that is strongly bottom-localized.

Using the metric (4.3), Figure 5.2 shows the basin-scale overturning for our main experiments. Considering collectively the "κ_ν-conserving", "Combined", and "E-conserving" experiments, in which eddy energy directly supports bottom-intensified diapycnal mixing, the rate of abyssal MOC ($|\Psi^\dagger|$) increases markedly with increasing wind-stress (τ). This is in broad agreement with the theoretical predictions, referring to (3.15) or (3.20) or Figure 3.2. Physically, stronger winds steepen isopycnals in the Southern Ocean, providing more energy to (parametrized in the model) eddies; this energy supports diapycnal mixing near the sea floor which converts dense AABW to Lower Circumpolar Deep Water (LCDW) and NADW; LCDW upwells in the

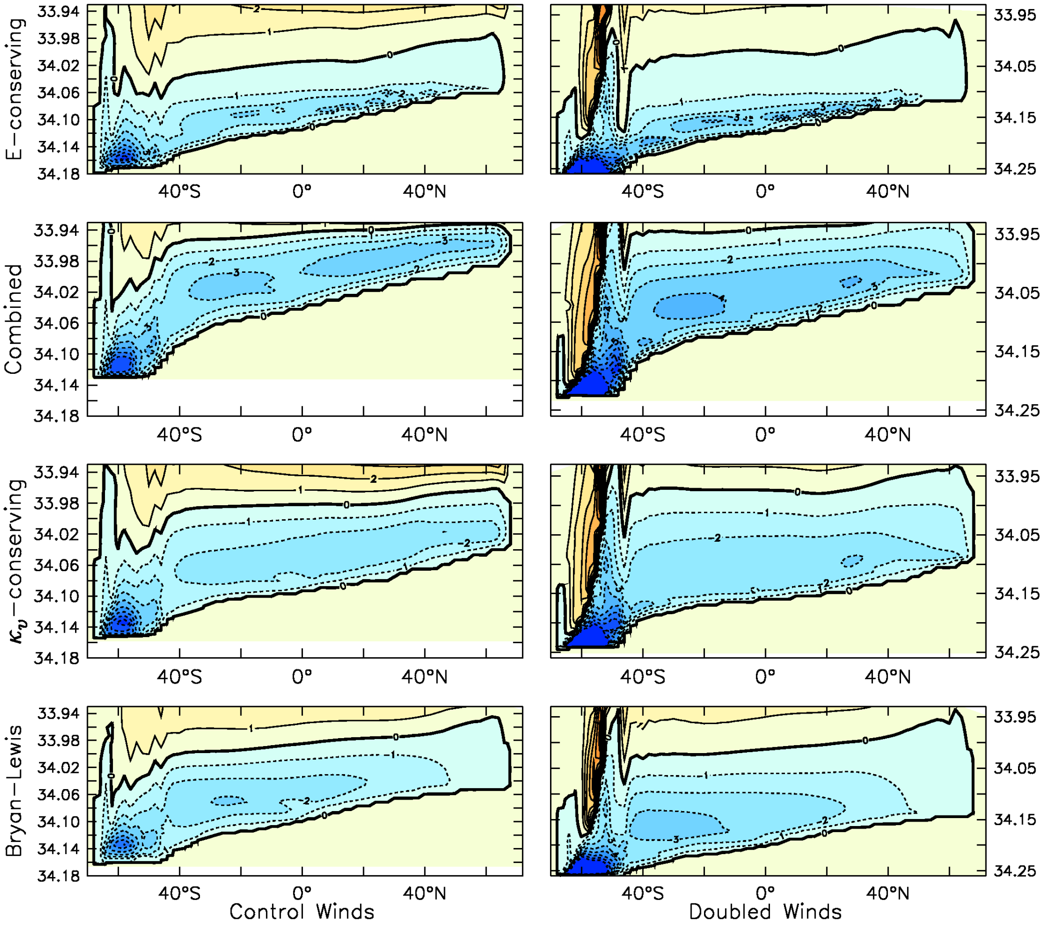

Figure 5.1: The residual overturning stream function $\Psi^\dagger(\theta, \sigma_3)$ as a function of latitude and potential density referenced to 3 km, focusing on the abyssal MOC, for (left) control wind-stress or (right) doubled wind-stress over the Southern Ocean. Results for four different parameterizations of κ_ν are shown (indicated at left). Contour interval is 1 Sv but contours beyond ±8 Sv are not shown.

Southern Ocean, closing the abyssal MOC.

However, there is a range in the abyssal MOC response to changes in the winds (Figure 5.2). This is not surprising given the different assumptions about the energy sources for diapycnal mixing in these simulations. Notably, experiments with unvarying κ_ν also display a (typically modest) strengthening of $\Psi^\dagger$ with τ, and a collapse of $\Psi^\dagger$ at low τ. As will be discussed in the following sections, this seeming discrepancy with the theoretical predictions (Ito and Marshall 2008; Nikurashin and Vallis 2011; Section 3.2) appears to be due to (a) the eddy transfer coefficient, K_{GM} (formulated in Appendix B), that can change in response to wind-driven changes in

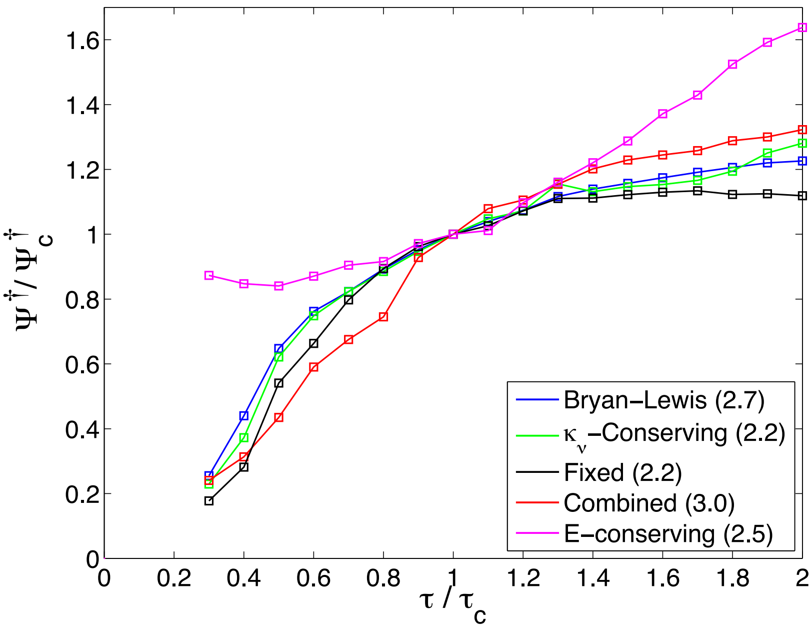

Figure 5.2: Dependence of the strength of the abyssal MOC ($\Psi^\dagger$) north of the circumpolar channel on Southern Ocean wind-stress (τ). Numbers in parentheses indicate $\Psi_c^\dagger$ [Sv], the value of $\Psi^\dagger$ at control winds $\tau_c = 0.2$ Pa.

the ocean baroclinicity, and (b) the use of ocean-atmosphere-sea-ice coupling which, while simple, allows for important feedbacks between ocean circulation and surface climate.

Further insight on the behavior of the abyssal MOC in our numerical experiments may come from considering the energetics of the system. Recalling Section 3.3, particularly (3.23), the rate of abyssal overturning is expected to be proportional to the energy consumed by diapycnal mixing, ϵ_{mix}, and inversely proportional to the buoyancy contrast that the overturning must overcome, Δb_{z_d}. Recall that if ϵ_{mix} is fixed, an increase in Δb_{z_d} requires the overturning to slow, allowing more time for the required buoyancy to be gained via diapycnal mixing. Furthermore, note that if z_d, the depth at which terms in (3.23) are measured, is taken near the level of maximum $w^\dagger$ in the abyssal basin (approximately 3 km, see Figure 4.7a), then Δb_{z_d} may reflect a buoyancy difference between AABW and NADW: the former entirely sets the buoyancy at depth z_d near the southern boundary, but, owing to diapycnal mixing, it is a mix of the two that sets the buoyancy at depth z_d in the ocean basin. Since we modify winds only over the Southern Ocean in the “SOW” experiments, this can be important under the EMBM atmosphere, as we shall see.

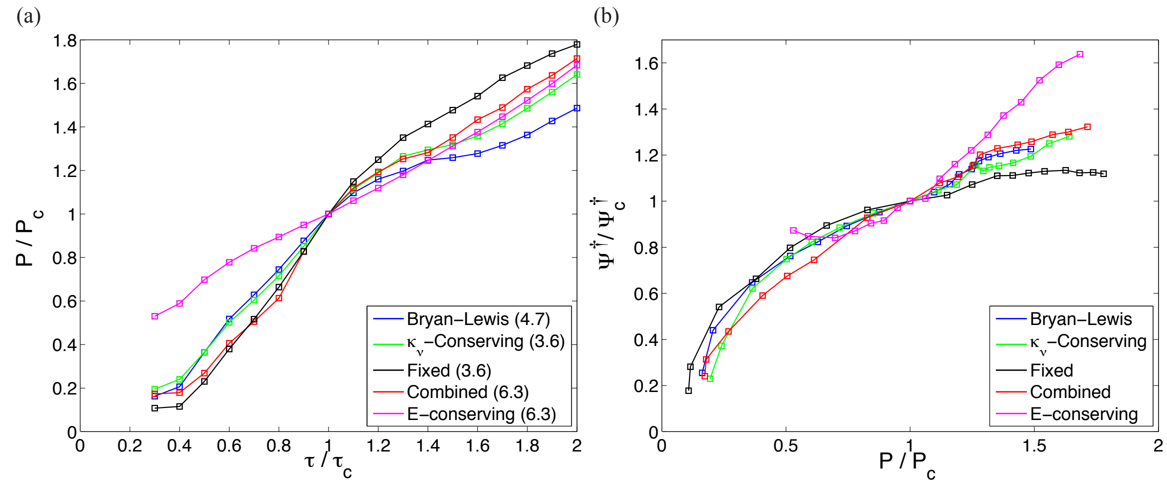

Figure 5.3: (a) Relative potential energy generated by diapycnal mixing, P, from (5.1), as a function of Southern Ocean wind-stress τ. Numbers in parentheses indicate P_c [GW], the value of P at $\tau = \tau_c$. (b) Relative $\Psi^\dagger$ (as in Figure 5.2) as a function of P.

Consider the rate of potential energy generation by diapycnal mixing (recalling (3.22)) in a region V below 2 km depth and between 43°S and 61°N,

$$P = \int \rho_0 \kappa_\nu N^2 \, \mathrm{d}V, \tag{5.1}$$

with ρ_0 a reference density. For all parameterizations tested here, P increases with wind energy input to the ocean (Figure 5.3a). However, except for the "E-conserving" case in which some eddy energy radiates away from the fluid column where it is released, κ_ν changes little (or not at all) in the ocean basin since the winds are perturbed only over the Southern Ocean. Hence, this increase of P is largely due to an increase of stratification in the ocean basin. Recalling Figure 3.1 and Section 3.1, stronger Southern Ocean winds can increase the interior stratification by connecting the interior ocean basin to the mixed layer at more northerly latitudes (as seen in Figure 5.4) where the meridional buoyancy gradient, which is projected along isopycnals to the interior stratification, can be greater. Similarly, weaker Southern Ocean winds can decrease the interior stratification and hence decrease P. Based on these changes in interior stratification, Nikurashin and Vallis [2011] argue that, under stronger Southern Ocean winds, the abyssal MOC should weaken. As we shall see, however, when κ_ν is set to be independent of wind energy input to the ocean as was assumed in

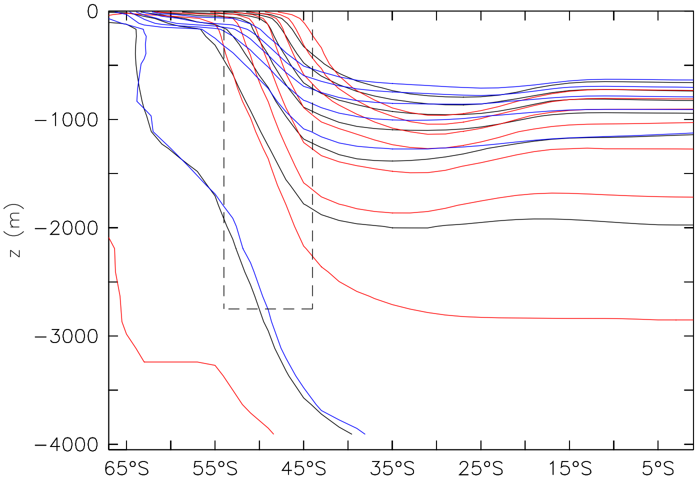

Figure 5.4: Zonal average potential density referenced to 2 km depth (σ_2) in the southern hemisphere, for the "Bryan-Lewis" model. Southern Ocean wind-stress is (black) at control levels $\tau_c = 0.2$ Pa, (red) doubled, or (blue) halved. The uppermost contour shown is $\sigma_2 = 33.5$ kg m^{-3}, and the contour interval is 0.1 kg m^{-3}. The dotted black lines bound the circumpolar channel. Stronger winds over the channel steepen isopycnal slopes, which reduces stratification in the deep ocean basin north of the channel. Broadly, the isopycnal structure compares well with the conceptual structure of Figure 3.1.

the theory of Nikurashin and Vallis [2011], the response of abyssal MOC to winds depends on the formulations employed for K_{GM} and the surface buoyancy.

Consider increasing the winds over the Southern Ocean. While, ultimately, it is the potential energy generated by diapycnal mixing which is necessary to convert dense bottom water to lighter water and to drive the abyssal MOC, the relationship between $\Psi^\dagger$ and P varies between models and is not always linear (Figure 5.3b). This is most strikingly exhibited by the "Fixed" model, where both κ_ν and K_{GM} are held fixed, unaffected by the changes in the wind-stress. In this model, P increases strongly with wind-stress beyond τ_c (Figure 5.3a), as expected due to increasing stratification, but $\Psi^\dagger$ does not (Figure 5.2 or 5.3b). Rather than driving a faster MOC, the extra P works against an increased buoyancy contrast Δb_{z_d}, which increases with winds faster when K_{GM} is fixed: essentially, Δb_{z_d} increases under stronger winds (to be discussed in Section 5.1.3), but a variable (strengthening with winds) K_{GM} more efficiently removes the available potential energy inherent in a larger Δb_{z_d} (to be discussed further in Section 5.1.2, particularly Figure 5.7). Note the "Fixed" model, uniquely in this thesis, employs a constant but non-uniform K_{GM}. Modifying "Fixed" to use the variable K_{GM} scheme, $\Psi^{\dagger}$ as well as P track those of the "Bryan-Lewis" experiment quite closely with changes in τ, although the detailed structure of $\Psi^{\dagger}(\theta, \sigma_3)$ is different (not shown).

The "E-conserving" model, on the other hand, shows a strong and fairly linear increase of $\Psi^{\dagger}$ for $\tau > \tau_c$ and/or for $P > P_c$ (Figure 5.2 and Figure 5.3b), and this increase is notably stronger than for the "κ_ν-conserving" or "Combined" models. To understand this, recall that our choice of metric of the abyssal MOC (4.3) is focused on the circulation of, and hence the buoyancy gained by, deep waters north of the circumpolar channel. Because the "E-conserving" model redistributes 40% of wind/eddy energy globally and converts it to diapycnal mixing, it has elevated rates of mixing in the deep ocean basin (away from the Southern Ocean). Since AABW will extend as far north as necessary for the buoyancy provided by diapycnal mixing to match the buoyancy lost elsewhere in the overturning circulation, this drives a strong basin-scale abyssal MOC in response to wind energy input in the south. In contrast, when eddy energy supports diapycnal mixing only in the local fluid column such as in the "κ_ν-conserving" and "Combined" models, highly elevated mixing is localized to near the region of the ACC. Thus, while the Southern Ocean wind-stress τ is increased and buoyancy losses at the surface south of the channel hasten (Section 5.1.3), this change may be largely compensated for by an increased buoyancy gain of AABW beneath the ACC by diapycnal mixing. The result is a strong abyssal MOC that does *not* significantly extend into the basin north of the channel, translating into a weaker response of $\Psi^{\dagger}$ with τ than for the "E-conserving" model (Figure 5.2).

While this recirculation south of the channel may be strongest in the "κ_ν-conserving" model, it is present in all models, particularly at high winds (Figure 5.5; see also Figure 5.1). Naveira Garabato *et al.* [2007] provide evidence for such a short-circuiting of AABW in the real Southern Ocean. Consider (in a zonal average) the isopycnal that outcrops just at the southern boundary. Waters below this isopycnal experience no surface buoyancy loss, and hence are highly unstratified. Thus, stronger winds driving faster upwelling in the channel through Ekman suction can easily intensify the circulation below this isopycnal. In contrast, waters participating in the abyssal MOC that are above and north of this isopycnal experience significant buoyancy loss near the surface as they move toward the southern boundary, and this buoyancy must be regained in the abyss by diapycnal mixing. Hence, the circulation above and north of this isopycnal does not necessarily intensify simply because upward vertical velocities in the channel are increased. To the extent that it does not

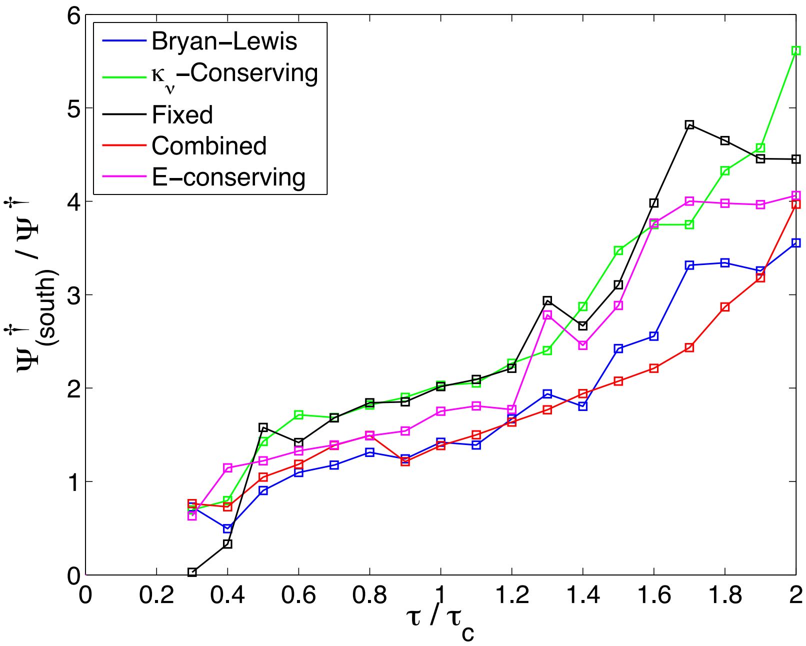

Figure 5.5: Ratio of recirculation in the Southern Ocean to the basin-scale abyssal MOC, indicating the degree to which the abyssal MOC short-circuits the upwelling pathway in the main ocean basin, instead upwelling in the circumpolar channel. As in Figure 5.2, $\Psi^\dagger$ is calculated by the metric (4.3), and $\Psi^\dagger_{\text{(south)}}$ by the same metric but with the average performed between the southern boundary and the northern edge of the circumpolar channel at 44°S.

intensify, the faster upwelling drives a stronger upper MOC and short-circuiting lower MOC.

Let us now consider the effect of weakening winds over the Southern Ocean. In all models except the "E-conserving" model, the abyssal MOC collapses (Figure 5.2). When κ_ν does not explicitly[1] depend on N^2 (as in all our models other than the "E-conserving" model), P decreases fairly linearly through decreasing N^2 as winds are weakened (Figure 5.3a). From (3.23), as $P \propto \epsilon_{\text{mix}}$ decreases, so too does $|\Psi^\dagger|$.

In contrast, the "E-conserving" model conserves the product of κ_ν and N^2, and hence P is maintained at low Southern Ocean winds by the (unperturbed) winds over the basin (Figure 5.3a). Furthermore, being tightly linked to N^2, Δb_{z_d} decreases under weaker Southern Ocean winds. It also decreases because weaker winds pull less sea-ice off-shelf and hence AABW becomes fresher; with NADW relatively unaffected, the buoyancy contrast between AABW and NADW is diminished, decreasing Δb_{z_d} (this

---

[1] For κ_ν of the form (2.6) for example, it depends *implicitly* on N^2 through s.

is further discussed in Section 5.1.3). The increase of $\Psi^\dagger$ below a critical wind-stress is thus predicted by (3.23).

Note that, because of the global redistribution of a fraction $(1-q)$ of eddy energy, it is appropriate to think of the "E-conserving" model as having two energy sources for mixing: one in the Southern Ocean, and one in the basin. So, we may expect it to behave (qualitatively) as predicted by (3.17) and illustrated in Figure 3.2, displaying a minimum of $\Psi^\dagger$ at a critical wind-stress. Uniquely, it does (Figure 5.2). The "Combined" model, with κ_ν akin[2] to (3.16), also has two energy sources supporting mixing and was designed to test the increase of $\Psi^\dagger$ below some critical wind-stress. That it shows no such increase at low winds (owing to the collapse of P — Figure 5.3a), indicates the importance of conserving energy, rather than κ_ν, if $\Psi^\dagger$ is to be display a minimum at some critical wind-stress. Furthermore, a variant of the "E-conserving" model with $q = 1$ (i.e. with eddy energy dissipating entirely in the local water column) exhibits no such increase at low winds (not shown), indicating the importance of redistributing energy for mixing if a minimum of $\Psi^\dagger$ is to be observed.

Introducing simpler ocean models

The model we use, with its EMBM atmosphere and variable eddy transfer coefficient, is different from the ocean-only models previously employed in sensitivity studies of the abyssal MOC [Ito and Marshall, 2008; Nikurashin and Vallis, 2011; Shakespeare and Hogg, 2012]. Nikurashin and Vallis [2011] define a non-dimensional number ε representing the contribution to the MOC of diapycnal diffusion relative to that of the winds: $\varepsilon \sim \kappa_\nu \, \tau^{-1}$. For $\varepsilon \ll 1$ (weak mixing relative to winds), the abyssal MOC scales as $\Psi^\dagger \sim \tau^{-1}$ in their theory, while for $\varepsilon \gg 1$ (strong mixing relative to winds), it is independent of wind-stress. For our "Bryan-Lewis" model, ε is in the range[3] 0.1 to 0.3, and hence we should expect a decay, though perhaps only weakly, of the abyssal MOC under strengthened winds. We find such a decay, but only when using restoring SBC's and a constant K_{GM} (Figure 5.6). With κ_ν fixed to the "Bryan-Lewis" profile, the abyssal MOC is relatively insensitive to increases in the Southern

---

[2] For the "Combined" κ_ν, the eddy-mixing term is bottom-enhanced and the constant term is from the "Bryan-Lewis" profile, but this should not alter the qualitative prediction.

[3] Here ε is calculated, as per Eq. 2.21b in Nikurashin and Vallis [2011], as a ratio between diffusion-driven upwelling in the ocean basin and Southern Ocean Ekman transport: $\varepsilon = (\int w^\dagger \mathrm{d}A) \, |L_x \tau / (f \rho_0)|^{-1}$, with the residual vertical velocity $w^\dagger$ averaged over the depths corresponding to the abyssal MOC, the area A covering 40°S to 40°N, and the zonal distance $L_x \sim 4000$ km and Coriolis parameter $f \sim -10^{-4}$ s^{-1} evaluated at the circumpolar channel.

Ocean wind-stress beyond τ_c, changing by at most $\sim 20\%$ for a doubling of wind-stress. Nonetheless, the variable K_{GM} scheme and the EMBM atmosphere tend to cause the abyssal MOC to increase with winds, while a constant K_{GM} and restoring SBC's tend to cause it to decrease.

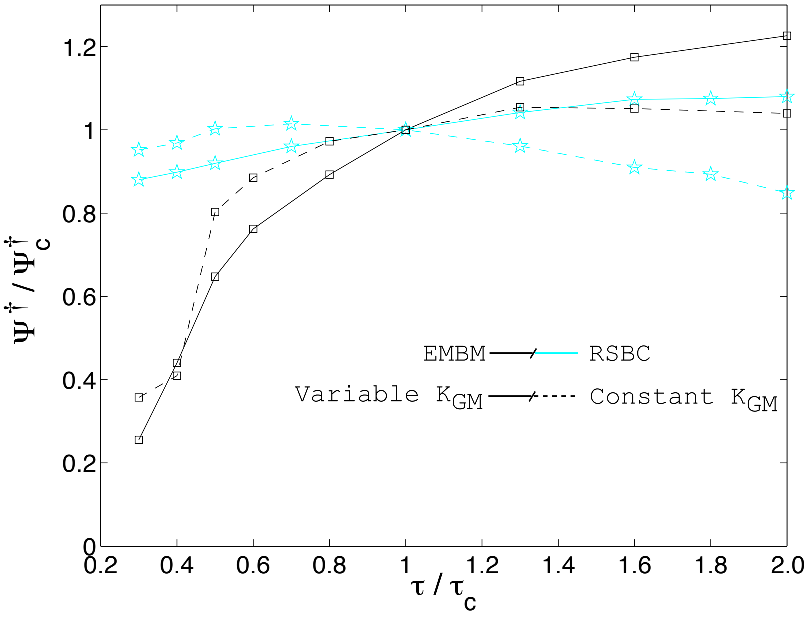

Figure 5.6: The abyssal MOC, as in Figure 5.2 but for model variants with the "Bryan-Lewis" mixing scheme. K_{GM} is variable (solid lines) or constant (dashed lines). Either the energy moisture balance model atmosphere (black, squares, EMBM) or restoring surface boundary conditions (cyan, pentagrams, RSBC) are used.

5.1.2 Role of a variable eddy transfer coefficient

The impact of variable K_{GM} on the meridional structure of buoyancy at mid-depths is illustrated in Figure 5.7. Consider increasing the wind-stress over the Southern Ocean. In response, the buoyancy contrast across the channel is significantly increased, regardless of the surface boundary conditions. However, under the (implicitly) wind-dependent K_{GM}, much of the associated available potential energy is removed from the mean state by the more active (though parametrized) eddies. As a result, while the eddy energy is largest around 50°S, the weaker increase in the meridional buoyancy gradient within the channel under the variable K_{GM} scheme gets projected into the region north of the Southern Ocean. That is, Δb_{z_d} increases less under the variable K_{GM}, which, recalling (3.23), causes a greater increase of $\Psi^\dagger$.

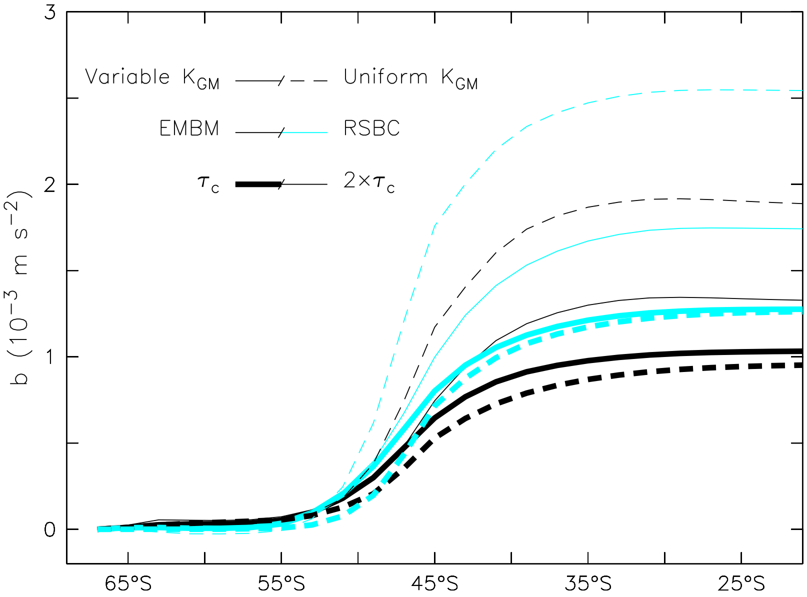

Figure 5.7: Zonal mean buoyancy averaged between 2300 m and 2750 m depth, relative to that at the southern boundary, for variants of the model with "Bryan-Lewis" mixing and either (thick lines) control winds or (thin lines) doubled wind-stress over the Southern Ocean.

Additionally, we may argue that since the eddy-induced overturning in the abyssal Southern Ocean is in the same direction as the residual circulation $\Psi^\dagger$, the variable K_{GM} scheme tends to increase the response of $\Psi^\dagger$ to changes in wind-stress (relative to the corresponding experiments with a constant K_{GM}). This increased sensitivity of $\Psi^\dagger$ to wind-stress under the variable K_{GM} formulation can be seen in Figure 5.8 across the models tested in this thesis.

5.1.3 Role of surface boundary conditions

Together, the EMBM atmosphere and the sea-ice model significantly alter the ocean circulation's response to changes in wind-stress. One of their primary effects is that the model AABW becomes significantly denser (lighter) as Southern Ocean wind-stress is increased (decreased) (Figure 5.9). As mentioned in the introduction to this chapter, stronger westerlies push (via Ekman transport) sea-ice northward faster, and hence allow faster formation of fresh ice near the southern boundary, and hence, via the brine rejected to the ocean during sea-ice formation, form denser AABW. Furthermore, as wind-stress is increased the wind-speed is increased accordingly, in-

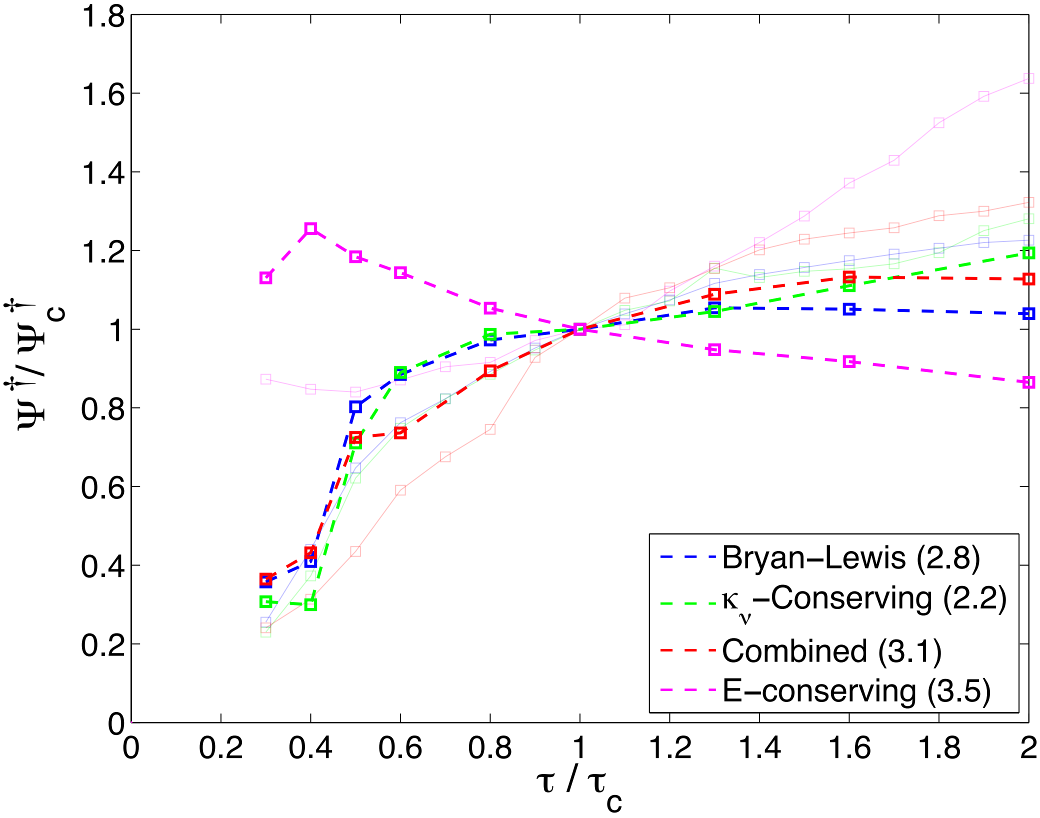

Figure 5.8: Dependence of the abyssal MOC ($\Psi^\dagger$) north of the circumpolar channel on the Southern Ocean wind-stress (τ) for (thick, dashed) constant $K_{GM} = 800$ m^2 s^{-1} or (faint, solid) variable K_{GM}. Numbers in parentheses indicate $\Psi^\dagger_c$ [Sv], the value of $\Psi^\dagger$ at control winds $\tau_c = 0.2$ Pa with constant K_{GM}.

creasing air-sea interaction, causing the ocean to lose more heat to the cold polar atmosphere. Now, where the abyssal and upper meridional overturning cells meet in the deep ocean basin (around 2 km depth, see Figure 4.7a), stratification is heavily influenced by the density contrast between AABW and NADW, the latter being relatively unaffected since winds are unperturbed over the ocean basin. This effect is clearly seen in Figure 5.10b: Under the EMBM atmosphere with sea-ice, N^2 at 2 km depth approximately doubles when doubling Southern Ocean wind-stress. This effect is not present under the restoring SBC since the density of AABW is not significantly altered. With κ_ν unvarying, as in this "Bryan-Lewis" experiment, this increase in N^2 under the EMBM at stronger winds actually increases the energy consumed by mixing ϵ_{mix}, and hence can increase $\Psi^\dagger$ via (3.23).

However, invoking (3.23) also requires consideration of the horizontal buoyancy

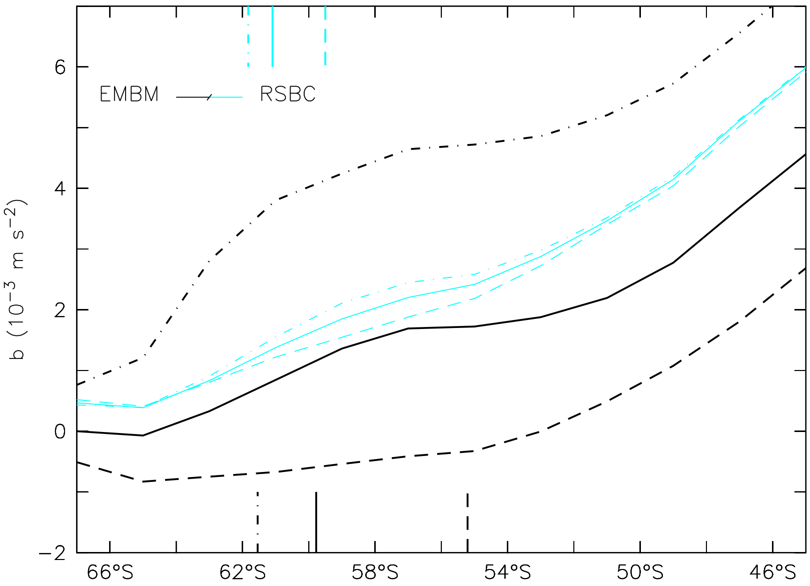

Figure 5.9: Zonally averaged buoyancy in the upper 140 m in the Southern Ocean for two variants of the "Bryan-Lewis" model: EMBM (black) or RSBC (cyan), both employing the variable K_{GM} scheme (these results are similar for constant K_{GM}). Wind-stress over the Southern Ocean is (solid lines) at control levels, (dashed lines) doubled, or (dash-dot lines) halved. Buoyancy is relative to that at the southern boundary with control winds and the EMBM atmosphere. Vertical lines at the bottom (top) show the latitude at which the zonally averaged isopycnal at 2500 m depth and just north of the circumpolar channel reaches the base of the mixed layer for the EMBM (RSBC) model.

contrast Δb_{z_d}. Figure 5.9 shows how the EMBM allows the mixed layer buoyancy and its derivatives to change in response to changes in the wind and the MOC. The mixed layer meridional buoyancy profile in the Southern Ocean is mapped, via sloping isopycnals, into the ocean interior (a crucial element to the theory of Nikurashin and Vallis [2011]; see also Section 3.1). To the extent that the circumpolar channel dynamics are adiabatic[4] the horizontal buoyancy contrast Δb_{z_d} across the channel at depth z_d is approximately the buoyancy contrast Δb_0 in the mixed layer between the southern boundary and the outcrop of the isopycnal that is just north of the circumpolar channel at depth z_d. The latter latitude is shown by vertical indicators in Figure 5.9. Stronger winds steepen isopycnals, pushing this location northward, which, under RSBC, increases Δb_0. Under the EMBM, however, more significant than the outcrop

---

[4] This approximation is made by Nikurashin and Vallis [2011], on the grounds that, with κ_ν uniform, most of the diabatic transformation of AABW will occur in the ocean basin owing to its much larger area.

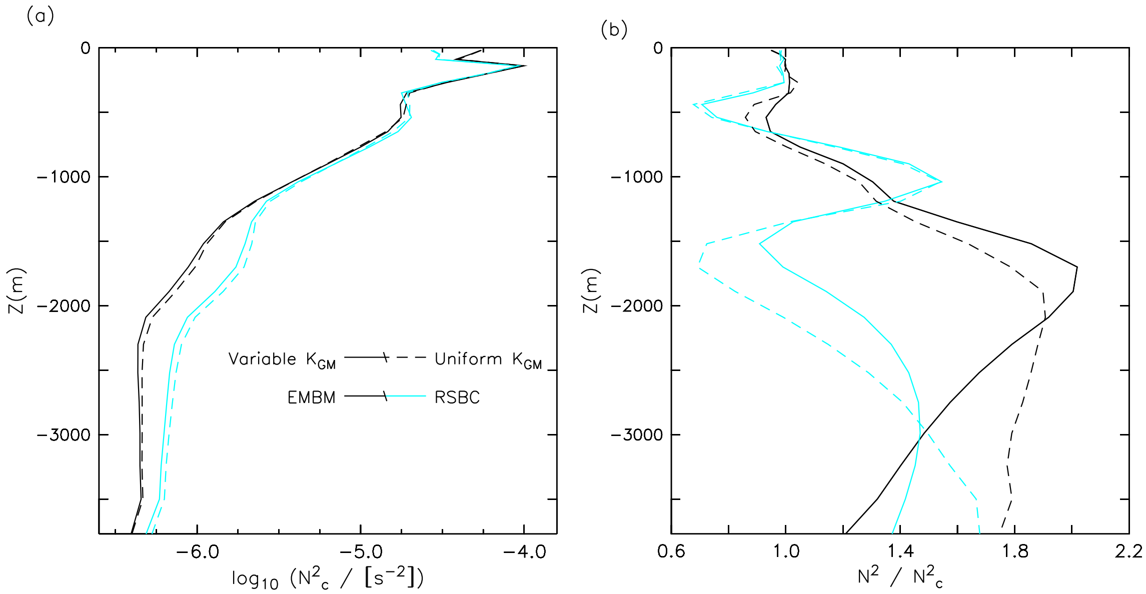

Figure 5.10: Stratification, averaged zonally and in the basin, 40°S to 40°N, for variants of the model using the "Bryan-Lewis" mixing parameterization. (a) Depth profile of stratification at control wind-stress (N_{c}^2 [s^{-2}]; note the logarithmic scale). (b) Ratio between area-averaged N^2 at doubled and control wind-stress, with the same legend as in (a).

latitude is the alteration of the meridional buoyancy profile by altered wind-stress, such that stronger winds actually reduce Δb_0 (Figure 5.9). Translating these surface changes downward along isopycnals, we see Δb_{z_d} increases with winds more[5] under RSBC than EMBM (corroborated in Figure 5.7). Combining this behaviour of Δb_{z_d} with that of N^2, the EMBM tends to increase $\Psi^\dagger$ with winds, relative to the RSBC, as seen from (3.23).

The significant changes in the surface meridional buoyancy profile are likely due to sea-ice. Examine Figure 5.11. Sea-ice forms in the south-eastern corner (the corresponding brine rejection is seen in the upper panels) and is pushed west by the polar easterlies, harbouring in the south-west corner (hatching in lower panels). This piles the ice higher, but also pushes it slowly northward via its own internal dynamics (internal stress tensor), where it begins to melt, leaving a strong freshwater anomaly (positive buoyancy anomaly) around 60°S near the western boundary (upper

---

[5] Despite Δb_0 decreasing under the EMBM at stronger winds, Δb_{z_d} nonetheless consistently increases. This appears to be due, at least in part, to stronger buoyancy loss during convection under the EMBM.

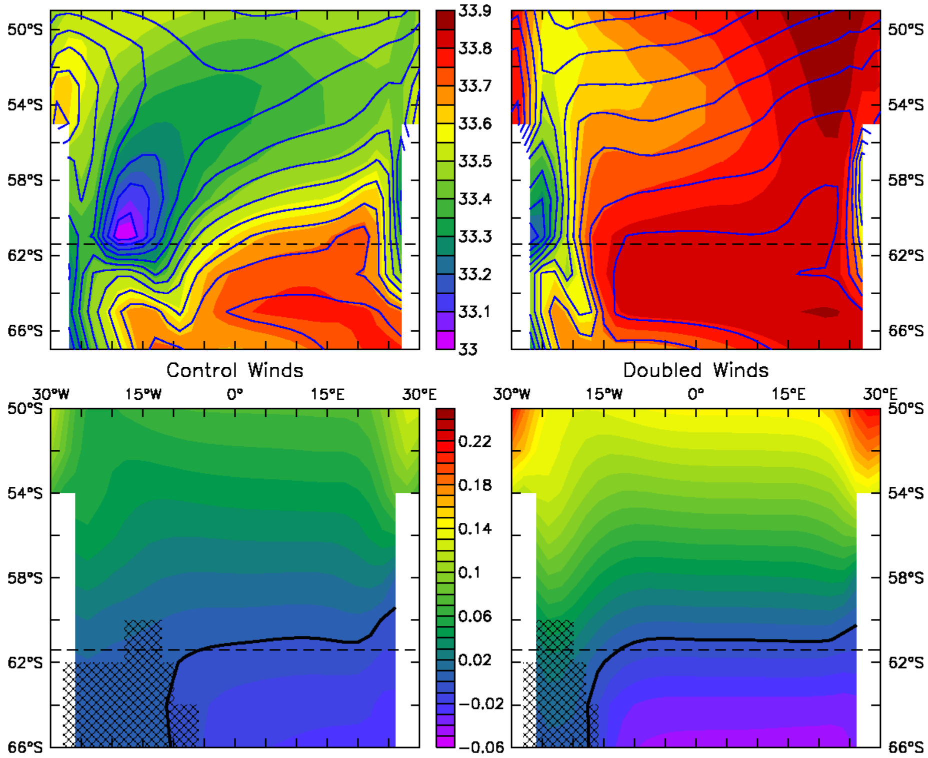

Figure 5.11: Relating the surface velocity and salinity distribution in the Southern Ocean, in the “Bryan-Lewis” model with the EMBM and sea-ice present, and a variable K_{GM} scheme. Wind-stress is at control (doubled) levels in the left (right) panels. Upper panels: sea surface salinity (colours); sea surface buoyancy (blue contours, with interval 0.05 m s^{-2}). Lower panels: Eulerian-mean northward surface velocity [m s^{-1}]. The thick line is the zero contour. Hatching indicates grid-cells with average sea-ice thickness ≥ 0.2 m. Sea-ice does exist north (east) of this area, but it is in the late (early) stages of its life-cycle. North (south) of the dashed black line, the mean winds are westerly (easterly).

left panel). This net transport of freshwater away from the bottom-water formation region is essential to forming salty bottom water, and is the classic picture of how bottom water is formed in the Weddell Sea [Gill, 1973]. This meltwater causes the positive buoyancy anomaly seen in the zonal average sections at control and low winds (Figure 5.9, black curves). Furthermore, the sea surface temperature being slightly above the salinity-dependent freezing temperature, sea-ice also melts from below; this meltwater is carried northward by the surface ocean flow (bottom panels); the flow is northward because at other longitudes the polar easterlies drive southward flow, and the sea-ice shields the water beneath it from the wind-stress allowing it freely move north, pushed by horizontal convergence.

Going to stronger (westerly *and* easterly) wind-stress, the northward ocean surface and sea-ice flow near the western boundary speeds up (lower right panel). This spreads the melting sea-ice and meltwater out over a larger latitude range, resulting in no discernible corresponding buoyancy anomaly in the zonal average (Figure 5.9).

Under restoring SBC's, on the other hand, the lack of sea-ice means polar easterlies simply drive southward Ekman transport at all longitudes (Figure 5.12, lower panels) and deep water is formed all along the southern boundary. The positive buoyancy anomaly seen in the upper panels exists because the restoring temperature and salinity fields were taken from the EMBM & sea-ice model, but it does not change with changing winds.

Note that the behaviour of sea-ice described above depends on the presence of the land boundary. We included it to mimic the geometry of the Antarctic Peninsula and the Weddell Sea. Previous sensitivity studies [Ito and Marshall, 2008; Nikurashin and Vallis, 2011] had the circumpolar channel extend to the southern boundary. Clearly, in addition to altering the sea-ice effects just discussed, this could alter the wind-driven dynamics considerably.

To summarize, increasing Southern Ocean wind-stress with the EMBM and sea-ice present, the stratification N^2 and hence the energy consumed by diapycnal mixing ϵ_{mix} increases more strongly than under restoring SBC's. On the other hand, the horizontal buoyancy contrast Δb_{z_d} that the MOC must overcome increases with wind-stress more under restoring SBC's than under the EMBM with sea-ice. As we have noted in (3.24), N^2 and Δb_{z_d} are intimately related, but the surface boundary conditions examined here conspire to nudge them in opposite directions (illuminating the "chicken-and-egg" problem referred to in Section 3.3). The result, predicted by (3.23) and verified in Figure 5.6, is that the response of the abyssal MOC to stronger Southern Ocean winds is to weaken under restoring SBC's, but to strengthen under the EMBM with sea-ice present.

This feedback should be kept in mind when presenting simple analytical solutions. For example, in their analytical solution, Nikurashin and Vallis [2011] prescribe the surface buoyancy b_0 as a quadratic function of latitude y, so that $\partial_{yy} b_0$ is a constant. They then project this along isopycnals onto the vertical structure of buoyancy in the deep ocean interior: hence $\partial_{zz}\bar{b}$ is also constant. In that case, and with a constant κ_ν, variations in the strength of the MOC are entirely controlled by changes in the stratification, as can be seen from the advective-diffusive balance, (3.7). In reality, $\partial_{zz}\bar{b}$ will change as well (and therefore we prefer thinking in terms of the box model of

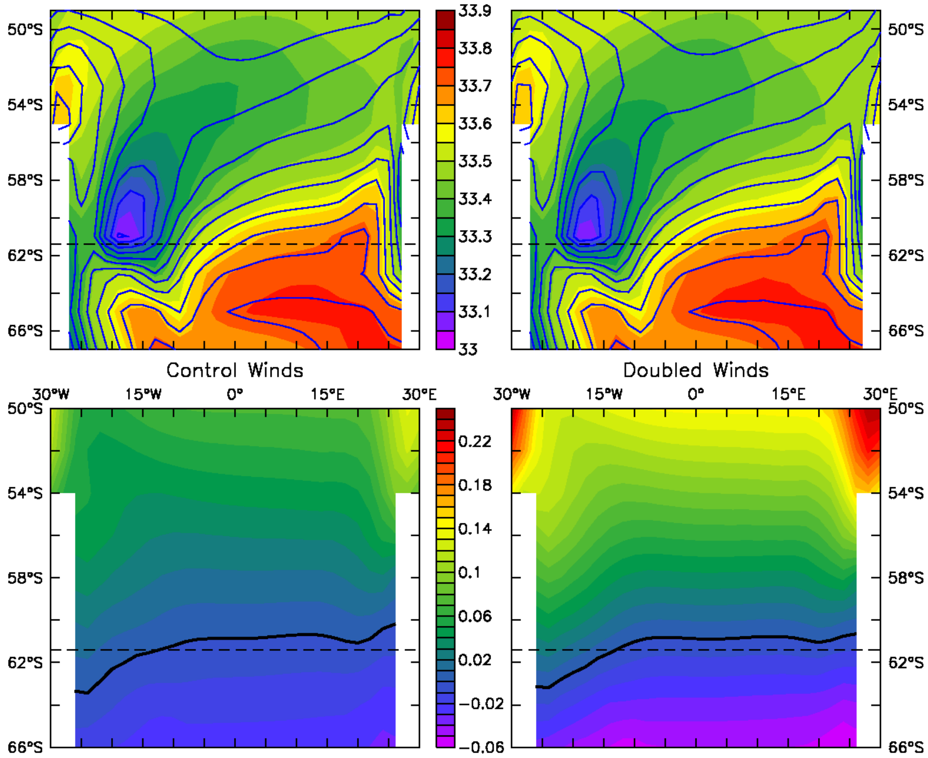

Figure 5.12: Relating the surface velocity and salinity distribution in the Southern Ocean, in the "Bryan-Lewis" model with restoring SBC's (no sea-ice) and a variable K_{GM} scheme. Figure layout is as in Figure 5.11.

Section 3.3 for the energetic intuition it affords and because it exchanges the $\partial_z \bar{b}$ and $\partial_{zz} \bar{b}$ terms for the simpler pair, N^2 and Δb_{z_d}). Indeed, allowing for feedbacks between the large-scale ocean circulation, eddies, and climate can strongly affect the response of the interior stratification *and* its curvature ($\partial_{zz} \bar{b}$) to changes in the Southern Ocean wind-stress. As we have shown, these feedbacks tend to strengthen the abyssal MOC with winds.

5.2 Perturbing winds globally

We now consider the "GFD" experiments in which wind-stress is modified globally by a multiplicative factor. In this case, the total wind energy input to the model ocean ($\sim$ 0.32 TW at control winds) changes more drastically with τ than in the "SOW" experiments, reaching $\sim$ 1.1 TW for doubled global wind-stress in the "GFD" experiments, compared to $\sim$ 0.47 TW for doubled wind-stress over the Southern

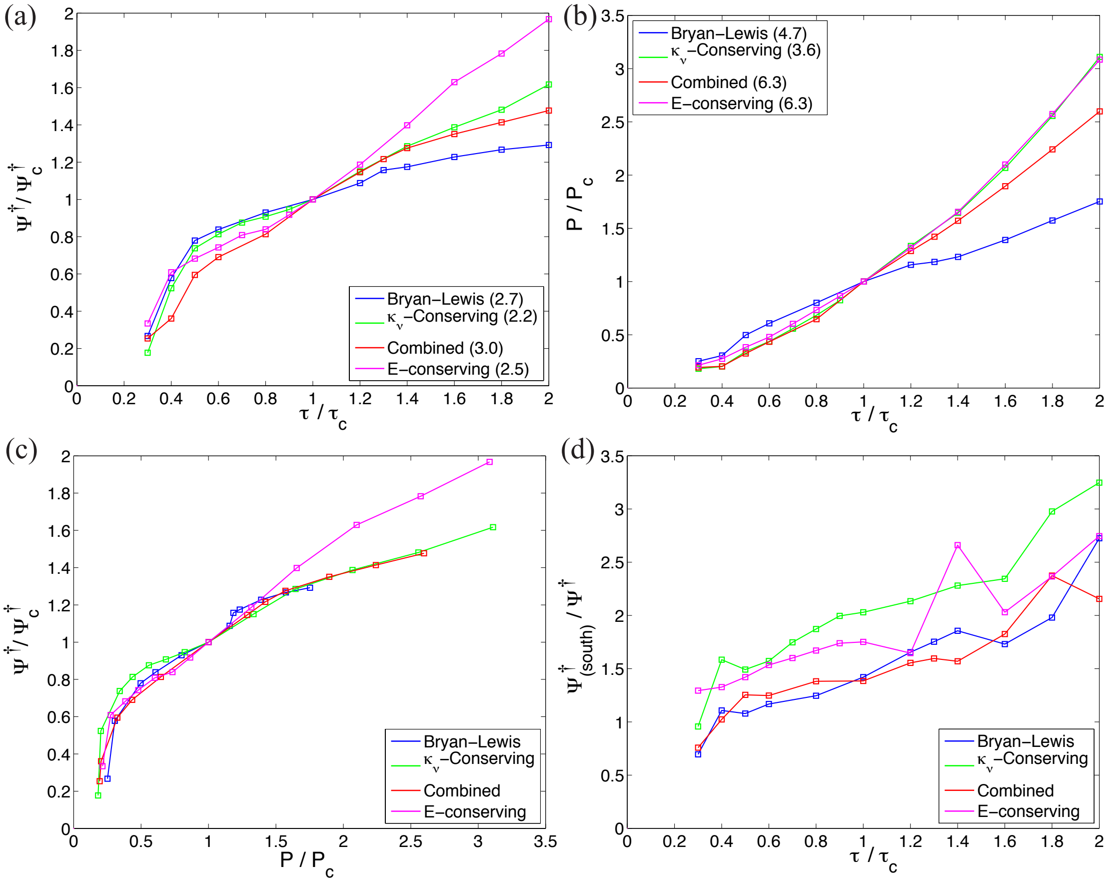

Figure 5.13: Results from the "GFD" experiments. (a) Relative strength of the abyssal MOC, $\Psi^\dagger$, north of the circumpolar channel. Numbers in parentheses indicate $\Psi^\dagger_c$ [Sv], the value of $\Psi^\dagger$ at control winds $\tau_c = 0.2$ Pa. (b) Relative potential energy generated by diapycnal mixing, P, from (5.1). Numbers in parentheses indicate P_c [GW], the value of P at $\tau = \tau_c$. (c) Relative $\Psi^\dagger$ vs. relative P. (d) Ratio of recirculation in the Southern Ocean to the basin-scale abyssal MOC, as in Figure 5.5.

Ocean in the "SOW" experiments.

Correspondingly, in the models where eddy energy dissipation (and hence wind energy input, indirectly) support diapycnal mixing, the potential energy generated by diapycnal mixing in the deep ocean basin, P, is more sensitive to changes in the wind-stress (Figure 5.13b) than in the "SOW" experiments, because κ_ν, in addition to N^2, changes significantly with τ. However, the "Bryan-Lewis" experiment — with unvarying κ_ν and hence $P \propto N^2$ only — shows a relatively consistent sensitivity of P to τ between the "SOW" and "GFD" experiments (Figures 5.13b and 5.3a): indeed, at realistic levels of diapycnal mixing, deep stratification is set primarily by the Southern Ocean isopycnal slope and surface climate, themselves primarily influenced by the Southern Ocean, rather than the global, wind-stress [Wolfe and Cessi, 2010; Nikurashin and Vallis, 2011]. Nevertheless, second order effects are noticeable: at doubled τ, P reaches 8.3 GW in the "GFD" case compared to 7.1 GW in the "SOW" case. The winds over the ocean basin influence the deep stratification in two competing ways: (a) by increasing Ekman downwelling in the sub-tropics, deepening the thermocline and reducing the geometrical extent of deep waters so as to increase the deep stratification, and (b) increasing the density of NADW and hence reducing the density contrast between NADW and AABW, reducing the deep stratification. Evidently, for "Bryan-Lewis" levels of diapycnal mixing, the former mechanism is more significant.

As in the "SOW" experiments, the "E-conserving" model shows a stronger increase of the basin-scale abyssal MOC $|\Psi^{\dagger}|$ with τ and/or P (Figures 5.13a,c) than do the "κ_{ν}-conserving" or "Combined" models. Again, short-circuiting of the abyssal MOC is the likely cause, at least for the "κ_{ν}-conserving" model (Figure 5.13d). However, this effect is less pronounced (c.f. Figure 5.5) than in the "SOW" experiments especially for the models in which eddy energy supports mixing in the local water column, owing to a globally perturbed wind-stress creating larger κ_{ν} in the ocean basin, which encourages a basin-scale overturning.

Decreasing the global wind-stress, all models show a strong and fairly linear decline of P (Figure 5.13b), including the "E-conserving" model which in the "SOW" experiments had P maintained at low τ by the unperturbed winds over the basin. In agreement with (3.23), as P decreases so does $|\Psi^{\dagger}|$, and indeed even the "E-conserving" run shows a collapse of $\Psi^{\dagger}$ at low wind-stress in the "GFD" experiments (Figure 5.13a).

Chapter 6

Conclusions

To maintain the small-scale turbulence and observed stratification in the deep ocean against a steady intrusion of cold, salty Antarctic Bottom Water, it is believed that some 3 ± 1 TW of mechanical energy input are required [Munk and Wunsch, 1998; St. Laurent and Simmons, 2006]. A fraction of this energy, but perhaps no more than 1 TW, comes from the dissipation of tides in the abyss. The most plausible candidate to account for the rest is the wind [e.g. Munk and Wunsch, 1998], and most of the wind energy input to the ocean's large-scale circulation is from the Southern Hemisphere westerly winds over the Southern Ocean [Wunsch, 1998]. In the unique dynamics of the Southern Ocean, the continual work of the wind steepens isopycnals, connecting the abyssal Pacific, Atlantic, and Indian Oceans with the mixed layer of the Southern Ocean, thereby maintaining the deep stratification [e.g. Wolfe and Cessi, 2010].

At the same time, this wind energy input is dissipated to a significant degree by mesoscale eddies consuming available potential energy. Recent theoretical, observational, and numerical work, collected and discussed by Marshall and Naveira Garabato [2008], suggests a large fraction of eddy energy dissipation is by way of barotropic eddies generating internal lee waves through interactions with rough bottom topography. These internal waves break, largely in the abyss, and small-scale turbulence and diapycnal mixing ensues. Being driven by diapycnal mixing, the basin-scale abyssal MOC should be sensitive to this energy pathway.

Previous theoretical scalings of the abyssal MOC, with a wind-independent diapycnal diffusivity, predict it to weaken under strengthening winds over the Southern Ocean. We extended one of these theories to include this energy pathway and found that the abyssal MOC actually intensifies as stronger Southern Ocean winds steepen isopycnals and eddies release more energy to diapycnal mixing in the abyss. Furthermore, we predicted that when there are two energy sources supporting mixing, one constant and the other wind-dependent, then there is a critical wind-stress at which the abyssal MOC attains a minimum strength, and below which it increases.

Following and expanding upon the suggestion of Marshall and Naveira Garabato [2008], we presented two distinct parameterizations of this energy pathway — from large-scale surface wind energy input to small-scale abyssal diapycnal mixing — for use in coarse-resolution ocean general circulation models employing the Gent and McWilliams [1990] closure for mesoscale eddies. Both our parameterizations measure the energy dissipated by GM-parameterized eddies and transfer a certain fraction of that energy to diapycnal mixing. One parameterization (termed "κ_ν-conserving") transfers the energy dissipated by eddies to diapycnal diffusion locally, then rearranges the diffusivity to be bottom-enhanced. The second parameterization globally redistributes a fraction of the energy dissipated by eddies, leaving the remaining fraction in the local water column; this energy distribution is bottom-enhanced, and then diapycnal diffusivities are calculated. The second parameterization ensures precisely the desired fraction of energy dissipated by eddies goes to support diapycnal mixing, and hence is called "E-conserving".

We studied the effect of these parameterizations, and simple variants on them, through numerical modelling. Our models employing some form of these parameterizations showed, in general, an increase of the abyssal MOC under strengthened winds over the Southern Ocean. This is in contrast to previous numerical results, as well as the aforementioned scaling theories, wherein the diapycnal diffusivity was independent of the wind-stress, in which case the abyssal MOC slows under strengthened Southern Ocean wind-stress.

However, our model included a parameterization for the eddy transfer coefficient that increases with the local baroclinicity, as well as sea-ice and a simple yet dynamic atmosphere. These features tend to support the abyssal MOC increasing under increased Southern Ocean wind-stress. Indeed, even with a wind-independent diapycnal diffusivity [after Bryan and Lewis, 1979], with these features active the abyssal MOC strengthens (albeit much more weakly than with a wind-dependent diapycnal diffusivity) under increased Southern Ocean wind-stress; in contrast, with these features disabled the abyssal MOC does indeed weaken under increased Southern Ocean wind-stress, in agreement with previous numerical and theoretical results that also employed a constant eddy transfer coefficient and restoring surface boundary conditions [Ito and Marshall, 2008; Nikurashin and Vallis, 2011]. This indicates the importance of feedbacks between the winds and the eddy activity and of feedbacks between the wind-driven changes in the ocean circulation and the surface climate, the latter tending to be suppressed when sea surface temperature and salinity are restored to prescribed fields.

Our prediction of an increase of the abyssal MOC below a critical wind-stress was found only in the "E-conserving" model. We argued that, in addition to having one wind-dependent and one fairly constant energy source for mixing, the two unique properties of this parameterization — that it conserves energy and that it redistributes some of that energy globally — are required if the abyssal MOC is to exhibit a minimum strength at some critical wind-stress.

We also generalized (Appendix C) the scaling theory of Ito and Marshall [2008], to explicitly account for the effect of the depth-dependent isopycnal slope in the Southern Ocean. This led to some qualitatively different predictions. In particular, the abyssal MOC is maintained above a constant strength under wind-independent diapycnal diffusivity even as the wind-stress is increased without bounds, and, with one wind-dependent and one wind-independent energy source for mixing, there is no critical wind-stress below which the abyssal MOC appreciably increases. Nonetheless, the key result, that the abyssal MOC strengthens under stronger winds when there is a wind-dependent energy source for abyssal diapycnal mixing, holds.

We thus conclude that, while on energetic grounds we prefer the "E-conserving" parameterization for wind-driven diapycnal mixing, and though it agrees well with one theoretical scaling of the abyssal MOC, more research is required to compare the merits and demerits of these mixing parameterizations. Nonetheless, it has been made clear, it is hoped, that incorporating an energy source for diapycnal mixing in the abyss that is ultimately wind-driven significantly alters the abyssal circulation in general, and the strength of the lower-limb of the ocean's meridional overturning circulation in particular.

Appendix A

Transformed Eulerian Mean

Primitive TEM

Here we follow [Vallis, 2006, Section 7.3.4], to derive the Transformed Eulerian Mean (TEM) buoyancy equation. Its advantage, we shall see, is that the eddy momentum flux and the eddy buoyancy flux are combined into a single term, the potential vorticity flux, in the TEM momentum equation, while the TEM buoyancy equation becomes devoid of explicit eddy terms. Thus the TEM framework acknowledges and employs the important dynamical link between the eddy momentum flux and the eddy buoyancy flux. The result is a transformed velocity field, the "residual velocity", that is the sum of the mean and eddy-induced velocities, and represents the total mass-weighted circulation.

Let $b = -g(\rho - \rho_0)\rho_0^{-1}$ be the buoyancy, where g is the gravitational acceleration, ρ the density, and ρ_0 a reference density. Consider the primitive buoyancy equation,

$$\partial_t b + \mathbf{u} \cdot \nabla b = S, \tag{A.1}$$

where $\mathbf{u}$ is the 3D velocity vector and the field S is a buoyancy source field. To each of the variables in (A.1) we shall apply a standard Reynolds decomposition, $\lambda = \bar{\lambda} + \lambda'$, where the over-bar represents a temporal and/or spatial average over scales larger than geostrophic eddies but smaller than climatic scales, and the prime indicates deviations from that average. Note $\mathbf{u}'$ is the eddy velocity. Then (A.1) becomes

$$\partial_t \bar{b} + \overline{\mathbf{u}} \cdot \nabla \bar{b} = \overline{S} - \nabla \cdot \left(\overline{\mathbf{u}'b'}\right). \tag{A.2}$$

The eddy buoyancy flux, $\overline{\mathbf{u}'b'}$, is placed on the RHS because, to the extent that the eddying flow is not resolved, the LHS is the material derivative for the resolved buoyancy and the eddy buoyancy flux modifies the large-scale buoyancy distribution just as a source / sink would. The eddy buoyancy flux can be decomposed into along-isopycnal and across-isopycnal (diapycnal) fluxes:

$$\overline{\mathbf{u}'b'} = \overline{\mathbf{u}'b'}_{||} + \overline{\mathbf{u}'b'}_{\perp}. \tag{A.3}$$

Let $\mathbf{u}^*$ represent an as yet unspecified eddy-induced velocity. Like the mean velocity, we wish it to be an incompressible flow, and hence by the Helmholtz decomposition we may write $\mathbf{u}^* = \nabla \times \boldsymbol{\psi}$, where $\boldsymbol{\psi}$ is an arbitrary vector stream function. Define the residual velocity as:

$$\mathbf{u}^\dagger \equiv \overline{\mathbf{u}} + \mathbf{u}^*. \tag{A.4}$$

Employing the fact that $\mathbf{u}^*$ is divergence-free, we add $\mathbf{u}^* \cdot \nabla\bar{b}$ to the LHS of (A.2) and $\nabla \cdot \left(\mathbf{u}^*\bar{b}\right)$ to the RHS. Then, using (A.4), we get

$$\partial_t\bar{b} + \mathbf{u}^\dagger \cdot \nabla\bar{b} = \overline{S} - \nabla \cdot \left(\overline{\mathbf{u}'b'}\right) + \nabla \cdot \left(\mathbf{u}^*\bar{b}\right). \tag{A.5}$$

We are now free to choose $\mathbf{u}^*$, or equivalently, to choose $\boldsymbol{\psi}$, so as to simplify (A.5). Since it is often easier to parameterize diapycnal fluxes than along-isopycnal fluxes, we shall choose $\mathbf{u}^*$ such that the RHS of (A.5) contains only diapycnal fluxes (aside from $\overline{S}$). That is, we shall choose $\mathbf{u}^*$ such that

$$\begin{aligned} \nabla \cdot \left(\mathbf{u}^*\bar{b}\right) &= \nabla \cdot \overline{\mathbf{u}'b'}_{||} \\ \nabla \cdot \left(\bar{b}\, \nabla \times \boldsymbol{\psi}\right) &= \\ \nabla \cdot \left(\boldsymbol{\psi} \times \nabla\bar{b}\right) &= \nabla \cdot \left(\frac{\nabla\bar{b} \times \overline{\mathbf{u}'b'}}{|\nabla\bar{b}|^2} \times \nabla\bar{b}\right). \end{aligned} \tag{A.6}$$

where the expression for $\overline{\mathbf{u}'b'}_{||}$ is obtained by noting that the unit vector normal to the isopycnal surface is $\nabla\bar{b}/|\nabla\bar{b}|$. It is clear from (A.6) that the simplest choice is

$$\psi = \frac{\nabla\bar{b} \times \overline{\mathbf{u}'b'}}{|\nabla\bar{b}|^2}. \tag{A.7}$$

Putting this in (A.5) and using (A.3) gives the TEM version of the buoyancy equation,

$$\partial_t\bar{b} + \mathbf{u}^\dagger \cdot \nabla\bar{b} = \overline{S} - \nabla \cdot \overline{\mathbf{u}'b'}_{\perp}. \tag{A.8}$$

In the interior of the ocean, eddies are, to very good approximation, adiabatic, meaning the diapycnal buoyancy flux $\overline{\mathbf{u}'b'}_{\perp}$ above is zero, and the TEM buoyancy equation takes on a particularly simple form, containing no explicit eddy terms. (Note the eddies have not been removed. The eddy terms are collected in the momentum equation, not shown here, and appear as a single term: the flux of potential vorticity or, equivalently, the divergence of the Eliassen-Palm flux.)

TEM for buoyancy under small-slope approximation

Thus far we have expressed one form of the TEM buoyancy equation and illustrated the purpose of the TEM framework. However, other transformations are possible and the one that follows gives a cleaner and more intuitive expression, first arrived at by Gent *et al.* [1995], for the eddy-induced velocity $\mathbf{u}^*$, though at the expense of some eddy terms remaining in the transformed buoyancy equation. In this case, we instead decompose the eddy buoyancy flux into along-isopycnal and *vertical* components; since the isopycnal slope is generally small, this is only slightly different from the transformation applied above, and the eddy terms that remain in the transformed buoyancy equation will be small, perhaps negligible. Proceeding, we write

$$\overline{\mathbf{u}'b'} = \overline{\mathbf{u}'b'}_{||} + \overline{\mathbf{u}'b'}_{(z)}, \tag{A.9}$$

where

$$\begin{aligned}\overline{\mathbf{u}'b'}_{||} &= (\overline{u'b'},\, \overline{v'b'},\, \overline{u'b'}s_x + \overline{v'b'}s_y),\\ \overline{\mathbf{u}'b'}_{(z)} &= (0 \quad, 0 \quad, \overline{w'b'} - \overline{u'b'}s_x - \overline{v'b'}s_y),\end{aligned}$$

and the isopycnal slope is

$$\mathbf{s} = (s_x, s_y) = \left(-\frac{\partial_x \bar{b}}{\partial_z \bar{b}}, -\frac{\partial_y \bar{b}}{\partial_z \bar{b}}\right). \tag{A.10}$$

Note $\overline{\mathbf{u}'b'}_{||} \cdot \nabla \bar{b} = 0$ as intended. We can immediately compute

$$\nabla \cdot \overline{\mathbf{u}'b'}_{(z)} = \partial_z G \tag{A.11}$$

where

$$G = \left(\overline{w'b'} + \frac{\overline{u'b'}\partial_x \bar{b} + \overline{v'b'}\partial_y \bar{b}}{\partial_z \bar{b}}\right). \tag{A.12}$$

Furthermore, some algebra reveals that, once again, the along-isopycnal buoyancy flux can be written as an advective flux, i.e. $\nabla \cdot \overline{\mathbf{u}'b'}_{||} = \mathbf{u}^* \cdot \nabla \bar{b}$, but now with a somewhat different eddy-induced velocity $\mathbf{u}^* = (u^*, v^*, w^*)$. The result is

$$u^* = -\partial_z \Psi^*_{(x)}, \quad v^* = -\partial_z \Psi^*_{(y)}, \quad w^* = \partial_x \Psi^*_{(x)} + \partial_y \Psi^*_{(y)}, \tag{A.13}$$

from which we see non-divergence is retained, $\nabla \cdot \mathbf{u}^* = 0$, and where

$$\Psi^*_{(x)} = \frac{\overline{u'b'}}{\partial_z \bar{b}}, \quad \Psi^*_{(y)} = \frac{\overline{v'b'}}{\partial_z \bar{b}}, \tag{A.14}$$

Absorbing $\overline{\mathbf{u}'b'}_{||}$ into the advective flux by (A.4), this version of the TEM buoyancy equation becomes

$$\partial_t \bar{b} + \mathbf{u}^\dagger \cdot \nabla \bar{b} = \overline{S} - \partial_z G. \tag{A.15}$$

Assuming a small isopycnal slope, $\overline{\mathbf{u}'b'}_{(z)} \approx \overline{\mathbf{u}'b'}_{\perp}$ and so the assumption of adiabatic eddies that gave us $\overline{\mathbf{u}'b'}_{\perp} = 0$ in the last section is often extended to give $G = 0$. Finally, we note that with the eddy closure of [Gent and McWilliams, 1990],

$$\overline{u'b'} = -K_{GM} \partial_x \bar{b}, \quad \overline{v'b'} = -K_{GM} \partial_y \bar{b}, \tag{A.16}$$

the eddy-induced velocities are

$$u^* = -\partial_z \left(K_{GM} s_x \right), \; v^* = -\partial_z \left(K_{GM} s_y \right), \; w^* = \partial_x \left(K_{GM} s_x \right) + \partial_y \left(K_{GM} s_y \right), \tag{A.17}$$

as arrived at by Gent *et al.* [1995].

Appendix B

Variable Eddy Diffusivity

The Gent and McWilliams [1990] eddy mixing scheme offers a choice for the eddy transfer coefficient, K_{GM}. The simplest choice is a constant. However, global altimetric observations and eddy-resolving ocean simulations suggest that the regions of enhanced eddy activity are typically associated with strong currents, such as in the western boundary regions and in the Southern Ocean. It has therefore been argued [Held and Larichev, 1996; Visbeck *et al.*, 1997; Bryan *et al.*, 1999; Henning and Vallis, 2005; Cessi, 2008] that a formulation for K_{GM} that allows it to vary in space and time may represent a better choice in coarse-resolution ocean-climate simulations, especially when the ocean density structure is expected to change in response to changes in surface climate.

One common approach is to assume that the eddy transfer coefficient is the product of a typical eddy velocity, U_e, and a typical eddy mixing length, L_m:

$$K_{GM} = U_e \; L_m. \tag{B.1}$$

As illustrated schematically in Figure 2.3 and discussed in the text, most eddy kinetic energy is supplied through baroclinic instability which then decays in spatial scale until a scale comparable to the first baroclinic Rossby radius, L_d. At this scale, the eddy kinetic energy is roughly equal to the eddy potential energy [Gill, 1982]:

$$\overline{u'^2} = \frac{\overline{b'^2}}{N^2} \tag{B.2}$$

where primes indicate deviations from the mean field. This equipartition is often employed to estimate U_e [Held and Larichev, 1996; Henning and Vallis, 2005]. For example, assuming $|b'| \sim |\nabla \bar{b}| L_d$, it gives

$$U_e = \sqrt{\overline{u'^2}} \sim \frac{|\nabla \bar{b}|}{\sqrt{\bar{b}_z}} \, L_d, \tag{B.3}$$

where $|\nabla \bar{b}|/\sqrt{\bar{b}_z}$ is the Eady growth rate of baroclinic instability.

We employ the WKB method [e.g. Chelton *et al.*, 1998] to estimate

$$L_d = \frac{1}{\pi |f|} \int_{-H}^{0} \sqrt{\bar{b}_z} \, \mathrm{d}z. \tag{B.4}$$

Inserting (B.4) and the vertical average of (B.3) into (B.1) gives our expression for the eddy transfer coefficient

$$K_{GM} = c \frac{L_m}{\pi |f|} \left(\int_{-H}^{0} \sqrt{\bar{b}_z} \, \mathrm{d}z \right) \left(\frac{1}{H} \int_{-H}^{0} \frac{|\nabla \bar{b}|}{\sqrt{\bar{b}_z}} \, \mathrm{d}z \right), \tag{B.5}$$

where we have added the non-dimensional constant c.

Finally, we must choose L_m. One choice is to use $L_m = L_d$, in which case we arrive at the Visbeck *et al.* [1997] formulation. However, this gives $K_{GM} \propto |f|^{-2}$, leading to very large values of K_{GM} near the equator [Bryan *et al.*, 1999]. Taking this into consideration, and motivated in part by the results of Schlosser and Eden [2007] and Scott and Wang [2005], we set L_m to a constant. In the model, $L_m = 50$ km, $c = 1$, L_d is capped at 200 km within 5° of the equator, and we restrict $300 \text{ m}^2 \text{ s}^{-1} \leq K_{GM} \leq 3000 \text{ m}^2 \text{ s}^{-1}$. We note that if, in addition to L_m, we would choose to set $\bar{b}_z$ to a constant, then we would arrive at the formulation for K_{GM} which is implemented in a recent version of the GFDL MOM [Gnanadesikan *et al.*, 2006].

Appendix C

Alternative Scaling Theory

C.1 Motivation

Bottom-enhanced diapycnal mixing

Examining the theory of Ito and Marshall [2008], reviewed in Section 3.2, the isopycnal slope s did vary with depth, as can be seen, for example, in (3.12) and noting that $\overline{\Psi}$ varies linearly with depth below the highest topography. This depth-dependent s immediately raises a problem with our extensions of the theory of Ito and Marshall [2008] to use alternative parameterizations of κ_ν which depended upon s: we did not account for the $\partial_z \kappa_\nu$ term, which must be non-zero since s does vary with depth. A simple attempt to include the $\partial_z \kappa_\nu$ term produces undesirable results, as is now shown.

Suppose that we wanted to incorporate a bottom-enhancement of κ_ν by a vertical structure function $F(z)$ as in (2.10). Also suppose diapycnal mixing is supported entirely by eddy energy dissipation; that is, let κ_ν be given by (2.11). As we are now explicitly changing the depth-dependence of κ_ν, we should not ignore the term $\partial_z \kappa_\nu = -\zeta^{-1} \kappa_\nu$ in this case. Then, with $s = \alpha z_0 / \tilde{y}$ as in Section 3.2, (3.10) becomes[1]

$$\Psi^\dagger = \alpha \Gamma K_{GM} s H F(z) \left(1 - \frac{z_0}{\zeta}\right). \tag{C.1}$$

---

[1] We've ignored the fact that the integral in (2.11) does not include the mixed layer — a minor difference.

Together with (3.3), we can solve for the abyssal MOC,

$$\Psi^\dagger = -\overline{\Psi}\frac{\gamma'}{1-\gamma'}, \tag{C.2}$$

where $\gamma' = \alpha\Gamma\left(1-\frac{z_0}{\zeta}\right)HF(z)$. Note if $\zeta < z_0$ (a strong bottom-enhancement of diapycnal mixing), then $\Psi^\dagger$ becomes positive, which is problematic for our theory. Note that, in this theory, bottom-intensification of mixing (i.e. $\partial_z\kappa_\nu < 0$) weakens the abyssal MOC, $|\Psi^\dagger|$, or in the extreme case of $\zeta < z_0$, actually reverses the sign of $\Psi^\dagger$. This counter-intuitive result is owing to the fact that the bottom boundary is not well accounted for: The condition of zero diapycnal flux across the bottom boundary requires (as we shall see) a strongly varying κ_ν near the bottom boundary, and hence a large $\partial_z\kappa_\nu > 0$ that offsets the effect of $\partial_z\kappa_\nu$ on $\Psi^\dagger$ above the bottom boundary. This is a limitation of the theory presented in Section 3.2, which in this Appendix we attempt to address.

Consideration of α

Another difficulty with the theory of Section 3.2 lies in the estimation of the parameter α. Calculating the distance $\tilde{y}$ (or the meridional distance y) travelled while moving up from $-H$ to z along an isopycnal was necessary to simplify (3.10), and can be done exactly if we know s as a function of height above the bottom, $z+H$. If s were constant with depth, for example, then $y = (z+H)/s$ exactly. However, if one wants a local theory or if one only knows (the depth-varying) s at one particular depth, then a parameter $\hat{\alpha}$ can substitute for the missing knowledge: $y = \hat{\alpha}(z+H)/s$. Since $|s|$ tends to increase moving upwards from the sea-floor, $\hat{\alpha} > 1$. Furthermore, recalling (3.10), it was necessary to relate s, $\tilde{y}$, and z_0 rather than s, y, and z; note that z_0 is by no means related to the chosen depth z of evaluation of $\Psi^\dagger$. Thus we used, following Ito and Marshall [2008], a new parameter α such that $\tilde{y} = \alpha z_0/s$.

Determining, from theory, the proper value of α is non-trivial; indeed, Ito and Marshall [2008] fit α from their numerical models. One approach would be to exploit the dominant balance in (3.3) and (3.10), which is $\overline{\Psi} + K_{GM}s = 0$, such that s grows approximately linearly with height above the bottom. Making this assumption, we can calculate[2]

$$\alpha = \frac{\tilde{y}s}{z_0} = \frac{1}{z_0}\frac{K_{GM}}{\partial_z\overline{\Psi}}\ln\left|1 - \frac{\partial_z\overline{\Psi}}{K_{GM}}\frac{z_0}{s_b}(z+H)\right|\left(-s_b + \frac{\partial_z\overline{\Psi}}{K_{GM}}(z+H)\right), \tag{C.3}$$

where $s_b < 0$ is the slope just above the sea-floor. Taking $(z+H) = z_0 = 10^3$ m, $K_{GM} = 10^3$ m^2 s^{-1}, $\partial_z\overline{\Psi} = 10^{-3}$ m s^{-1}, and $s_b = 3 \times 10^{-4}$, this α increases fairly linearly and strongly from the ocean bottom, reaching ~ 2 at 1000 m above the bottom.

However, the subtle variations of s from $-\overline{\Psi}/K_{GM}$ are what gives a non-zero $\Psi^\dagger$, so this remains unsatisfactory for two reasons. First, adopting this strongly depth-dependent α changes the solution for s, which feeds back to change α, and so on. This can be easily seen at the sea-floor, where

$$s_b = \lim_{z\to -H} s(z) = -\sqrt{\alpha\frac{\kappa_\nu}{K_{GM}}} \tag{C.4}$$

from (3.12). Thus, s_b depends on α, but α depends on s_b. Second, (especially with slope-dependent parameterizations of κ_ν) $\Psi^\dagger$ varies with depth, further confounding the use of $-\overline{\Psi}/K_{GM}$ to approximate s.

In this section we shall resolve these problems by evaluating (3.10) without using the approximation inherent in α. Rather, we explicitly allow the isopycnal slope to vary with depth, solving for s and $\Psi^\dagger$ at all depths simultaneously. The results, we shall see, for s and $\Psi^\dagger$ are qualitatively different from those in the Section 3.2: even a "perfectly-fit" α will not reconcile these differences. The trade-off is that we must work with ordinary differential equations (ODE's), which must sometimes be solved numerically.

C.2 Derivation

For an infinitesimal change in depth dz, the corresponding infinitesimal distance travelled along-isopycnal is

$$\mathrm{d}\tilde{y} = \frac{\sqrt{1+s^2}}{s}\mathrm{d}z \approx \frac{1}{s}\mathrm{d}z, \tag{C.5}$$

---

[2] To obtain this, take $s(z) = s_b - \frac{\partial_z\overline{\Psi}}{K_{GM}}(z+H) = \mathrm{d}z/\mathrm{d}y$, then integrate s^{-1} with respect to z to get the meridional distance $y < 0$ travelled while following an isopycnal upwards to depth $z + H$. For $s \ll 1$ the (signed) meridional distance is very close to the actual (signed) distance, $y \approx \tilde{y}$.

where the approximation assumes a small isopycnal slope, $s \ll 1$. For a continuous function f that is constant in latitude y, integration by substitution gives

$$\int_0^{\tilde{y}} f(\tilde{y}')\,\mathrm{d}\tilde{y}' = \int_{-H}^{z} f(z')\frac{\mathrm{d}\tilde{y}'}{\mathrm{d}z'}\mathrm{d}z' \approx \int_{-H}^{z} f(z')\frac{1}{s(z')}\mathrm{d}z', \tag{C.6}$$

where z is the depth of $\bar{b}$ at a distance $\tilde{y}$ from where $\bar{b}$ grounds. Applying this to (3.10), and collecting our two equations for the two variables $\Psi^\dagger$ and s here for convenience, we have

$$\Psi^\dagger = \overline{\Psi} + K_{GM}s \tag{C.7}$$

$$\Psi^\dagger = \int_{-H}^{z} \frac{1}{s}\left(\frac{\kappa_\nu}{z_0} + \frac{\partial \kappa_\nu}{\partial z'}\right)\mathrm{d}z'. \tag{C.8}$$

The assumption of meridional independence was applied, above, to κ_ν (and $\partial_z \kappa_\nu$ and z_0, but not to K_{GM} or s) over the region below where $\Psi^\dagger$ is to be evaluated, about 3 km depth, and from the circumpolar channel, $\sim 50°\mathrm{S}$, north to where that isopycnal through $(50°\mathrm{S}, 3\ \mathrm{km})$ grounds. Though there is certainly meridional variation of κ_ν in this region (Figure 4.5), this assumption is necessary to strike a balance for analytical tractability, and it pins the focus on understanding the effect of the vertical variation of κ_ν.

C.3 Application

In this section we develop the governing ODE's from the system (C.7) and (C.8) for three parameterizations of κ_ν. Some results are shown for realistic parameter choices in Figures C.1 and C.2.

C.3.1 Constant mixing

Let us now apply this theory to the case when κ_ν is constant, for comparison with Section 3.2.1. Taking the vertical derivative of (C.7) and (C.8), we get a non-linear differential equation for s:

$$s\frac{\mathrm{d}s}{\mathrm{d}z} + \frac{\partial_z \overline{\Psi}}{K_{GM}}\, s = \frac{\kappa_\nu}{z_0 K_{GM}}. \tag{C.9}$$

Analytic solutions do not come easily, so numerical solutions are used in this section. Nonetheless, the solution for s is then substituted into (C.7) to obtain $\Psi^\dagger$.

To solve (C.9), a bottom boundary condition for s must first be decided upon. There are two physical conditions at the bottom boundary that must be accounted for. First, the buoyancy flux across the ocean floor at $z = -H$ must be zero:

$$\kappa_\nu \frac{\partial b}{\partial z} = 0. \tag{C.10}$$

Since we have already established our buoyancy profile in (3.9), this can only be satisfied if $\kappa_\nu = 0$ at $z = -H$. Second, the eddy fluxes and hence the eddy-induced transport across the sea floor must be zero. In the GM eddy parameterization, this is usually realized by choosing $K_{GM} = 0$ at $z = -H$ [e.g. Gent *et al.*, 1995]. We thus consider a boundary layer $-H < z < -H + \eta$ for the above ODE (C.9), in which

$$\kappa_\nu = \left(\frac{z+H}{\eta}\right)\kappa_0, \tag{C.11}$$

$$K_{GM} = \left(\frac{z+H}{\eta}\right)K_0, \tag{C.12}$$

where κ_0 and K_0 are the values of κ_ν and K_{GM} in the ocean interior, respectively. Using these depth-varying parameters in (C.7) and (C.8) gives a different ODE for s:

$$\partial_z\overline{\Psi} + \frac{K_0}{\eta}s + \frac{K_0(z+H)}{\eta}\frac{\mathrm{d}s}{\mathrm{d}z} = \frac{1}{s}\frac{\kappa_0}{\eta}\left(\frac{z+H}{z_0} + 1\right). \tag{C.13}$$

For $\eta \ll 1$, the first term on the RHS and the first term on the LHS (remembering $z < -H + \eta$) can be neglected, giving

$$K_0(z+H)\frac{\mathrm{d}s}{\mathrm{d}z} + K_0 s = \frac{1}{s}\kappa_0. \tag{C.14}$$

This non-linear differential equation for s could, in theory, be solved to obtain $s(-H+\eta)$; however, this would require a bottom boundary condition: that is, a value for $s(-H)$, which is what we are searching for. Instead, we shall match the solutions for s in the bottom boundary region and the ocean interior. Specifically, equating $\frac{\mathrm{d}s}{\mathrm{d}z}$ from (C.9) and (C.14) at $z = -H + \eta$ gives

$$s^2 - \left(\frac{\partial_z\overline{\Psi}}{K_{GM}}\eta\right)s + \frac{\kappa_\nu}{K_{GM}}\left(\frac{\eta}{z_0} - 1\right) = 0. \tag{C.15}$$

Taking $\eta \to 0$ and choosing the negative root appropriate for the abyssal MOC gives

$$s_b = \lim_{\eta \to 0} s(-H + \eta) = -\sqrt{\frac{\kappa_\nu}{K_{GM}}}. \tag{C.16}$$

This is the bottom boundary condition for s to be used when solving (C.9) in the ocean interior. Physically, strong diapycnal (vertical) diffusion tends to increase the sea-floor isopycnal slope, while eddy motions tend to relax the slope. This is rather similar to the isopycnal slope near the sea-floor in the theory of Ito and Marshall [2008], given in (C.4). It is possible for other approaches[3] to be taken to determine an appropriate boundary condition $s(-H)$.

This non-zero bottom boundary condition embodies the point of including the $\partial_z \kappa_\nu$ term in (C.8). Indeed, following the above procedure but ignoring the $\partial_z \kappa_\nu$ term, one would obtain $s_b = 0$. Without considering this transitional layer where κ_ν may change rapidly, a bottom-intensified κ_ν tends to make $\Psi^\dagger$ *positive* by way of $\partial_z \kappa_\nu > 0$; this was the problem encountered in Section C.1. A strong bottom-enhancement of κ_ν with $\partial_z \kappa_\nu < 0$ in the interior must be balanced by $\partial_z \kappa_\nu > 0$ in the bottom layer, which gives intense diapycnal mixing and strong (equatorwards) circulation, tending to make $\Psi^\dagger$ negative. Using this non-zero boundary condition for s_b gives a rather different, and stronger, $\Psi^\dagger$, relative to using the boundary condition $s_b = 0$ (solid lines versus dotted lines in Figures C.1 and C.2).

In the limit of high wind-stress, the $\partial_z \overline{\Psi}$ term dominates in the ODE (C.9), giving

$$\frac{\mathrm{d}s}{\mathrm{d}z} + \frac{\partial_z \overline{\Psi}}{K_{GM}} = 0. \tag{C.17}$$

When integrated vertically and upon using (C.7), this gives

$$\lim_{\overline{\Psi} \to \infty} \Psi^\dagger = K_{GM}\ s(-H). \tag{C.18}$$

With the non-zero boundary condition $s(-H) = s_b$ given by (C.16), $\Psi^\dagger$ under high winds is maintained at a finite value: indeed, putting (C.16) into (C.18) gives

$$\lim_{\overline{\Psi} \to \infty} \Psi^\dagger = -\sqrt{\kappa_\nu K_{GM}}, \tag{C.19}$$

---

[3] One alternative approach we tried was to solve (C.7) and (C.8) with (C.11) but assuming constant K_{GM} and $s(-H) = 0$; we obtained $s(-H + \eta) = \sqrt{2\kappa_\nu / K_{GM}}$, which has the same form as (C.16).

which happens to be (up to α) the prediction for $\Psi^\dagger$ from the theory of Ito and Marshall [2008] in the limit of *low* wind-stress: see (3.14).

In the limit of low wind-stress, the $\partial_z\overline{\Psi}$ term can be neglected in the ODE (C.9). By solving the resulting linear ODE for s^2 and using (C.7), we get

$$\lim_{\overline{\Psi}\to 0} \Psi^\dagger = -\sqrt{\frac{2(z+H)}{z_0}+1}\cdot\sqrt{\kappa_\nu K_{GM}}. \tag{C.20}$$

When evaluated at $z=-H+z_0$, for example, we see from (C.19) and (C.20) that the variation in $\Psi^\dagger$ with wind-stress is up to $(\sqrt{3}-1)\sqrt{\kappa_\nu K_{GM}}$. This is less[4] than the corresponding variation of $\sqrt{\alpha\kappa_\nu K_{GM}}$ in the theory of Ito and Marshall [2008]: This alternative theory predicts, relative to the theory of Ito and Marshall [2008] with κ_ν constant in the ocean interior, a $\Psi^\dagger$ that is less sensitive to changes in wind-stress. This can be seen by comparing the solid and dotted blue lines in Figure C.2.

As we shall see, this weaker variation in $\Psi^\dagger$ with wind-stress has implications for whether $\Psi^\dagger$ shows an appreciable increase below a critical τ when two energy sources, one wind-dependent and one wind-independent, support mixing, as was found in Section 3.2.3.

C.3.2 Eddy mixing

When diapycnal mixing is supported entirely by eddies, $\kappa_\nu = \Gamma K_{GM} s^2$, (C.7) and (C.8) reduce to a first-order linear ODE that is analytically solvable. In this case the physical condition $\kappa_\nu = 0$ at $z=-H$ immediately gives the bottom boundary condition $s(-H)=0$. Equating (C.7) and (C.8) with this κ_ν and differentiating with respect to z, the ODE for s is

$$\frac{\mathrm{d}s}{\mathrm{d}z} - \frac{\Gamma}{z_0(1-2\Gamma)}s = \frac{-(\partial_z\overline{\Psi})}{K_{GM}(1-2\Gamma)}. \tag{C.21}$$

The analytical solution, valid below the height of topography in Drake Passage, $z < -H_T$, is:

$$s = \frac{-(\partial_z\overline{\Psi})z_0}{K_{GM}\Gamma}\left\{\exp\left(\frac{\Gamma}{z_0(1-2\Gamma)}(H+z)\right)-1\right\}. \tag{C.22}$$

---

[4] Choosing $\alpha = 1$, say. Also, this statement depends on the depth at which $\Psi^\dagger$ is evaluated, being particularly true when evaluating close to the sea-floor.

The residual stream function is then obtained from (C.7):

$$\Psi^\dagger = (\partial_z\overline{\Psi})(z+H) - \frac{(\partial_z\overline{\Psi})z_0}{\Gamma}\left\{\exp\left(\frac{\Gamma}{z_0(1-2\Gamma)}(H+z)\right) - 1\right\}. \tag{C.23}$$

As in Section 3.2.2 with the same $\kappa_\nu \sim s^2$, the overturning is predicted to increase linearly with increasing wind-stress (τ, embedded in $\partial_z\overline{\Psi}$). However, while that theory breaks down when $\alpha\Gamma$ is near or larger than 1 (see (3.15)), that fate is avoided here by explicit calculation and hence removal of α. Finally, note the above results are only valid below the level of highest topography, $z < -H_T$, but for $z \geq -H_T$ where $\partial_z\overline{\Psi} = 0$, (C.21) takes a simple exponential solution:

$$s(z \geq -H_T) = s_{H_T}\exp\left(\frac{\Gamma}{z_0(1-2\Gamma)}(z+H_T)\right) \tag{C.24}$$

$$\Psi^\dagger = \overline{\Psi} + K_{GM}s_{H_T}\exp\left(\frac{\Gamma}{z_0(1-2\Gamma)}(z+H_T)\right) \tag{C.25}$$

where $s_{H_T} = s(-H_T)$ may be calculated from (C.22).

C.3.3 Eddy + constant mixing

Lastly, consider the case where both eddy energy and a constant energy source support diapycnal mixing: $\kappa_\nu = \Gamma K_{GM}s^2 + \kappa_0$. Taking the vertical derivative of (C.7) and (C.8) gives our ODE for s:

$$K_{GM}(1-2\Gamma)s\frac{\mathrm{d}s}{\mathrm{d}z} - \frac{\Gamma K_{GM}}{z_0}s^2 + \left(\partial_z\overline{\Psi}\right)s = \frac{\kappa_0}{z_0}. \tag{C.26}$$

To determine the bottom boundary condition on s that ensures, as before, $\kappa_\nu = 0$ at the sea floor, let $s_b \equiv s(-H+\eta)$ be, for the moment, an unknown constant. Define κ_ν near the sea-floor ($-H < z < -H+\eta$) to linearly increase from zero until it matches the corresponding value at $z = -H+\eta$:

$$\kappa_\nu = \left(\Gamma K_{GM}s_b^2 + \kappa_0\right)\left(\frac{z+H}{\eta}\right). \tag{C.27}$$

As in Section C.3.1, (C.12) is retained for K_{GM}. In this bottom boundary region,

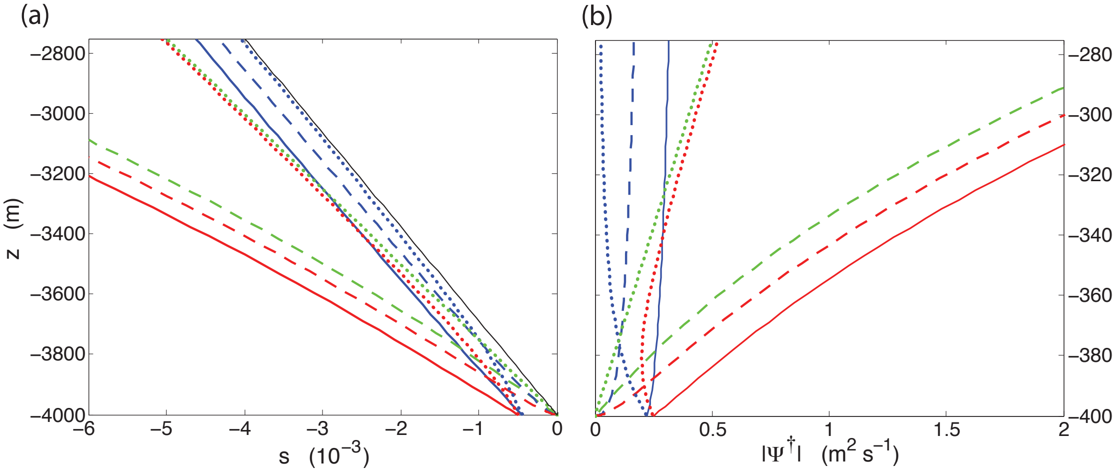

Figure C.1: Comparison of the (a) isopycnal slope (s) and (b) abyssal MOC ($|\Psi^\dagger|$) as a function of depth, for (colours) three different parameterizations of κ_ν and (line style) three different theories. Blue: $\kappa_\nu = 10^{-4}$ m^2 s^{-1} = constant; green: $\kappa_\nu = \Gamma K_{GM} s^2$; red: $\kappa_\nu = \Gamma K_{GM} s^2 + 10^{-4}$ m^2 s^{-1}. Dotted lines: Ito and Marshall [2008] theory, Section 3.2; dashed lines: alternate theory of Appendix C, with $s(-H) = 0$; solid lines: alternate theory of Appendix C, with $s(-H) = s_b$ incorporating $\kappa_\nu = 0$ and $K_{GM} = 0$ at $z = -H$. For reference, $-\overline{\Psi}/K_{GM}$ (which would give $\Psi^\dagger = 0$) is marked by the solid black line. The non-asymptotic behaviour of s and $\Psi^\dagger$ is emphasized by zooming in to smaller values. Other parameters are as in Figure 3.2.

(C.7) and (C.8) give a different ODE for s:

$$\partial_z \overline{\Psi} + \frac{K_0}{\eta} s + \frac{K_0(z+H)}{\eta}\frac{\mathrm{d}s}{\mathrm{d}z} = \frac{\Gamma K_0 s_b^2 + \kappa_0}{s\ \eta}\left(\frac{z+H}{z_0} + 1\right) \tag{C.28}$$

for which the first term on both sides can be neglected for $\eta \ll 1$. As in Section C.3.1, matching this $\frac{\mathrm{d}s}{\mathrm{d}z}$ in the bottom boundary layer with that in the ocean interior from (C.26) gives

$$s_b^2 = \frac{\Gamma K_{GM} s_b^2 + \kappa_0}{K_{GM}} \ \Rightarrow\ s_b = -\sqrt{\frac{\kappa_0}{K_{GM}(1-\Gamma)}}. \tag{C.29}$$

Again, this non-zero boundary condition for s, to be used in solving (C.26), reflects the importance of the depth variations of κ_ν, particularly the rapid changes near the sea-floor.

Note with this non-zero boundary condition s_b and realistic parameters, $\Psi^\dagger$ is monotonic: that is, there is no critical wind-stress at which $\Psi^\dagger$ attains a minimum. This is because, for the same parameters, the corresponding $\Psi^\dagger$ when $\kappa_\nu = \kappa_0$ shows little gain at low τ, as discussed at the end of Section C.3.1, or as seen in Figure C.2.

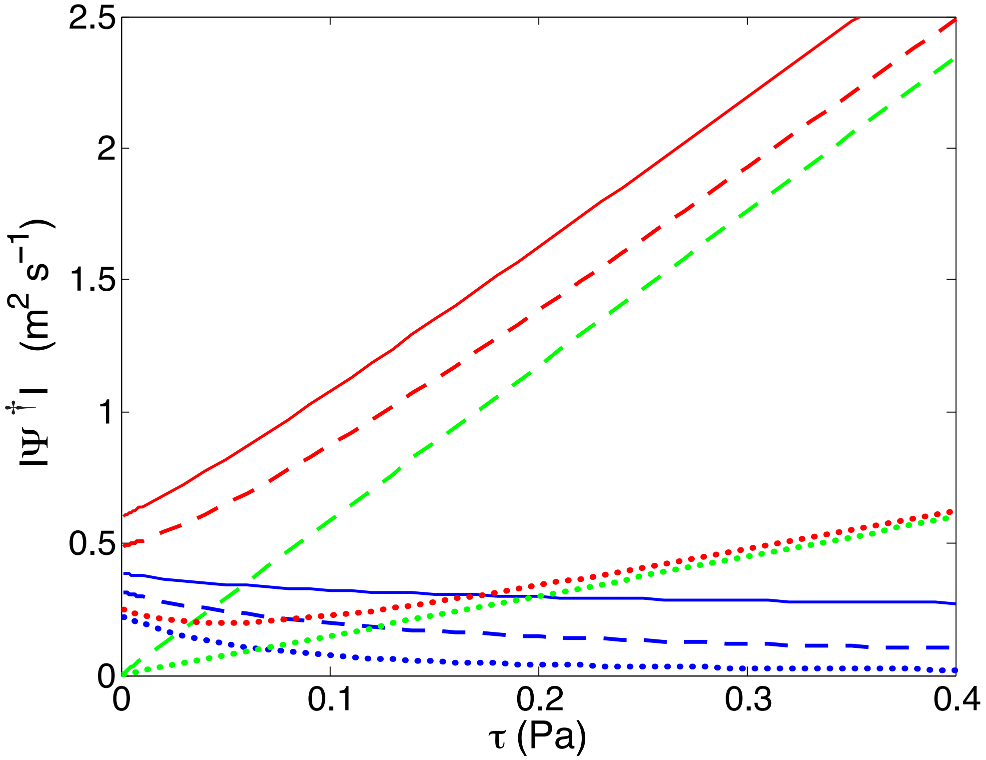

Figure C.2: Comparison of the abyssal MOC ($|\Psi^{\dagger}|$) as a function of Southern Ocean wind-stress (τ), for (colours) three different parameterizations of κ_{ν} and (line style) three different theories. Colours, line styles, and parameters are as in Figure C.1.

C.4 Summary

Here we have extended the theory of Ito and Marshall [2008] to a more general form embodied in (C.8), the theoretical benefits of which were discussed in Section C.1. Having two scaling theories, the question arises: to which scaling theory should we compare our numerical results?

We chose to compare the numerical results in Chapter 5 with the simpler scaling theory of Section 3.2, and indeed broad and interesting comparisons were made. The more complicated scaling theory developed here was not used for explicit comparison with the numerical model, but instead it serves by way of comparison to the simpler scaling theory. It reminds us that, as scaling theories, a wide range of results can be obtained depending on one's assumptions. Some results, such as the increase of the abyssal MOC under increased wind-stress when wind/eddy-energy supports diapycnal mixing in the abyss, are robust. However, other results, such as a possible critical wind-stress at which the abyssal MOC attains a minimum strength when there are both wind-dependent and wind-independent sources of mixing active, are evidently dependent on the details of the scaling theory.

Bibliography

Bryan, K. and L. J. Lewis (1979), A Water Mass Model of the World Ocean, *J. Geophys. Res.*, **84,** pp. 2503–2517, DOI: 10.1029/JC084iC05p02503 (see pp. 29, 59).

Bryan, K., J. K. Dukowicz, and R. D. Smith (1999), On the Mixing Coefficient in the Parameterization of Bolus Velocity, *Journal of Physical Oceanography*, **29,** pp. 2442–2456, DOI: 10.1175/1520-0485(1999)029<2442:OTMCIT>2.0.CO;2 (see pp. 65, 66).

Bryden, H. L. and A. J. G. Nurser (2003), Effects of strait mixing on ocean stratification, *Journal Of Physical Oceanography*, **33,** pp. 1870–1872, DOI: 10.1175/1520-0485(2003)033<1870:EOSMOO>2.0.CO;2 (see p. 22).

Cessi, P. (2008), An energy-constrained parameterization of eddy buoyancy flux, *Journal of Physical Oceanography*, **38,** pp. 1807–1819, DOI: 10.1175/2007JPO3812.1 (see p. 65).

Charney, J. G. (1971), Geostrophic Turbulence, *Journal Of The Atmospheric Sciences*, **28,** pp. 1087–1095, DOI: 10.1175/1520-0469(1971)028<1087:GT>2.0.CO;2 (see p. 7).

Chelton, D. B., R. A. DeSzoeke, M. G. Schlax, K. El Naggar, and N. Siwertz (1998), Geographical variability of the first baroclinic Rossby radius of deformation, *Journal of Physical Oceanography*, **28,** pp. 433–460, DOI: 10.1175/1520-0485(1998)028<0433:GVOTFB>2.0.CO;2 (see p. 66).

Dewar, W. K. and P. D. Killworth (1995), Do Fast Gravity-Waves Interact With Geostrophic Motions, *Deep-Sea Research Part I-Oceanographic Research Papers*, **42,** pp. 1063–1081, DOI: 10.1016/0967-0637(95)00040-D (see p. 8).

Döös, K. and D. J. Webb (1994), The Deacon Cell and the Other Meridional Cells of the Southern Ocean, *Journal of Physical Oceanography*, **24,** pp. 429–442, DOI: 10.1175/1520-0485(1994)024<0429:TDCATO>2.0.CO;2 (see p. 37).

Fanning, A. F. and A. J. Weaver (1996), An atmospheric energy-moisture balance model: Climatology, interpentadal climate change, and coupling to an ocean general circulation model, *Journal of Geophysical Research-Atmoshperes*, **101,** pp. 15111–15128, DOI: `10.1029/96JD01017` (see p. 26).

Farneti, R., T. L. Delworth, A. J. Rosati, S. M. Griffies, and F. R. Zeng (2010), The Role of Mesoscale Eddies in the Rectification of the Southern Ocean Response to Climate Change, *Journal Of Physical Oceanography*, **40,** pp. 1539–1557, DOI: `10.1175/2010JPO4353.1` (see p. 6).

Ferrari, R. and C. Wunsch (2009), Ocean Circulation Kinetic Energy: Reservoirs, Sources, and Sinks, *Annual Review of Fluid Mechanics*, **41,** pp. 253–282, DOI: `10.1146/annurev.fluid.40.111406.102139` (see pp. 5, 8).

Fyfe, J. C. and O. A. Saenko (2006), Simulated changes in the extratropical Southern Hemisphere winds and currents, *Geophysical Research Letters*, **33,** DOI: `10.1029/2005GL025332` (see p. 31).

Ganachaud, A. (2003), Large-scale mass transports, water mass formation, and diffusivities estimated from World Ocean Circulation Experiment (WOCE) hydrographic data, *Journal of Geophysical Research-Oceans*, **108,** p. 3213, DOI: `10.1029/2002JC001565` (see p. 34).

Ganachaud, A. and C. Wunsch (2000), Improved estimates of global ocean circulation, heat transport and mixing from hydrographic data, *Nature*, **408,** pp. 453–457, DOI: `10.1038/35044048` (see p. 34).

Gent, P. and J. McWilliams (1990), Isopycnal Mixing in Ocean Circulation Models, *J. Phys. Oceanogr.*, **20,** pp. 150–155, DOI: `10.1175/1520-0485(1990)020<0150:IMIOCM>2.0.CO;2` (see pp. 2, 9–12, 17, 27, 32, 33, 59, 64, 65, 71).

Gent, P., J. Willebrand, T. McDougall, and J. McWilliams (1995), Parameterizing Eddy-Induced Tracer Transports in Ocean Circulation Models, *Journal of Physical Oceanography*, **25,** pp. 463–474, DOI: `10.1175/1520-0485(1995)025<0463:PEITTI>2.0.CO;2` (see pp. 10, 11, 63, 64, 71).

Gerdes, R., C. Köberle, and J. Willebrand (1991), The influence of numerical advection schemes on the results of ocean general circulation models, *Climate Dynamics*, **5,** (4), pp. 211–226, DOI: `10.1007/BF00210006` (see p. 27).

Gill, A. E. (1973), Circulation and Bottom Water Production in Weddell Sea, *Deep-Sea Research*, **20,** pp. 111–140, DOI: `10.1016/0011-7471(73)90048-X` (see p. 53).

Gill, A. E. (1982), *Atmosphere: Ocean Dynamics*, Academic Press, p. 662 (see pp. 5, 40, 65).

Gille, S. T., M. M. Yale, and D. T. Sandwell (2000), Global correlation of mesoscale ocean variability with seafloor roughness from satellite altimetry, *Geophys. Res. Lett.*, **27,** pp. 1251–1254, DOI: `10.1029/1999GL007003` (see p. 8).

Gnanadesikan, A., K. W. Dixon, S. M. Griffies, V. Balaji, M. Barreiro, J. A. Beesley, W. F. Cooke, T. L. Delworth, R. Gerdes, M. J. Harrison, I. M. Held, W. J. Hurlin, H.-C. Lee, Z. Liang, G. Nong, R. C. Pacanowski, A. Rosati, J. Russell, B. L. Samuels, Q. Song, M. J. Spelman, R. J. Stouffer, C. O. Sweeney, G. Vecchi, M. Winton, A. T. Wittenberg, F. Zeng, R. Zhang, and J. P. Dunne (2006), GFDL's CM2 Global Coupled Climate Models. Part II: The Baseline Ocean Simulation, *Journal of Climate*, **19,** pp. 675–697, DOI: `10.1175/JCLI3630.1` (see p. 66).

Gregg, M. C. (1987), Diapycnal Mixing in the Thermocline - a Review, *Journal of Geophysical Research-Oceans*, **92,** pp. 5249–5286, DOI: `10.1029/JC092iC05p05249` (see p. 4).

Held, I. M. and V. D. Larichev (1996), A Scaling Theory for Horizontally Homogeneous, Baroclinically Unstable Flow on a Beta Plane, *Journal of the Atmospheric Sciences*, **53,** pp. 946–952, DOI: `10.1175/1520-0469(1996)053<0946:ASTFHH>2.0.CO;2` (see p. 65).

Henning, C. C. and G. K. Vallis (2005), The effects of mesoscale eddies on the stratification and transport of an ocean with a circumpolar channel, *Journal of Physical Oceanography*, **35,** pp. 880–896, DOI: `10.1175/JPO2727.1` (see p. 65).

Huang, R. X. and W. Wang (2003), "Gravitational potential energy sinks/sources in the oceans", in: *Near-Boundary Processes and Their Parameterization, Proceedings, Hawaii Winter Workshop*, Honolulu, HI, University of Hawaii at Manoa, pp. 239–247 (see pp. 6, 11).

Ito, T. and J. Marshall (2008), Control of Lower-Limb Overturning Circulation in the Southern Ocean by Diapycnal Mixing and Mesoscale Eddy Transfer, *Journal of Physical Oceanography*, **38,** pp. 2832–2845, DOI: `10.1175/2008JPO3878.1` (see pp. 1, 15, 16, 18–21, 25, 41, 47, 54, 59, 60, 67, 68, 72, 73, 75, 76).

Ivey, G. N. and R. I. Nokes (1989), Vertical mixing due to the breaking of critical internal waves on sloping boundaries, *Journal of Fluid Mechanics*, **204,** pp. 479–500, DOI: `10.1017/S0022112089001849` (see p. 14).

Karsten, R. H. and J. Marshall (2002), Constructing the residual circulation of the ACC from observations, *Journal Of Physical Oceanography*, **32,** pp. 3315–3327, DOI: `10.1175/1520-0485(2002)032<3315:CTRCOT>2.0.CO;2` (see p. 19).

Koblinsky, C. J. and P. P. Niiler (1982), The relationship between deep ocean currents and winds east of barbados, *Journal of Physical Oceanography*, **12,** pp. 144–153, DOI: `10.1175/1520-0485(1982)012<0144:TRBDOC>2.0.CO;2` (see p. 5).

Kunze, E., E. Firing, J. M. Hummon, T. K. Chereskin, and A. M. Thurnherr (2006), Global Abyssal Mixing Inferred from Lowered ADCP Shear and CTD Strain Profiles, *Journal of Physical Oceanography*, **36,** pp. 1553–1576, DOI: `10.1175/JPO2926.1` (see pp. 4, 17).

Ledwell, J. R., A. J. Watson, and C. S. Law (1993), Evidence for slow mixing across the pycnocline from an open-ocean tracer-release experiment, *Nature*, **364,** pp. 701–703, DOI: `10.1038/364701a0` (see p. 4).

Lovenduski, N. S., N. Gruber, and S. C. Doney (2008), Toward a mechanistic understanding of the decadal trends in the Southern Ocean carbon sink, *Global Biogeochemical Cycles*, **22,** GB3016, DOI: `10.1029/2007GB003139` (see p. 2).

Marshall, D. and A. Naveira Garabato (2008), A Conjecture on the Role of Bottom-Enhanced Diapycnal Mixing in the Parameterization of Geostrophic Eddies, *Journal of Physical Oceanography*, **38,** pp. 1607–1613, DOI: `10.1175/2007JPO3619.1` (see pp. 1, 7–9, 12, 58, 59).

Marshall, G. J. (2003), Trends in the Southern Annular Mode from Observations and Reanalyses, *Journal of Climate*, **16,** pp. 4134–4143, DOI: `10.1175/1520-0442(2003)016<4134:TITSAM>2.0.CO;2` (see p. 31).

Marshall, J. and T. Radko (2003), Residual-Mean Solutions for the Antarctic Circumpolar Current and Its Associated Overturning Circulation, *Journal of Physical Oceanography*, **33,** pp. 2341–2354, DOI: `10.1175/1520-0485(2003)033<2341:RSFTAC>2.0.CO;2` (see p. 15).

Maximenko, N. A., B. Bang, and H. Sasaki (2005), Observational evidence of alternating zonal jets in the world ocean, *Geophysical Research Letters*, **32,** p. L12607, DOI: `10.1029/2005GL022728` (see p. 9).

Munk, W. and C. Wunsch (1998), Abyssal recipes II: energetics of tidal and wind mixing, *Deep Sea Research Part I: Oceanographic Research Papers*, **45,** pp. 1977–2010, DOI: `10.1016/S0967-0637(98)00070-3` (see pp. 1, 20, 22, 24, 58).

Munk, W. H. (1966), Abyssal recipes, *Deep Sea Research and Oceanographic Abstracts*, **13,** pp. 707 –730, DOI: `10.1016/0011-7471(66)90602-4` (see p. 17).

Naveira Garabato, A. C., K. L. Polzin, B. A. King, K. J. Heywood, and M. Visbeck (2004), Widespread Intense Turbulent Mixing in the Southern Ocean, *Science*, **303,** pp. 210–213, DOI: 10.1126/science.1090929 (see pp. 4, 9).

Naveira Garabato, A. C., D. P. Stevens, A. J. Watson, and W. Roether (2007), Short-circuiting of the overturning circulation in the Antarctic Circumpolar Current, *Nature*, **447,** pp. 194–197, DOI: 10.1038/nature05832 (see pp. 9, 45).

Nikurashin, M. and R. Ferrari (2010), Radiation and Dissipation of Internal Waves Generated by Geostrophic Motions Impinging on Small-Scale Topography: Application to the Southern Ocean, *Journal of Physical Oceanography*, **40,** pp. 2025–2042, DOI: 10.1175/2010JPO4315.1 (see p. 30).

Nikurashin, M. and G. Vallis (2011), A Theory of Deep Stratification and Overturning Circulation in the Ocean, *Journal of Physical Oceanography*, **41,** pp. 485–502, DOI: 10.1175/2010JPO4529.1 (see pp. 1, 17, 18, 31, 41, 43, 44, 47, 51, 54, 57, 59).

Nikurashin, M., G. K. Vallis, and A. Adcroft (2013), Routes to energy dissipation for geostrophic flows in the Southern Ocean, *Nature Geosci*, **6,** pp. 48–51, DOI: 10.1038/ngeo1657 (see p. 9).

Olbers, D., D. Borowski, C. Volker, and J. O. Wolff (2004), The dynamical balance, transport and circulation of the Antarctic Circumpolar Current, *Antarctic Science*, **16,** pp. 439–470, DOI: 10.1017/S0954102004002251 (see p. 11).

Osborn, T. R. (1980), Estimates of the Local-Rate of Vertical Diffusion from Dissipation Measurements, *Journal of Physical Oceanography*, **10,** pp. 83–89, DOI: 10.1175/1520-0485(1980)010<0083:EOTLRO>2.0.CO;2 (see p. 12).

Pacanowski, R. (1995), *MOM 2 Documentation User's Guide and Reference Manual*, tech. rep., GFDL Ocean Group Technical Report 3. NOAA, GFDL. Princeton. 232 pp. (see p. 27).

Polzin, K. L., J. M. Toole, J. R. Ledwell, and R. W. Schmitt (1997), Spatial Variability of Turbulent Mixing in the Abyssal Ocean, *Science*, **276,** pp. 93–96 (see pp. 4, 17).

Rhines, P. B. (1975), Waves and turbulence on a beta-plane, *Journal of Fluid Mechanics*, **69,** pp. 417–443, DOI: 10.1017/S0022112075001504 (see p. 7).

Saenko, O. A. (2008), On the Strong Seasonal Currents in the Deep Ocean, *Journal of Climate*, **21,** pp. 5642–5656, DOI: 10.1175/2008JCLI2262.1 (see p. 6).

Saenko, O. A., A. Sen Gupta, and P. Spence (2012), On Challenges in Predicting Bottom Water Transport in the Southern Ocean, *Journal of Climate*, **25,** pp. 1349–1356, DOI: 10.1175/JCLI-D-11-00040.1 (see p. 21).

Salmon, R. (1998), *Lectures on Geophysical Fluid Dynamics*, Oxford University Press, p. 400 (see p. 7).

Schlosser, F. and C. Eden (2007), Diagnosing the energy cascade in a model of the North Atlantic, *Geophysical Research Letters*, **34,** p. L02604, DOI: `10.1029/2006GL027813` (see p. 66).

Scott, R. B., J. A. Goff, A. C. Naveira Garabato, and A. J. G. Nurser (2011), Global rate and spectral characteristics of internal gravity wave generation by geostrophic flow over topography, *Journal of Geophysical Research-Oceans*, **116,** p. C09029, DOI: `10.1029/2011JC007005` (see pp. 5, 29).

Scott, R. B. and F. Wang (2005), Direct Evidence of an Oceanic Inverse Kinetic Energy Cascade from Satellite Altimetry, *Journal of Physical Oceanography*, **35,** pp. 1650–1666, DOI: `10.1175/JPO2771.1` (see pp. 7, 8, 66).

Shakespeare, C. J. and A. M. Hogg (2012), An Analytical Model of the Response of the Meridional Overturning Circulation to Changes in Wind and Buoyancy Forcing, *Journal of Physical Oceanography*, **42,** pp. 1270–1287, DOI: `10.1175/JPO-D-11-0198.1` (see pp. 31, 47).

Sheen, K. L., J. A. Brearley, A. C. N. Garabato, S. Waterman, D. A. Smeed, J. R. Ledwell, M. P. Meredith, L. St. Laurent, A. M. Thurnherr, J. M. Toole, and A. J. Watson (2013), Rates and mechanisms of turbulent dissipation and mixing in the Southern Ocean: Results from the DIMES experiment, *Journal of Geophysical Research: Oceans*, in press, DOI: `10.1002/jgrc.20217` (see p. 34).

Sloyan, B. M. (2005), Spatial variability of mixing in the Southern Ocean, *Geophysical Research Letters*, **32,** p. L18603, DOI: `10.1029/2005GL023568` (see pp. 4, 9).

St. Laurent, L. and H. Simmons (2006), Estimates of power consumed by mixing in the ocean interior, *Journal of Climate*, **19,** pp. 4877–4890, DOI: `10.1175/JCLI3887.1` (see p. 58).

St. Laurent, L. C., H. L. Simmons, and S. R. Jayne (2002), Estimating tidally driven mixing in the deep ocean, *Geophysical Research Letters*, **29,** p. 2106, DOI: `10.1029/2002GL015633` (see p. 13).

St. Laurent, L. and C. Garrett (2002), The Role of Internal Tides in Mixing the Deep Ocean, *Journal of Physical Oceanography*, **32,** pp. 2882–2899, DOI: `10.1175/1520-0485(2002)032<2882:TROITI>2.0.CO;2` (see p. 30).

Tandon, A. and C. Garrett (1996), On a Recent Parameterization of Mesoscale Eddies, *Journal of Physical Oceanography*, **26,** pp. 406–411, DOI: `10.1175/1520-0485(1996)026<0406:OARPOM>2.0.CO;2` (see pp. 2, 10, 11, 30).

Toggweiler, J. R. and B. Samuels (1998), On the ocean's large-scale circulation near the limit of no vertical mixing, *Journal of Physical Oceanography*, **28,** pp. 1832–1852, DOI: `10.1175/1520-0485(1998)028<1832:OTOSLS>2.0.CO;2` (see p. 17).

Vallis, G. K. (2006), *Atmospheric and Oceanic Fluid Dynamics*, Cambridge University Press, p. 745 (see p. 61).

Visbeck, M., J. Marshall, T. Haine, and M. Spall (1997), Specification of Eddy Transfer Coefficients in Coarse-Resolution Ocean Circulation Models, *Journal of Physical Oceanography*, **27,** pp. 381–402, DOI: `10.1175/1520-0485(1997)027<0381:SOETCI>2.0.CO;2` (see pp. 65, 66).

Walter, M., C. Mertens, and M. Rhein (2005), Mixing estimates from a large-scale hydrographic survey in the North Atlantic, *Geophysical Research Letters*, **32,** p. L13605, DOI: `10.1029/2005GL022471` (see p. 4).

Weaver, A. J., M. Eby, E. C. Wiebe, C. M. Bitz, P. B. Duffy, T. L. Ewen, A. F. Fanning, M. M. Holland, A. MacFadyen, H. D. Matthews, K. J. Meissner, O. Saenko, A. Schmittner, H. X. Wang, and M. Yoshimori (2001), The UVic Earth System Climate Model: Model description, climatology, and applications to past, present and future climates, *Atmosphere-Ocean*, **39,** pp. 361–428, DOI: `10.1080/07055900.2001.9649686` (see p. 26).

Weaver, A. J. and E. S. Sarachik (1990), On the Importance of Vertical Resolution in Certain Ocean General Circulation Models, *Journal of Physical Oceanography*, **20,** pp. 600–609, DOI: `10.1175/1520-0485(1990)020<0600:OTIOVR>2.0.CO;2` (see p. 28).

Willebrand, J., S. G. H. Philander, and R. C. Pacanowski (1980), The oceanic response to large-scale atmospheric disturbances, *Journal of Physical Oceanography*, **10,** pp. 411–429, DOI: `10.1175/1520-0485(1980)010<0411:TORTLS>2.0.CO;2` (see p. 6).

Wolfe, C. L. and P. Cessi (2010), What Sets the Strength of the Middepth Stratification and Overturning Circulation in Eddying Ocean Models?, *Journal Of Physical Oceanography*, **40,** pp. 1520–1538, DOI: `10.1175/2010JPO4393.1` (see pp. 17, 57, 58).

Wunsch, C. (1998), The work done by the wind on the oceanic general circulation, *Journal of Physical Oceanography*, **28,** pp. 2332–2340, DOI: `10.1175/1520-0485(1998)028<2332:TWDBTW>2.0.CO;2` (see pp. 5, 11, 31, 32, 58).

Wunsch, C. and R. Ferrari (2004), Vertical mixing, energy, and the general circulation of the oceans, *Annual Review of Fluid Mechanics*, **36,** pp. 281–314, DOI: `10.1146/annurev.fluid.36.050802.122121` (see pp. 6, 11).

Zalesak, S. T. (1979), Fully Multidimensional Flux-Corrected Transport Algorithms for Fluids, *Journal of Computational Physics*, **31,** pp. 335–362, DOI: `10.1016/0021-9991(79)90051-2` (see p. 27).

Zhai, X. M. and D. P. Marshall (2013), Vertical Eddy Energy Fluxes in the North Atlantic Subtropical and Subpolar Gyres, *Journal of Physical Oceanography*, **43,** pp. 95–103, DOI: `10.1175/JPO-D-12-021.1` (see p. 6).

Zhai, X. M., H. L. Johnson, and D. P. Marshall (2010), Significant sink of ocean-eddy energy near western boundaries, *Nature Geoscience*, **3,** pp. 608–612, DOI: `10.1038/NGEO943` (see p. 9).